REPUBLIQUE ALGERIENNE DEMOCRATIQUE ET POPULAIRE

Ministère de l'Enseignement Supèrieur et de la Recherche Scientifique

Université Ferhat Abbas Sétif 1

Faculté des Sciences

Département de Physique

Contribution à la segmentation d'images: application en imagerie médicale

Thèse présentée par :

Imane MEHIDI

En vue de l'obtention du diplôme de Doctorat 3ème cycle LMD en Radiophysique et Imagerie Biomédicale

Soutenue devant le jury composé de :

Pr. Fayçal KHARFI	Université Ferhat Abbas Sétif 1	Président
Pr. Djamel. E. C. BELKHIAT	Université Ferhat Abbas Sétif 1	Directeur
Pr. Hacene AZIZI	Université Ferhat Abbas Sétif 1	Examinateur
Pr. Toufik BOUDEN	Université M.S. Benyahia Jijel	Examinateur
Pr. Nabil OUNOUGHI	Université M.S. Benyahia Jijel	Examinateur

2023 / 2024

PEOPLES' DEMOCRATIC REPUBLIC OF ALGERIA

Ministry of Higher Education and Scientific Research

Ferhat Abbas University of Setif

Faculty of Sciences

Department of Physics

Contribution to image segmentation: application in medical imaging

Dissertation presented by :

Imane MEHIDI

As a requirement to aim for the degree of 3^{rd} cycle Doctorate in
Radiation Physics and Biomedical Imaging

Approved by supervisory committee :

Prof. Fayçal KHARFI	Ferhat Abbas University Setif 1	President
Prof. Djamel. E. C. BELKHIAT	Ferhat Abbas University Setif 1	Advisor
Prof. Hacene AZIZI	Ferhat Abbas University Setif 1	Examinator
Prof. Toufik BOUDEN	M.S. Benyahia University Jijel	Examinator
Prof. Nabil OUNOUGHI	M.S. Benyahia University Jijel	Examinator

2023 / 2024

اللَّهُمَّ إِنِّي أَعُوذُ بِك
مِنْ عِلْمٍ لاَ يَنْفَعُ،
ومِنْ قَلْبٍ لاَ يَخْشَعُ،
وَمِنْ نَفْسٍ لاَ تَشْبَعُ،
ومِنْ دُعَاءٍ لاَ يُسْمَعُ.

Declaration

I, Imane MEHIDI, declare that this dissertation, " Contribution to image segmentation: application in medical imaging " of Ferhat Abbas University; I confirm that:

- Date I have presented in the dissertation, information and documents are obtained in the framework of academic and ethical rules,
- All information, documentation, assessment and results are in accordance with scientific ethics and morals,
- have given the references for all the works that I used in this dissertation,
- I use the data obtained from the experiments without any change or modification,
- I declare that the work presented in this dissertation is original,

I understand that all the rights and privileges earned through this dissertation can be revoked if any parts of the above declarations are found to be untrue.

Signed : .....

Date : .....

.

Acknowledgments

All praise is due to Almighty ALLAH, who enabled me to accomplish this work.

I would like to express my deepest gratitude to my supervisor, **Professor Djamel Eddine Chouab Belkhiat**, for his tremendous academic support. I appreciate all his contributions of time and advice to make my research experience substantial and efficient.

I would also like to express my heartfelt appreciation for the thoughtful feedback and constructive criticism the **Jury Committee** provided. I am very grateful for the opportunity to present my research to such a distinguished panel of experts and for your unwavering support throughout the process. Thank you for your dedication, guidance, and valuable contributions.

Additionally, I am deeply grateful to those who made my stay in **Setif** unforgettable. I am appreciative of the experiences that I have had and the friendships that I have made. Your kindness and contributions have left me with many cherished memories. Thank you for the experience.

Lastly, I would like to extend my heartfelt gratitude to my dear **Family** and **Friends** in **Jijel**. Your words of wisdom, laughter, guidance, and camaraderie have been invaluable. Your love and unwavering support have not only helped me achieve my goals but have also helped me mature as a person. I am blessed to have such wonderful **Family** and **Friends**. Thank you for always being there for me, through thick and thin. You are the most valuable things in my life.

Imane Mehidi
30/1/2023

Abstract

Retinal imaging is a powerful tool for detecting and diagnosing various health conditions. Locating retinal vessels is important because it allows for the specification of different tissues of the vascular structure. Ophthalmologists use images with binary segmentation of retinal fundus to analyze and predict diseases such as hypertension and diabetes. However, blood vessel segmentation in retinal images can be challenging due to several factors such as low contrast, background illumination inhomogeneity, and noise.

The main objective of this dissertation is to study and propose effective methods for automatic retinal vasculature segmentation. Our first contribution involved studying the performance of improved FCM algorithms, including FCM, EnFCM, SFCM, FGFCM, FRFCM, DSFCM_N, FCM_SICM, and SSFCA, to recommend the best ones for the segmentation of retinal blood vessels. We evaluated their performance based on three criteria: noise robustness, blood vessel segmentation performance, and execution time.

In our second contribution, we proposed a new unsupervised method that ensures high-accuracy detection compared to previous studies. It depends on hybrid filtering and adaptive thresholding. We validated our proposed studies using two benchmark databases: STARE and DRIVE.

This dissertation also includes contributions related to the segmentation of MR brain images to identify tumors and different tissues. These contributions involve the development of new methods that have been evaluated using various databases and have shown promising results. These contributions are included in the appendices of the dissertation.

Overall, this dissertation aims to contribute to the field of medical image segmentation by proposing effective new methods, which can help in disease detection and monitoring.

Keywords: image processing, segmentation, classification, retinal, blood vessels.

Résumé

L'imagerie rétinienne est un outil puissant pour détecter et diagnostiquer diverses état de santé. La localisation des vaisseaux rétiniens est importante car elle permet de spécifier différents tissus de la structure vasculaire. Les ophtalmologistes utilisent des images avec une segmentation binaire de la rétine pour analyser et prédire des maladies telles que l'hypertension et le diabète. Cependant, la segmentation des vaisseaux sanguins dans les images rétiniennes peut être difficile en raison de plusieurs facteurs tels que le faible contraste, l'inhomogénéité de l'éclairage du fond d'œil et le bruit.

Le principal objectif de cette thèse est d'étudier et de proposer des méthodes efficaces pour la segmentation automatique de la vascularisation rétinienne. Notre première contribution consiste à étudier les performances des algorithmes FCM améliorés, notamment FCM, EnFCM, SFCM, FGFCM, FRFCM, DSFCM_N, FCM_SICM et SSFCA, pour recommander les meilleurs pour la segmentation des vaisseaux sanguins rétiniens. Nous avons évalué leur performance sur la base de trois critères : la robustesse au bruit, la performance de segmentation des vaisseaux sanguins et le temps d'exécution.

Dans notre deuxième contribution, nous avons proposé une nouvelle méthode non supervisée qui garantit une détection de haute précision par rapport aux études précédentes. Elle dépend du filtrage hybride et du seuillage adaptatif. Nous avons validé nos études proposées en utilisant deux bases de données de référence : STARE et DRIVE.

Cette thèse comprend également des contributions liées à la segmentation des images cérébrales en IRM pour l'identification des tumeurs et des différents tissus. Ces contributions impliquent le développement de nouvelles méthodes qui ont été évaluées à l'aide de différentes bases de données et ont montré des résultats prometteurs. Ces contributions sont incluses dans les annexes de la thèse.

Dans l'ensemble, cette thèse vise à contribuer au domaine de la segmentation des images médicales en proposant de nouvelles méthodes efficaces, qui peuvent aider à la détection et au suivi des maladies.

Mots-clés : traitement d'images, segmentation, classification, rétine, vaisseaux sanguins.

الملخص

يعد استخراج الأوعية الدموية في الشبكية أمرًا بالغ الأهمية لأنه يسمح بتحديد الأنسجة المختلفة لبنية الأوعية الدموية. يستخدم أطباء العيون الصور ذات التجزئة الثنائية لخلفية الشبكية لتحليل الأمراض والتنبؤ بها مثل ارتفاع ضغط الدم والسكري. ومع ذلك، يمكن أن تكون استخراج وتجزئة الأوعية الدموية في صور الشبكية أمرًا صعبًا بسبب عدة عوامل مثل انخفاض التباين، عدم تجانس الإضاءة الخلفية، ووجود التشويش.

الهدف الرئيسي من هذه الأطروحة هو دراسة واقتراح طرق فعالة وآلية لاستخراج الأوعية الدموية في الشبكية. في هذا السياق، قمنا في مساهمتنا الأولى بالتحليل ودراسة أداء بعض خوارزميات FCM المحسّنة للإبراز أفضلها في التجزئة. تتضمن هذه الدراسة الخوارزميات التالية: FCM ، EnFCM ، SFCM ، FGFCM ، FRFCM ، DSFCM_N ، FCM_SICM و SSFCA. اختبرنا أدائهم بالتركيز على ثلاث نقاط: قوة إزالة التشويش، أداءها في تجزئة الأوعية الدموية وسرعة الاداء.

أما في مساهمتنا الثانية، اقترحنا طريقة جديدة غير خاضعة للإشراف توفر كشفًا عالي الدقة مقارنة بالدراسات السابقة. تعتمد هذه التجزئة على التصفية الهجينة والعتبة التكيفية. تم تحقق من صحة الدراسة المنجزة والطريقة المقترحة باستخدام قاعدتي بيانات مرجعية: STARE و DRIVE.

تتضمن هذه الاطروحة أيضًا مساهمات متعلقة بتجزئة صور الدماغ بالرنين المغناطيسي لتحديد الأورام والأنسجة المختلفة. تشمل هذه المساهمات تطوير طرق جديدة تم تقييمها باستخدام قواعد بيانات مختلفة وأظهرت نتائج واعدة. تم تضمين هذه المساهمات في ملحقات الأطروحة.

بشكل عام ، تهدف هذه الأطروحة إلى المساهمة في مجال تجزئة الصور الطبية من خلال اقتراح طرق جديدة فعالة، والتي يمكن أن تساعد في الكشف عن الأمراض ومراقبتها.

الكلمات المفتاحية: معالجة الصور، التجزئة، التصنيف، الشبكية، الأوعية الدموية.

Scientific productions

Journal papers

- Imane Mehidi, Djamel Eddine Chouaib Belkhiat, and Dalel Jabri. "A high accuracy segmentation method for retinal blood vessel detection based on hybrid filters and an adaptive thresholding". Journal of Ambient Intelligence and Humanized Computing, 20 May 2022. https://doi.org/10.1007/s12652-022-03893-y.

- Imane Mehidi, Djamel Eddine Chouaib Belkhiat, and Dalel Jabri. "Comparative analysis of improved FCM algorithms for the segmentation of retinal blood vessels". Soft Computing, 03 October 2022. https://doi.org/10.1007/s00500-022-07531-9.

Conference proceedings

Scopus indexed conferences

- Sarra Atek, Imane Mehidi, Abbas Imane Khadidja, Sarra Zoghbi, Dalel Jabri, and Djamel Eddine Chouaib Belkhiat. "U-Net Based Retinal Vessel Detection on DRIVE and CHASE_DB1 Databases: The Impact of Data Augmentation " In 2024 8th International Conference on Image and Signal Processing and their Applications (ISPA). IEEE, 2024.

- Imane Mehidi, Dalel Jabri, and Djamel Eddine Chouaib Belkhiat. "Retinal Image Segmentation Using Clustering Methods: Performance Analysis." In 2022 19th International Multi-Conference on Systems, Signals & Devices (SSD'22). IEEE, Setif, Algeria, May 2022.

- Sarra Atek, Imane Mehidi, Dalel Jabri, and Djamel Eddine Chouaib Belkhiat. "SwinT-Unet: Hybrid architecture for Medical Image Segmentation Based on Swin transformer block and Dual-Scale Information " In 2022 7th International Conference on Image and Signal Processing and their Applications (ISPA). IEEE, 2022.

- Imane Mehidi, Djamel Eddine Chouaib Belkhiat, and Dalel Jabri. "A fast K-means clustering algorithm for separation of brain tissues in MRI." In 2020 2nd

International Conference on Mathematics and Information Technology (ICMIT), pp.132-137. IEEE, 2020.

- Imane Mehidi, Djamel Eddine Chouaib Belkhiat, and Dalel Jabri. "An improved clustering method based on k-means algorithm for MRI brain tumor segmentation." In 2019 6th International Conference on Image and Signal Processing and their Applications (ISPA), pp. 1-6. IEEE, 2019.

Books and Chapters

- Imane Mehidi, Djamel Eddine Chouaib Belkhiat, and Dalel Jabri. "Automatic Brain Tumor Segmentation Using Multi-OTSU Thresholding and Morphological Reconstruction." In International Conference on Computing Systems and Applications, pp. 289-300. Springer, Cham, 2020.

Non-indexed conferences

- Imane Mehidi, Djamel Eddine Chouaib Belkhiat, and Dalel Jabri. "Retinal Blood Vessel Image Segmentation by Common Algorithms: Analysis Performance", 1st International Conference and School on Radiation Imaging (ICSRI-2021). Sétif, Algérie.

- Imane Mehidi, Djamel Eddine Chouaib Belkhiat, and Dalel Jabri. "A Robust K-means Clustering Algorithm for Tissues Segmentation of Brain MRI", International Conference on Pattern Analysis and Recognition (ICPAR 2019). Tebessa, Algeria.

Medical days

- Imane Mehidi and, Djamel Eddine Chouaib Belkhiat,"Une Méthode améliorée de segmentation des tumeurs basée sur le seuillage à plusieurs niveaux et reconstruction morphologique", 5$^{\text{ème}}$ journée d'étude internationale de la physique médicale. Sétif, Algérie.

- Imane Mehidi and, Djamel Eddine Chouaib Belkhiat, "Contribution à la segmentation medicale: application à l'imagerie médicale", 4$^{\text{ème}}$ journée d'étude internationale de la physique médicale. Sétif, Algérie.

Contents

List of Figures

List of Tables

List of abbreviations

A

Acc Accuracy

ANN Artificial Neural Networks

AMD Age-related Macular Degeneration

B

BLH Bowler-Hat

BTH Bottom-Hat

C

CLAHE Contrast Limited Adaptive Histogram Equalization

CPU Central Processing Unit

CVD Circular Vessel Ratio

D

DR diabetic Retinopathy

DRIVE Digital Retinal Image for Vessel Extraction

F

FP False Positive

FN False Negative

FOV Field Of View

FCM Fuzzy C-Means

G

GT Ground Truth

H

HRF High-Resolution Fundus

I

ICA Independent Component Analysis

J

JPEG Joint Photographic Experts Group image format

K

KNN K-Nearest Neighbors

M

MATLAB MATrix LABoratory

MCC Matthews Correlation Coefficient

MF Matched Filter

MRI Magnetic Resonance Imaging

O

OD Optic Disc

P

PCA Principal Component Analysis

PMM Portable Pixmap Format

T

TN True Negative

TP True Positive

S

Se Sensitivity

Sp Specificity

SVM Support Vector Machine

STARE STructured Analysis of the REtina

R

RGB Red, Green and Blue

ROI Region Of Interest

General introduction

The ability to view the inside of the human body without performing surgery has always fascinated people. This is now made possible due to advancements in science and technology in the healthcare industry, where medical imaging has greatly improved, and various forms have been created [1].

Over the past few decades, fundus images have been used by eye specialists to diagnose and treat eye conditions. As a result, it's crucial for experts to utilize digital image processing techniques on retinal images to identify various features of the retina, optic disc, blood vessels, and macula [2, 3].

The use of computer-based image analysis has played a major role in detecting imbalances in the ocular retina, including bleeding, aneurysms, secretions, and disc disorders. Furthermore, this analysis enables the detection and prediction of serious diseases such as diabetes, glaucoma, blindness, and macular edema.

Retinal image segmentation, the process of dividing an image into different segments or regions, is a crucial task in ophthalmology. It involves separating the different structures in a fundus image, such as blood vessels, optic disk, and other features. Segmentation is necessary for various applications, including disease diagnosis, monitoring, and treatment planning.

However, manual segmentation is often the preferred method for retinal images and can be challenging. It is labor-intensive, time-consuming, and prone to human error, particularly for large-scale screenings. Although most pixels in the image can be easily rated by an ophthalmologist, some pixels, such as those at the border of the vessel, those near pathologic vessels, and those of small vessels, are difficult to distinguish accurately [4–6].

Therefore, there is a need for methods that can reduce manual supervision while improving speed and accuracy. This has led to a significant amount of research effort to address the problem of retinal image segmentation. The methods used in the literature can be broadly classified into two categories: supervised and unsupervised. Supervised methods rely on labeled data to train a model that can segment vessels. In contrast, unsupervised methods use unlabeled data to learn the underlying structure of the images and segment the vessels. These efforts aim to develop algorithms that can accurately and efficiently segment the vessels in retinal images, improving the accuracy of diagnosis and treatment of eye diseases.

Contributions

The field of retinal vessel segmentation in fundus images has received much attention due to its importance in diagnosing numerous diseases. Despite advances in image processing techniques, retinal vessel segmentation still remains a persistent challenge. Our research focuses on improving the accuracy of retinal vessel segmentation through the use of matching filter techniques, clustering methods, and the development of a field-of-view mask. The goal is to increase the efficiency of segmentation and analysis procedures using the DRIVE and STARE image databases.

The first contribution of this dissertation the analysis of performance of various improved fuzzy c-mean (FCM) algorithms for the segmentation of retinal blood vessels. Eight different variants of the FCM algorithm, including FCM, EnFCM, SFCM, FGFCM, FRFCM, DSFCM_N, FCM_SICM, and SSFCA, are evaluated in terms of three main criteria: noise robustness, blood vessel segmentation performance, and computational time. A range of metrics was used to assess performance, and the study results are used to recommend the best algorithm for retinal vessel segmentation.

The second contribution is the development of an unsupervised method for retinal blood vessel segmentation that provides high-accuracy detection. This method is based on a new hybrid combination of well-known tools such as Contrast Limited Adaptive Histogram Equalization (CLAHE), Bottom-Hat (BTH) filtering, Jerman filtering, and Bowler-Hat (BLH) filtering. The method first performs contrast enhancement and detail preservation of the retina image using CLAHE and BTH filtering. Then, the vessel tree structure was extracted using Jerman filtering, the improved retinal image was denoised and delicate vessels are enhanced in appearance using reconstruction operations and BLH filtering. A Field-of-View (FoV) mask was also generated to prevent background pixels from overlapping in the segmentation process. Finally, adaptive thresholding was performed to binarize the enhanced images, resulting in improved segmentation accuracy compared to other methods.

In conclusion, this dissertation presents a comprehensive and effective approach for retinal vessel segmentation, which combines various techniques and tools to achieve improved accuracy and efficiency in the segmentation and analysis procedures using the STARE and DRIVE image databases.

In addition to the contributions outlined in the main body of this dissertation, other related contributions have been made that concern the segmentation of MR brain images for the identification and analysis of tumors and different tissues [7–9]. These contributions include the development of novel methods. The proposed methods have been evaluated using various databases and have shown promising results in terms of accuracy, sensitivity, and specificity in detecting brain tumors and different types of tissues. They represent important and valuable research that contributes to the

objectives of this dissertation, which are focused on developing effective and efficient methods for medical image segmentation.

Dissertation outline

All the chapters in this dissertation reflect our articles published in scientific journals. It contains five chapters divided into two main parts: Background and Contributions. The background part overviews retinal images and discusses their segmentation methods, importance, and challenges. The contributions part presents our proposed techniques that improve image segmentation of retinal vessels. This dissertation is organized as follows:

Part 1 Background

Chapter 1: Entitled "Clinical Context," this chapter serves as an introduction to the anatomy and imaging techniques utilized in the examination of the human eye. It delves into the significance of fundus photography, emphasizing the precise identification of landmarks for accurate diagnosis and monitoring of ocular conditions. Additionally, the chapter addresses the challenges associated with automated retinal blood vessel segmentation. It offers a comprehensive overview of ocular anatomy, medical imaging techniques, and provides a brief overview of MRI images of the brain.

Chapter 2: titled "Literature review: Retinal vessel segmentation," presents a detailed analysis of the diverse approaches used to segment blood vessels in retinal fundus images. The chapter thoroughly discusses the techniques used for enhancement in segmenting retinal vessel images. Furthermore, it evaluates the retinal databases that are currently available and the metrics used for retinal vessel segmentation.

Part 2 Contributions

Chapter 3: titled "Performance Analysis of Improved FCM Algorithms for Retinal Image Segmentation," is the first contribution that presents the performance evaluation of eight improved FCM algorithms for retinal blood vessel segmentation. The algorithms evaluated are FCM, EnFCM, SFCM, FGFCM, FRFCM, DSFCM_N, FCM_SICM, and SSFCA. The chapter recommends the best algorithms based on their performance. The evaluation mainly focuses on noise robustness, blood vessel segmentation performance, and running time.

Chapter 4: titled "An improved retinal image segmentation method based on hybrid filters and adaptive thresholding" presents the second contribution of vessel

segmentation in retinal images. The proposed method addresses two major challenges: low and varied levels of image contrast and noise. To enhance visibility of the vessels, CLAHE and morphological filters were used, and to highlight both wide and thin vessels, the Jerman filtering technique was used. In addition, a mask was created to reduce computations and increase the efficiency of the vessel detection process. Finally, adaptive thresholding was used for vessel extraction. The obtained results were compared with other methods using two databases STARE and DRIVE.

Chapter 5: titled "Contributions to Brain Image Segmentation," presents our methodologies for segmenting brain images, addressing key challenges in accuracy and efficiency. Three segmentation methods are explored: multi-Otsu thresholding with morphological reconstruction, fast K-means clustering with histogram enhancement, and DPSO-K-means with morphological reconstruction. Experimental validation showcases superior performance in tumor detection and brain tissue segmentation, contributing to the advancement of medical image analysis.

Chapter 6: Presents conclusions and suggestions for further work.

Background

Chapter 1

Clinical context

1.1 Introduction

Medical imaging plays a pivotal role in modern healthcare, enabling clinicians and researchers to visualize internal structures, diagnose diseases, and monitor treatment responses with unprecedented precision. Among the diverse modalities available, imaging of the eye and brain holds particular significance due to the intricate and vital nature of these organs.

Eye exams are crucial in several areas of medicine, serving as a starting point for detecting local eye issues in ophthalmology and providing insight into the impact of systemic diseases in internal medicine. For instance, eye exams can indicate a person's risk of developing cardiovascular disease in cardiology. Certain diseases, such as hypertension, diabetes, arteriosclerosis, cardiovascular disease, and stroke, can be detected through examination of the retinal vasculature. Concurrently, MRI (Magnetic Resonance Imaging), the ability to non-invasively visualize the structures and functions of the brain has transformed our understanding of neurological disorders. MRI provides detailed insights into brain anatomy, pathology, and connectivity, aiding in the diagnosis of conditions ranging from tumors diseases like Alzheimer's.

This chapter aims to provide background information on retinal images by covering the medical aspects, including the anatomy of the eye and the different imaging techniques utilized to capture these images, while also providing a concise overview of brain imaging.

1.2 Eye anatomy

The eye is a complex organ that plays a critical role in our ability to see. Its anatomy includes several vital structures, such as the cornea, iris, lens, retina, optic nerve, sclera, and retinal vessels, as show in Figure 1.1 . The cornea is the transparent outer layer of the eye that helps to focus incoming light. The iris is the colored part

of the eye that controls the size of the pupil, which regulates the amount of light that enters the eye. The lens is a flexible, transparent structure behind the iris that helps focus light onto the retina. The retina is a thin layer of tissue at the back of the eye that contains photoreceptor cells that detect light and transmit visual information to the brain via the optic nerve. The sclera is the tough, white outer layer of the eye that helps to protect the delicate structures inside [10].

The blood vessels in the eye play a vital role in maintaining the health and proper functioning of the eye. They supply oxygen and nutrients to the various structures of the eye. The retinal vessels help remove waste products and regulate fluid pressure within the eye, which is crucial for maintaining the proper shape of the eye and preventing damage to delicate structures [11].

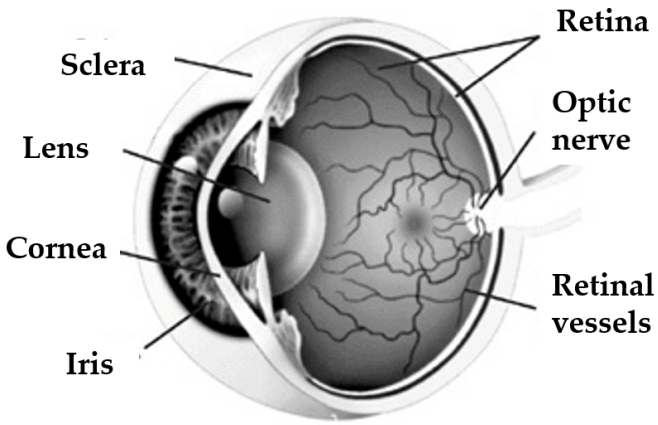

Figure 1.1: Anatomy of the eye [12].

1.2.1 Retinal vessels

The human eye's retinal blood vessels, consisting of arteries and capillaries, supply blood to the retina. The central retinal artery enters the eye through the optic nerve and branches into smaller vessels, eventually reaching the capillaries, which then connect to veins to form the central retinal vein. The close connection between the retina and the retinal blood vessels makes the retina a valuable tool for the non-invasive monitoring of various disorders, as changes in the blood vessels can indicate health issues.

As shown in Figure 1.2, normal retinal blood vessels are commonly straight and well-defined, with smooth walls and consistent diameters. In pathological conditions such as diabetic retinopathy or hypertension, the blood vessels may become distorted, have irregular walls, or show signs of stenosis or occlusion [13].

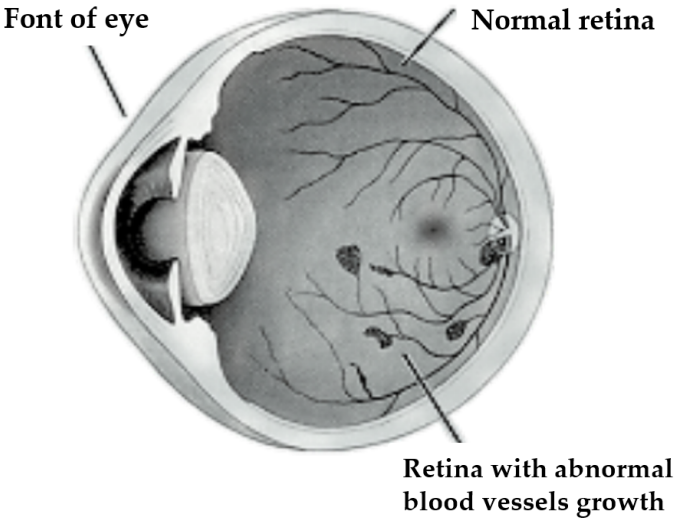

Figure 1.2: An example of normal and abnormal blood vessels [14].

One way to evaluate existing vessel detectors and develop robust vessel network segmentation methods in medical imaging is by classifying blood vessels based on their morphological features. Such features may include the vessel's shape, size, and branching pattern. Examples of vessel Classifications are Straight and Isolated Vessels, Parallel Vessels, Crossing Vessels, Bifurcation, and Corkscrew-like vessels [15].

1.2.2 Eye pathologies

An eye pathology is a disease or disorder affecting the eye's structure or function [13]. It can range from mild issues like dry eyes or styes to severe conditions like retinal detachment or glaucoma. Left untreated, some eye pathologies can result in vision loss. In the following, we provide a brief overview of some common eye diseases:

- **Cataracts:** are a clouding of the lens in the eye that affects vision and are a common condition, especially among older people. They can cause blurred vision, sensitivity to light and glare, double vision, and faded colors [16].

- **Glaucoma:** is a group of eye diseases that can damage the optic nerve and result in vision loss. It is often caused by increased pressure inside the eye but can also occur without elevated pressure. Glaucoma typically has no early symptoms, and vision loss is often gradual, so regular eye exams are important for early detection and treatment [17].

- **Age-related macular degeneration (AMD):** is a condition that affects the central part of the retina, known as the macula, causing vision loss. It is the leading cause of blindness in people over the age of 60. There are two forms of

AMD: "dry" and "wet." Dry AMD is the more common form and causes a gradual vision loss. Wet AMD is less common but more severe and can cause rapid vision loss [17].

- **Diabetic retinopathy:** a complication of diabetes that affects the eyes and can lead to vision loss or blindness. It occurs as a result of damage to the blood vessels in the retina and is caused by high blood sugar levels (Glycaemia) over time. Symptoms may include blurred vision, floaters, and difficulty seeing at night. In the early stages, diabetic retinopathy may not cause noticeable symptoms, so regular eye exams are important for early detection and treatment [18].

- **Retinal detachment:** is a serious eye condition in which the retina, the light-sensitive layer at the back of the eye, separates from its underlying supportive tissue. This can cause vision loss or blindness. Symptoms may include a sudden increase in floaters, flashing lights, and a shadow or curtain over part of your vision. Retinal detachment can be caused by a tear or hole in the retina, which allows fluid to accumulate and separate the retina from its underlying tissue [17].

- **Dry eye syndrome:** is a common condition in which the eyes do not produce enough tears, or the tears produced are of poor quality, leading to dryness and discomfort. Symptoms may include itching, burning, redness, and sensitivity to light. Various factors, including aging, environmental conditions, certain medications, and medical conditions can cause it [16–18].

1.3 Fundus imaging

The imaging of the fundus examines the retina to visualize the eye's internal structures, including the underlying blood vessels. The direct ophthalmoscope, invented by Herman von Helmholtz in the 1851s, is the predecessor of modern fundus imaging devices [19, 20]. The process involves illuminating the eye and capturing images of the reflected light with a digital camera. To capture the images, the subject is seated comfortably in front of the camera in a dark room, and a flash lamp is directed into the eye. The field of view can range from 35 to 60 degrees, and higher-resolution cameras are preferred to capture more detailed images [21]. The resulting images are digital, allowing for quantifiable analysis and easy data transfer through networks, as showed in Figure 1.3.
There are several different types of fundus imaging techniques, each with its own strengths and weaknesses. These techniques include:

1. **Fundus photography:** is a type of digital imaging that uses specialized cameras to capture images of the retina. The subject is seated comfortably in front of the

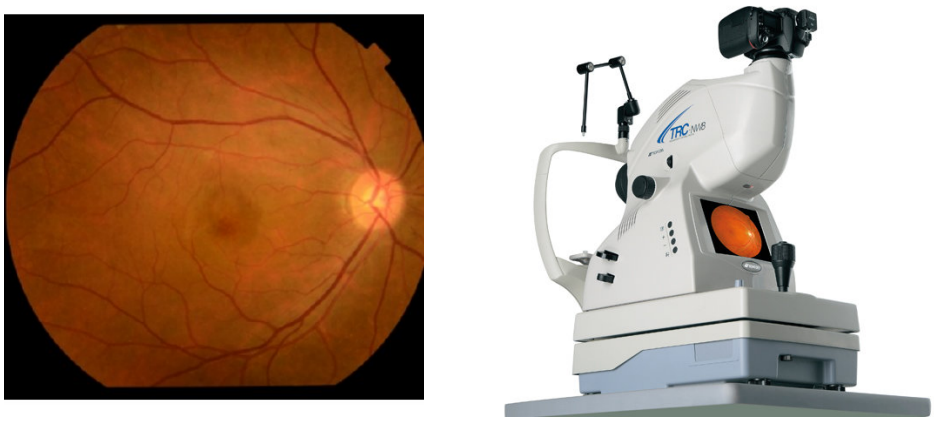

(a) **(b)**

Figure 1.3: (a) Sample fundus image. and (b) fundus camera [22].

camera and a flash lamp is directed into the eye to illuminate the retina. The reflected light is captured by the camera and a digital image is produced [23].

2. **Optical coherence tomography (OCT):** is a non-invasive imaging technique that uses light waves to create detailed cross-sectional images of the retina. This technique is commonly used to detect and monitor conditions such as macular degeneration and glaucoma [23].

3. **Fluorescein angiography:** is an imaging technique that involves injecting a fluorescent dye into the bloodstream and capturing images of the retina as the dye circulates through the blood vessels. The images captured by this technique are used to assess blood flow in the retina and identify any circulation issues [24].

However, the images produced by fundus imaging can suffer from non-uniform illumination and varying quality due to factors such as age, retinal pathologies, and the appearance of the retina. The illumination can cause the smallest vessels to appear very faint relative to the surrounding background. The quality of the images can also be impacted by anterior or posterior retinal pathologies. Despite these challenges, fundus imaging is a non-invasive, relatively inexpensive, and widely accepted method for examining the retina [25–27].

The imaging modality that will be used in this dissertation is color fundus photography. Color fundus photography is a well-established modality, and there are many publicly available databases that have been annotated for segmentation tasks. This makes it an ideal choice for researchers who want to compare their results with existing literature and benchmark databases.

Overall, the use of color fundus photography for segmentation in ophthalmology is a practical and effective imaging approach.

1.3.1 Landmarks of fundus photography

In fundus photography, the interior of the eye is captured and several landmarks are identified and evaluated. These landmarks serve as essential reference points for evaluating the health and condition of the retina and are used to diagnose and monitor various retinal diseases and conditions (subsection 1.2.2). They can also provide important information about the progression of retinal diseases and the effectiveness of treatments, including:

- **Optic disc** is a key landmark in fundus photography. The appearance of the optic disc can provide information about the presence of optic nerve damage or other conditions such as glaucoma [23].
- **Macula** is also a critical landmark in fundus photography. Changes in the macula can indicate the presence of age-related macular degeneration or other eye diseases [23].
- **Fovea** Fundus photography captures images of the fovea and the surrounding macula and retina, allowing for the detection and monitoring of eye diseases and disorders [23].
- **Vessels** is also a crucial landmark in fundus photography. The appearance of the blood vessels can indicate conditions such as diabetic retinopathy or retinal vein occlusions (see Figure 1.4).

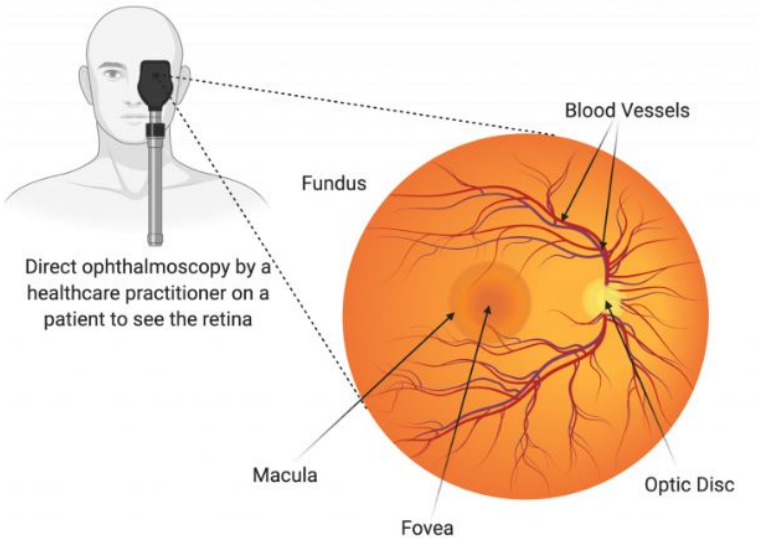

Figure 1.4: An example retinal image showing landmarks of fundus photography [28].

1.4 Automated Segmentation of Retinal Vessels

Semi-automatic segmentation of retinal blood vessels is a tedious and time-consuming task that requires a high degree of expertise and skill. The process involves a visual inspection of the retinal fundus image, followed by marking and tracing the boundaries of the blood vessels. This process must be performed with high accuracy to ensure that the results are usable for medical diagnosis. Semi-automatic segmentation is particularly challenging due to the low contrast and inhomogeneity of the background lighting in retinal fundus images and the presence of noise and color variations in the retina. These factors can make it difficult to accurately distinguish the blood vessels from other structures in the image [2, 23, 29–31].

Despite the difficulties, Semi-automatic segmentation is still widely used in ocular screening, especially for diseases such as diabetes and hypertension, where regular screening is necessary. However, Semi-automatic segmentation is not feasible for large-scale screening as it is time-consuming and requires highly skilled professionals.

Therefore, there has been a growing demand for automated retinal blood vessel segmentation methods to assist ophthalmologists and make the process more efficient and reliable. Automated methods have the advantage of being faster and less prone to human error, making them a valuable tool for medical diagnosis [32].

1.4.1 Challenges in retinal vessel segmentation

Retinal vessel segmentation is a challenging task due to the inherent characteristics of the vessels in retinal fundus images. Where the vessels are tree-like and tubular structures that are supposed to be connected. However, their appearance could be more consistent against the background, which makes them difficult to distinguish from the background.

The vessels' color is typically dark red, while the background is close to orange, and in a gray-level image, their appearance is close to the other elements in the background, such as the macula. Additionally, the appearance of capillaries may be very similar to that of the background.

The illumination of the image may also cause specular effects located on the center of the vessel objects, further complicating the segmentation process. The gray level of vessels is continuous and does not change abruptly, and the vessel shape is a piecewise linear shape with a relatively smooth curve without abrupt orientation changes. The width of vessels can vary widely, covering a range of diameters, and they can be extended along their length at any orientation. The cross-sectional intensity profile of vessels approximates a Gaussian shape, making it difficult to distinguish between vessels and non-vessel regions [5, 30, 33, 34].

These challenges make it difficult for automated algorithms to segment the reti-

nal vessels accurately. Some common techniques used to overcome these challenges include pre-processing techniques such as contrast enhancement, denoising, and background correction. Despite these efforts, retinal vessel segmentation remains a challenging problem, and there is ongoing research to improve these algorithms' accuracy and reliability.

1.5 Brain Magnetic Resonance Imaging (MRI)

Magnetic Resonance Imaging (MRI) is a powerful imaging technique that allows for the non-invasive visualization of the brain's internal structures with exceptional detail. This section aims to provide an overview of brain MRI, discussing its utility in clinical practice and research.

Brain MRI provides detailed insights into brain anatomy, pathology, and function. It plays a pivotal role in diagnosing diseases such as brain tumors, stroke, multiple sclerosis, Alzheimer's, and Parkinson's.

MRI scanners (Figure 1.5) generate images by utilizing strong magnetic fields and radiofrequency pulses to create high-resolution images of the brain. Different MRI sequences, such as T1-weighted, T2-weighted, FLAIR (Fluid-Attenuated Inversion Recovery), and diffusion-weighted imaging, provide complementary information about various tissue properties, enabling clinicians to assess different aspects of brain structure and function.

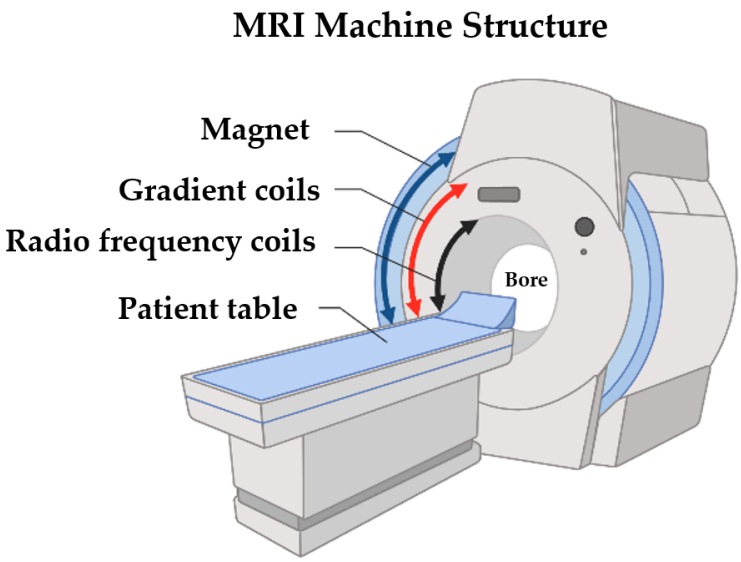

Figure 1.5: MRI scanner [35].

1.5.1 Brain MRI segmentation

Brain MRI segmentation is an essential task in many clinical applications, including measuring and visualizing different brain structures, delineating lesions, analyzing brain development, and image-guided interventions and surgical planning. The segmentation process involves dividing the brain MRI image into distinct regions, each representing a specific tissue type or structure, such as white matter (WM), gray matter (GM), or cerebrospinal fluid (CSF) [36]. There are various segmentation techniques, each with its

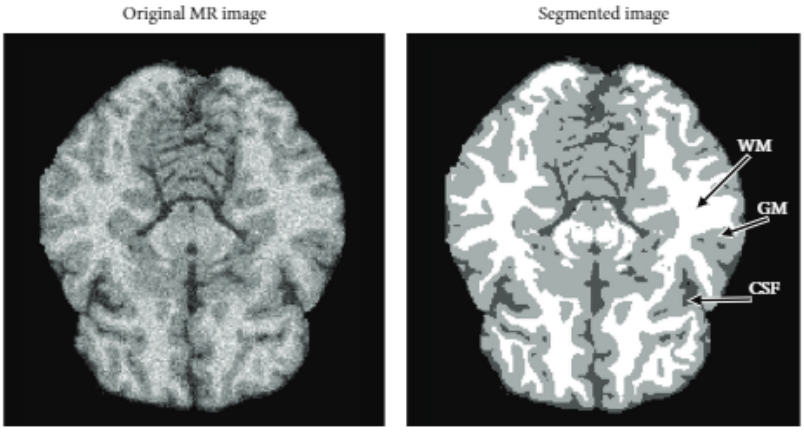

Figure 1.6: Brain MRI segmentation example [36].

advantages, limitations, and appropriate use cases. Some traditional methods include threshold-based methods, clustering-based methods, region-based methods, edge-based methods, and graph theory-based methods. However, these methods may not always provide accurate results, especially in complex cases with irregularly shaped structures or varying intensities [37].

1.5.2 Challenges in brain MRI segmentation

Brain MRI segmentation is a crucial step in many clinical applications, including image-guided interventions, surgical planning, and analyzing brain development. However, it is a challenging task due to various factors, including the complexity of brain structures, the presence of noise and artifacts, and the variability in image quality and contrast [38].

One of the major challenges in brain MRI segmentation is the low tissue contrast, particularly in infant brain MRI, where the intensity ranges of voxels in white matter (WM) and gray matter (GM) are largely overlapping, especially around the cortical regions. This creates the most challenge for tissue segmentation, making it difficult to accurately distinguish between WM, GM, and cerebrospinal fluid (CSF). Another challenge is the variability in image acquisition protocols, scanners, and imaging pro-

tocols, which can affect the quality and consistency of the images . This can lead to differences in image intensity, contrast, and noise, making it difficult to apply a single segmentation algorithm to images acquired from different sites or scanners Additionally, brain MRI segmentation can be time-consuming and prone to errors due to inter- or intraoperator variability studies, making it difficult to obtain accurate and consistent results. To address these challenges, various segmentation techniques of different accuracy and degree of complexity have been developed and reported in the literature [38, 39].

1.6 Conclusion

In conclusion, this chapter has provided an overview of the clinical context surrounding retinal imaging and brain MRI. We explored the anatomy of the eye, common eye pathologies, fundus imaging techniques, and challenges in automated retinal vessel segmentation. Additionally, we discussed the utility of brain MRI in diagnosing various neurological conditions and the challenges associated with brain MRI segmentation.

The next chapter presents a comprehensive review of the literature on retinal vessel segmentation, focusing on recent advancements, methodologies, and challenges in this field.

Chapter 2

Literature review: Retinal vessel segmentation

2.1 Introduction

RETINAL vessel segmentation is a crucial step in analyzing retinal images for diagnosing and monitoring eye diseases. The process involves dividing the retinal image into different segments, each corresponding to a specific structure within the eye, such as the blood vessels. In recent years, various techniques have been proposed for the automatic segmentation of retinal vessels. These techniques can be broadly classified into supervised and unsupervised methods.

This literature review aims to provide an overview of the different retinal image databases, the components of retinal images, and various methods for retinal vessel segmentation. Additionally, we discuss the different techniques used for retinal vessel enhancement and the metrics used to evaluate segmentation performance.

2.2 Retinal image databases

A retinal image processing database is a collection of retinal images and associated data, used for research and development of algorithms for analyzing and processing retinal images. These databases are used for various purposes such as developing algorithms for detecting and grading diabetic retinopathy, evaluating algorithms for retinal vessel segmentation, feature extraction, and for retinal image registration. The images in these databases may come from different sources such as digital fundus cameras or other imaging devices, and may be annotated with information such as retinal features, diagnosis, or image quality. The use of these databases helps to standardize research and enables comparison and benchmarking of different algorithms.

There are several publicly available databases that can be used for retinal image segmentation such as: STructured Analysis of the REtina (STARE) [40], Digital Retinal

Images for Vessel Extraction (DRIVE) [41] , Chinese Academy of Sciences, Huazhong University of Science and Technology, and Eye Hospital DataBase 1 (CHASE_DB1) [42], High-Resolution Fundus (HRF) [43] and the Indian Diabetic Retinopathy Image Dataset (IDRiD) [44], etc.

2.2.1 STARE database

The STARE database for blood vessel segmentation contains 20 retinal color images (10 with pathology) captured using TopCon TRV-50 camera with 35° Field of View (FoV), 700×605 pixels, 8 bits per channel, in PPM format. Includes two sets of manually segmented ground truth images by two specialists, with the performance of algorithms evaluated using the first observer's ground truth [40].
It should be noted that FoV stands for "Field of View," which refers to the visible area captured by a camera or other imaging device.

2.2.2 DRIVE database

The DRIVE database contains 40 retinal color images, 7 with diabetic retinopathy, captured using Canon CR5 camera, with 45° FoV, 768×584 pixels, 8-bits per channel, in JPEG format. It is divided into training (20 images with FoV masks and ground truth images) and test sets (20 images with FoV masks and two sets of ground truth images). Performance of algorithms is evaluated using the first observer's ground truth images [41].

Table 2.1 summarizes the characteristics of the STARE and DRIVE databases which are used as the basis for evaluating performance in our research.

Table 2.1: Characteristics of STARE and DRIVE databases.

Database	STARE	DRIVE
Number of image	20	40
Camera	TopCon TRV-50	Canon CR5
FoV	35°	45°
Spatial resolution	605 × 700	565 × 584
Format	PPM	JPEG
Ground truth	available	available
FoV mask	unavailable	available

- In the context of a database of retinal images, the **FoV mask** is a way to indicate which part of the image corresponds to the actual retina and which part is outside of the field of view. The FoV mask is a binary mask that indicates which pixels in the image are part of the retina and which are not. It is used to remove any

extraneous information outside of the FoV and to focus only on the relevant parts of the image for analysis or processing.

2.3 Retinal image Components

The color retinal image (RGB) consists of three channels red, green, and blue, as shown in Figure 2.1. Each channel captures different aspects of the retina, but the red channel is often over-saturated, and the blue channel lacks sufficient light to clearly reveal the blood vessels. In contrast, the green channel provides a better balance between highlighting the blood vessels and suppressing the background noise, which can improve the accuracy of the segmentation results. Additionally, the green channel is less sensitive to noise and artifacts compared to other channels, making it more reliable for segmentation. This is crucial because the quality of the retinal image can be affected by various factors such as the imaging device's quality, the patient's age, and the presence of certain eye conditions. Using the green channel can minimize the impact of these factors on the segmentation results [45].

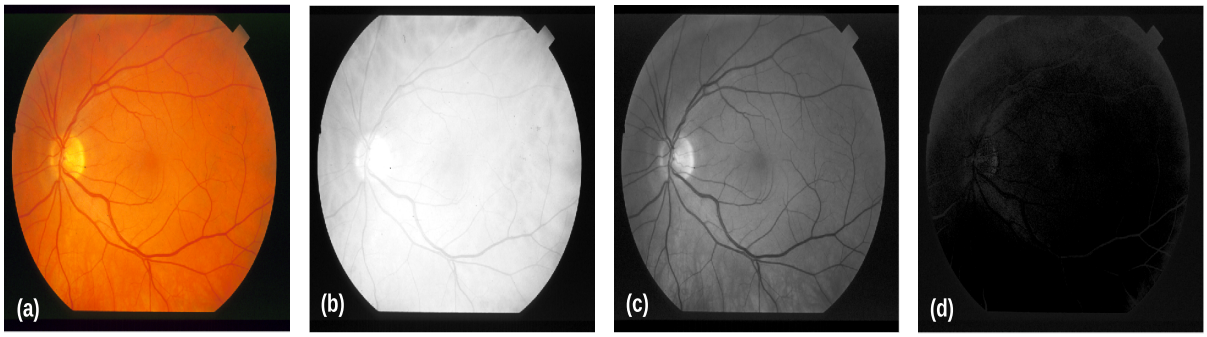

Figure 2.1: Color retinal image and its channels on STARE database. (a) RGB input image. (b) Red channel. (c) Green channel. (d) Blue channel.

2.4 Retinal vessel segmentation methods

A crucial aspect of retinal image analysis is determining important features of blood vessels with precision, largely determined by the effectiveness of blood vessel segmentation. The classification of retinal vessel segmentation methods into systematic categories based on their methodology has been an ongoing effort. At first, methods were divided into either contour-based or region-based categories. However, as the field has progressed, new techniques incorporating advancements have emerged, forming various subcategories [41, 46]. In recent years, researchers have combined algorithms in hybrid approaches, blurring the boundaries between methods. It is helpful to examine the surveys published in the literature to understand the field comprehensively [30, 47].

It is important to note that the categorization of retinal blood vessel segmentation methods in this review is not meant to be a rigid classification system. Many recent methods often incorporate techniques previously proposed by earlier researchers to address specific challenges, such as image smoothing, feature extraction, and pattern recognition. Some methods even employ hybrid techniques. This research adopts the classification of vessel segmentation methods into supervised and unsupervised methods.

2.4.1 Supervised methods

Supervised methods rely on prior labeling information to determine if a pixel belongs to a vessel or not. The algorithm learns a rule for vessel extraction based on a training set of reference images that have been manually segmented by an ophthalmologist or related professional, also known as the ground truth. However, obtaining a ground truth can be challenging in real-life applications [48].

Supervised techniques operate a set of samples to train a classifier that distinguishes between the vessel and non-vessel pixels, known as the training set. These techniques have evolved into machine learning and deep learning algorithms, such as Random Forest, Support Vector Machine (SVM), K Nearest Neighbors (KNN), and Artificial Neural Networks (ANN), which are widely used in the medical field [49].

Deep-learning networks trained on labeled data can be applied to unstructured data, allowing them to process much more input than traditional machine learning based approaches, resulting in higher performance [50–52]. However, a large training database with corresponding annotations is required to achieve high performance in deep learning models, which can be a challenge in retinal vessel segmentation.

2.4.2 Unsupervised methods

Unsupervised learning approaches utilize inherent patterns of blood vessels in retinal images to identify whether a particular pixel belongs to the vessel structure or not. In such methodologies, the algorithm design is not directly influenced by the ground truth [33]. Unsupervised learning approaches aim to automatically learn and extract these inherent patterns from the data without the need for explicit human annotation or labeling. The extracted patterns can then be used to segment the retinal images into regions of interest, such as the blood vessels, and to identify abnormalities or diseases that may be present in the retina.

The unsupervised methods reviewed for retinal vessel segmentation are primarily divided into six categories: matched filtering, mathematical morphology approach, multi-scale approach, model-based approach, vessel tracing approach, and other general approaches [2, 31]. Compared to supervised methods, unsupervised methods offer

the advantage of higher speed and lower computational complexity. For these reasons, we will focus on the unsupervised methods.

2.4.2.1 Matched filtering

The technique of using matched filtering to detect vasculature in retinal images involves convolving a 2D kernel with the image. This kernel is specifically designed to model a feature in the image, such as a vessel, with unknown orientation and position. The matched filter response obtained indicates the presence of this feature in the image. The design of the kernel takes advantage of three key properties of vasculature: vessels tend to have limited curvature and can be approximated by linear segments, their diameter decreases as they move away from the optic disk, and their cross-sectional intensity profile approximates a Gaussian curve.

However, applying the convolution kernel at multiple rotations can result in a significant computational overhead, and the kernel may only respond optimally to vessels that have the same standard deviation as the Gaussian function specified by the kernel. Other vessels with a different profile may not be detected, and the presence of retinal background variation or pathologies in the image can also increase the number of false responses, as these may exhibit similar local attributes as the vessels. Therefore, to improve the accuracy of this method, additional processing techniques should be used in conjunction with the matched filter response.

In this context, Chaudhuri et al. [53] proposed the use of the matched filter approach as the initial method. They asserted that the grey distribution of the vascular profile conforms to Gaussian properties and suggested convolving the image with a filter to isolate the target object. In their study, Hoover et al. [48] put forward a threshold descent search algorithm for extracting blood vessels post-matched filtering. The algorithm takes into account both the local features of the retinal vessels and the regional characteristics of the vascular network distribution. While this approach significantly reduces errors, it also complicates the overall calculation process.

Moreover, several researchers have made advancements to the matched filtering method, one of which is the approach proposed by Zhang et al. [54]. The authors utilized a double-sided thresholding model to enhance the results of matched filtering, thereby reducing false positives in pathological images. Additionally, they introduced a method that combines matched filtering and the first-order derivative of the Gaussian filter to improve the accuracy of vascular segmentation and identify vascular boundaries.

Li et al. [55] also presented a novel method for vessel extraction using multi-scale adaptations of the matched filter. This allowed for contrast enhancement of the image while suppressing noise, before applying a double thresholding method to detect the vessels. A method proposed by Neto et al. [56] aims to enhance the contrast of the inverted green layer of a raw image, followed by the application of a local threshold

based on the cumulative distribution. The results are then refined using morphological processes that aim to reduce noise and any remaining roughness in the image.

It is worth noting that the efficacy of the matched filter algorithm depends on the degree of matching between the template and the blood vessel, which can be influenced by various factors such as central light reflection, radius change, noise interference, and lesion interference [57].

2.4.2.2 Mathematical Morphology Approach

The mathematical morphology approach is a set of theories derived from mathematics that applies lattice theory to spatial constructions in image analysis. Unlike other methods, it focuses on the shapes present in an image rather than the intensity of pixels. Essentially, it treats pixel intensities as topographical highs. Initially, this approach was used in paired images but later became a general processing framework applied to grayscale and color images through morphological operators. In this context, Zana and Klein [58] developed a method for extracting the vascular tree using mathematical morphology that took into account the connectivity and local linear distribution of retinal vessels. However, this method had some limitations as it heavily relied on structural elements. Building on this method, Ayala et al. [59] proposed an improved approach that defined the averages of a given fuzzy set using a different definition of the mean of a random compact set.

Moreover, Soares et al. [60] employed morphological reconstruction and a regional growth method, followed by Gabor wavelet transformation to extract blood vessels. Mendonca and Campilho [46] utilized a multi-scale top hat transformation to enhance retinal blood vessels, followed by the extraction of vascular centerlines to obtain vessel segmentation. To further improve this implementation, Fraz et al. [61] combined vessel centerline detection with morphological bit plane slicing to achieve the final segmentation.

An unsupervised segmentation technique was proposed by Wang et al. [62] to enhance the texture contrast between the retinal vessels and background in fundus images. This method utilizes corrected morphological and fractal dimensions. Initially, the morphological factor, in conjunction with linear structural elements, removes any lesions and light reflections present in the image. Then, the blood vessels are extracted through the use of multi-threshold and fractal dimensions. The efficacy of this approach was tested on several publicly available databases, including STARE, DRIVE, and HRF.

2.4.2.3 Multi-scale approach

The use of multi-scale techniques involves varying image scales to facilitate vessel extraction, with a primary objective of improving execution speed. Such approaches

generate a scale space from the input image to identify various structures. Major vessel structures are identified from low-contrast images, whereas fine vasculatures are detected from high-contrast ones, which enhances robustness. The application of multi-scale methods is often employed in vessel extraction to address the challenge of vessel width variation in fundus images [33].

Frangi et al. [63] introduced a method for developing a vessel enhancement filter by analyzing the multi-scale second-order local structure of an image, specifically the Hessian matrix. By analyzing the eigenvalues of the Hessian matrix, this method allows for the detection of the principal directions in which the local second-order structure of the image can be decomposed. As a result, it can detect the direction of small intensity curvature along a vessel. Martinez-Perez et al. [64] also used a multi-scale approach to obtain information about the size, orientation, and width of vessels. They used two geometrical features that accounted for the first and second derivatives of the intensity to infer the topology of the image.

2.4.2.4 Model-based approach

Model-based approaches to retinal image analysis consist of vessel profile models and deformable models. Vessel profile models involve modeling the vessel cross-sectional intensity profile as a Gaussian-shaped curve or a mixture of Gaussians in the case of circular vessel ratio (CVR), which is a measure of the circularity of a blood vessel in a retinal image. The CVR is calculated by dividing the vessel area by the area of the smallest circle that can be fit around the vessel. Deformable models utilize both active contour and level set-based approaches.

In this category of segmentation methods, Xiao et al. [65] developed a Bayesian-based approach that takes spatial information into account, resulting in improved performance in detecting narrow and low-contrast vessels. For extracting major and minor vessels separately, Zhao et al. [66] employed a level set method based on region-scalable fitting energy function and a region-growing approach, respectively. Recently, Zhao et al. [67] proposed an inhomogeneity correction method based on Retinex theory and Local Polynomial (LP) analysis for vessel enhancement, and applied a segmentation approach based on an infinite perimeter active contour model using hybrid region information of the image. Notably, the latter authors evaluated their segmentation technique on Fluorescein Angiography (FA) images, which could pave the way for further research in retinal image analysis. In the study by Mahtab and Hossein [68], an improved active contour method was developed to accurately extract thin vessels and ridges from images. The method uses a discrete wavelet transform to reduce energy, and segmentation is divided into foreground and background using a minimization formula. The authors found that foreground pixels are more important than background pixels, so they modified the minimization formula to prioritize the foreground. The second part

of the innovation is an optimization procedure that replaces reinitialization to prevent the evolution process from becoming unstable. To maintain the contour on the image's edges, an optimization method formula was employed. The study evaluated the efficacy of the method on the DRIVE database and found that it has limitations in providing highly accurate detection.

2.4.2.5 Vessel tracing approach

Retinal segmentation using the vessel tracing method requires seed points, which can be selected either manually or through an automated process. Seed points are selected for the edges and the center of blood vessels. These seed points are then used to trace the entire vessel tree based on the available details. Since all vessels in the retina are interconnected, the use of this method results in better connectivity and allows for earlier diagnosis of diseases.

There have been several implementations using the vessel tracking approach. One of the earliest implementations was developed by Can et al. [69] in 1999, which uses directional templates to track vessels from initial seed points in real-time. The directional templates are designed to give the maximum response for an edge in a specific direction, and the algorithm takes a step in the direction of maximum response and repeats this procedure until the segmentation is complete. Another approach, proposed by Vlachos and Dermatas [70], uses multiscale line-tracking and post-processing with morphological operations.

Adel et al. [71] initially presented an approach that uses the maximum a posteriori probability criterion to perform the segmentation based on the vascular diameter, which was later improved by Yin et al. [72]. The proposed improvements include using a semi-ellipse as the dynamic search window to obtain local grey level statistical information. Delibasis et al. [73] proposed an algorithm that uses a parametric model to exploit geometrical properties for parameter definitions.

2.4.2.6 General approaches

General approach in unsupervised methods for retinal vessel segmentation includes a variety of methods that do not fit neatly into the other categories, such as hybrid methods that combine techniques from different categories to improve accuracy and robustness, and clustering-based methods that group pixels in the image based on similarity such as the two-level optimization method proposed by Hassanien et al. [74]. The method involves finding vessel clusters in the first level using artificial bee colony swarm optimization with a Fuzzy C-Means (FCM) fitness function, and enhancing the pattern search algorithm in the second level by adding shape descriptors as an additional feature in the fitness function. Other methods include thresholding [75],

graph-based approaches, dimensionality reduction techniques like Principal Component Analysis (PCA) [76] and Independent Component Analysis (ICA) [77].

The Table 2.2 presents an overview of the different techniques used to segment blood vessels in the retina.

2.5 Retinal vessel enhancement techniques

Retinal vessel enhancement methods are techniques used to improve the visibility and clarity of blood vessels in retinal images. The goal of retinal vessel enhancement is to make it easier to diagnose and monitor various eye diseases, such as diabetic retinopathy, age-related macular degeneration, and glaucoma.

In the following subsection, we will examine the most effective techniques used in our research.

2.5.1 Contrast limited adaptive histogram equalization

Contrast Limited Adaptive Histogram Equalization (CLAHE) is an advanced version of traditional histogram equalization, which is a technique for adjusting the contrast of an image. Traditional histogram equalization adjusts the overall histogram of the image to span the full range of possible intensities. However, this approach can result in over-saturation of certain areas and loss of detail in the image. CLAHE improves upon this by dividing the image into small, non-overlapping tiles and performing histogram equalization on each tile separately. This ensures that the local structure of the image is preserved, as the contrast is only adjusted within each small tile [94]. The equations for CLAHE are as follows:

Histogram computation: The first step in CLAHE is to divide the image into small overlapping tiles, and compute the histogram of each tile. Let's consider a tile t of size $m \times n$ pixels. The histogram 'h' of the tile can be computed using the following equation:

$$h(i) = number \;\; of \;\; pixels \;\; in \;\; tile \;\; t \;\; with \;\; intensity \;\; value \;\; i.$$

Cumulative histogram computation: The next step is to compute the cumulative histogram of each tile. The cumulative histogram 'H' is calculated as

$$H(i) = \sum h(j) \text{ where } j <= i. \tag{2.1}$$

Histogram scaling: The cumulative histogram is then scaled to a specified maximum

Table 2.2: Summary of techniques for retinal blood vessel segmentation.

Author (s)	Year	Database	Approach	Method
Marín et al. [78]	2010	ST DR	Machine learning	Supervised
Tuba et al. [79]	2017	DR		
Bandyopad [80]	2018	DR		
Melinscak et al. [81]	2015	DR	Deep learning	
Balasubret al. [51]	2021	ST DR		
Saravanan et al. [52]	2022	PRL		
Chaudhuri et al. [53]	1989	-	Matched filtering	Unsupervised
Hoover et al. [48]	2000	ST		
Zhang et al. [54]	2010	ST DR		
Azzopardi et al. [45]	2015	ST DR CHA		
Li et al. [55]	2012	ST DR		
Oliveira et al. [82]	2016	ST DR		
Zhang et al. [83]	2016	ST DR CHA		
Neto et al. [56]	2017	ST DR		
Roy et al. [84]	2019	ST DR		
Zana and Klein [58]	2001	-	Morphology	
Ayala et al. [59]	2005	ST		
Mendonca et al. [46]	2006	ST DR		
Fraz et al. [61]	2012	ST DR MESS		
Soomro et al. [85]	2018	ST DR		
Wang et al. [62]	2019	ST DR HRF		
da Rocha et al. [86]	2020	ST DR HRF		
Frangi et al. [63]	1998	-	Multi-scale	
Martinez et al. [64]	2007	HOOVER		
Fathi et al. [87]	2013	ST DR		
Khomri et al. [88]	2018	ST DR		
Shah et al. [89]	2019	ST DR HRF		
Xiao et al. [65]	2013	ST DR	Model-based approach	
Salazar et al. [90]	2014	ST DR		
Zhao et al. [67]	2015	ST DR VAMP		
Zhao et al. [91]	2017	ST DR		
Mahtab et al. [68]	2022	ST DR HRF CHA		
Can et al. [69]	1999	-	Vessel tracing	
Vlachos et al. [70]	2010	DR		
Adel et al. [71]	2010	DR		
Delibasis et al. [73]	2010	DR		
Yin et al. [72]	2012	HRIS		
Hassanien et al. [74]	2015	ST DR	General approaches	
Jebaseeli et al. [92]	2019	DR		
Sindh et al. [93]	2022	DR		

Note: ST, DR and CHA are abbreviations for each STARE, DRIVE and CHASE_DB1, respectively.

value, typically 255 for 8-bit images. The scaling equation is:

$$H(i) = H(i)^*(L-1)/(m \times n), \tag{2.2}$$

where L is the number of intensity levels and $(m \times n)$ is the number of pixels in the tile.

Histogram equalization: The final step is to perform histogram equalization on each tile, mapping the intensity values to their corresponding cumulative histogram values. The equation for histogram equalization is:

$$g(x, y) = H(f(x, y)) \tag{2.3}$$

where $f(x, y)$ is the original intensity value of the pixel at position (x, y).

It is important to note that CLAHE is a contrast limited method, meaning that it limits the amplification of contrasts to prevent over-amplification of noise. This is achieved by clipping the histogram of each tile at a specified clip limit before scaling. The clip limit determines the maximum number of pixels allowed to be mapped to a single intensity value [95].

In retinal vessel segmentation, CLAHE is often used as a pre-processing step to enhance the contrast of the retinal images and make the vessels more visible (Figure 2.2). This is particularly useful in cases where the vessels are not easily visible due to poor contrast in the image.

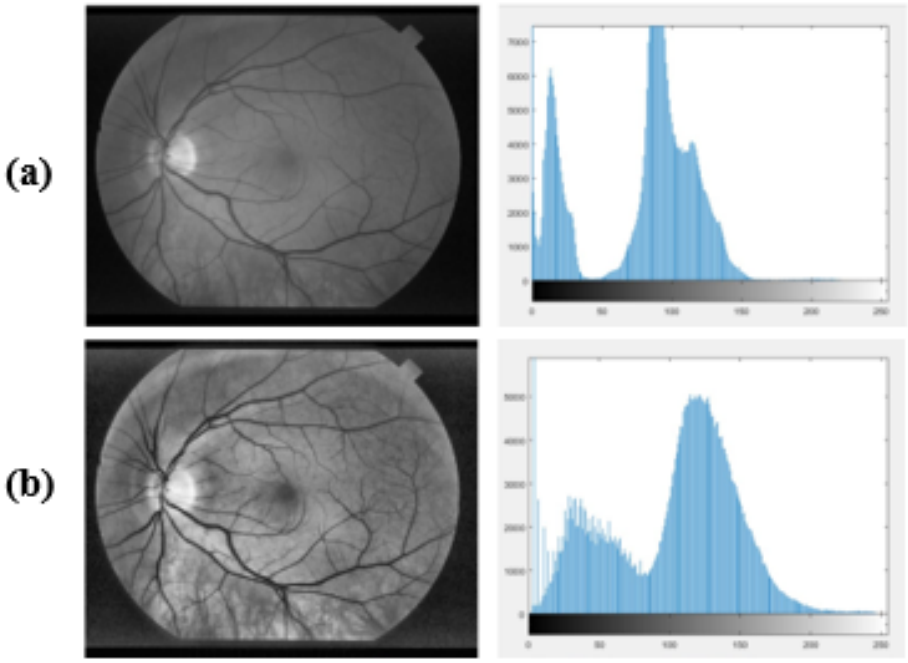

Figure 2.2: The concept of the CLAHE operation. (a) Before CLAHE. (b) After CLAHE.

2.5.2 Morphological operations

Morphological operations are techniques in image processing that analyze and change the image's structure based on its shapes and pixel relationships. They are frequently utilized in tasks such as image segmentation, noise reduction, and object extraction. Morphological image processing uses a mathematical approach to modify or extract information about the image's (I) shape and structure using a small matrix known as the structural element (S). This element is typically a binary matrix of zeros (0) and ones (1) that can be any size and shape. There are various morphological processes like dilation ($\oplus$) erosion ($\ominus$), etc. and all morphological processes are made up of a combination of these two basic operations like morphological opening ($\circ$) and closing ($\cdot$) [96], which are defined as:

2.5.2.1 Dilation

Dilation ($\oplus$) is a morphological image processing operation that is used to increase the size of the objects in an image. It works by adding pixels to the object boundaries and filling in gaps within the object. The added pixels are determined by the structural element, which is a small, pre-defined shape. During dilation, the structural element is placed over the image and moved across it as see in Figure 2.3. If any part of the structural element overlaps with an object in the image, a new pixel is added to the object in that location. The dilation equation is as follows:

$$\delta_S(I) = I \oplus S \tag{2.4}$$

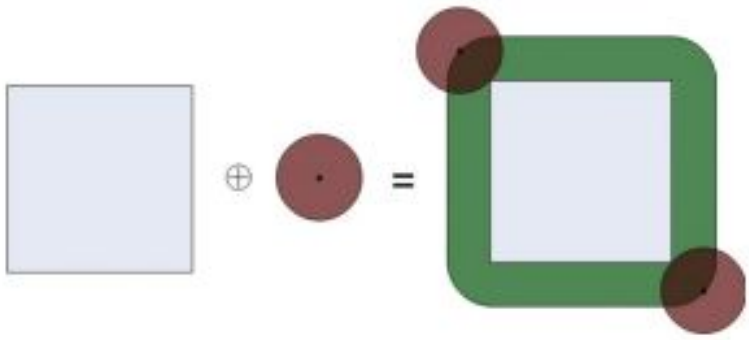

Figure 2.3: Dilation of a square by a disk element [97].

2.5.2.2 Erosion

Erosion ($\ominus$) is a morphological image processing operation that is used to shrink or thin the objects in an image. It works by removing pixels from the object boundaries and reducing the size of the objects. The pixels that are removed are determined by the

structural element, which is a small, pre-defined shape. During erosion, the structural element is placed over the image and moved across it as see in Figure 2.4. If all of the pixels under the structural element are part of the object, then the central pixel of the structural element is set to zero (or removed). The Erosion equation is as follows:

$$\epsilon_S(I) = I \ominus S \tag{2.5}$$

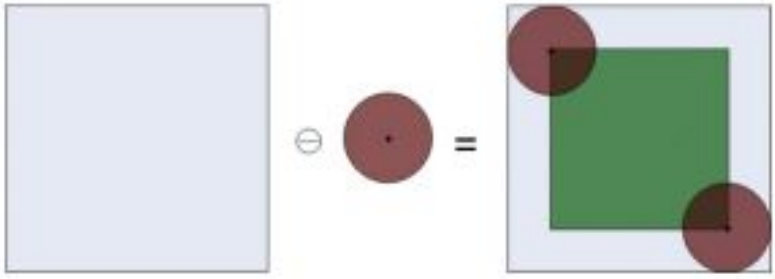

Figure 2.4: Erosion of a square by a disk element [97].

2.5.2.3 Opening

Opening ($\circ$) is a morphological image processing operation that is a combination of erosion followed by dilation. It is used to remove small, isolated pixels or noise from an image while preserving the overall shape of the objects. The opening operation works by eroding the image to remove the small, unwanted pixels, then dilating the image to restore the size of the objects to their original state (Figure 2.5). The result is an image with reduced noise and preserved object boundaries. The choice of structural element, its size and shape, and the number of iterations performed during the dilation and erosion steps determine the results of the opening operation. The opening equation is as follows:

$$\gamma_S(I) = \delta_S\left(\epsilon_S(I)\right) = (I \ominus S) \oplus S = I \circ S \tag{2.6}$$

2.5.2.4 Closing

Closing ($\cdot$) is a morphological image processing operation that is a combination of dilation followed by erosion. It is used to fill small gaps or holes within objects while preserving the overall shape of the objects. The closing operation works by dilating the image to fill in the small gaps or holes, then eroding the image to restore the object boundaries to their original state Figure 2.6. The result is an image with filled gaps and preserved object boundaries. The choice of structural element, its size and shape, and

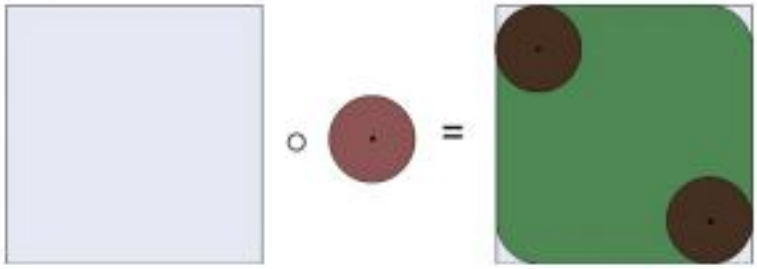

Figure 2.5: Opening of a square by a disk element [97].

the number of iterations performed during the dilation and erosion steps determine the results of the closing operation [97]. The closing equation is as follows:

$$\phi_S(I) = \epsilon_S\left(\delta_S(I)\right) = (I \oplus S) \ominus S = I \cdot S \tag{2.7}$$

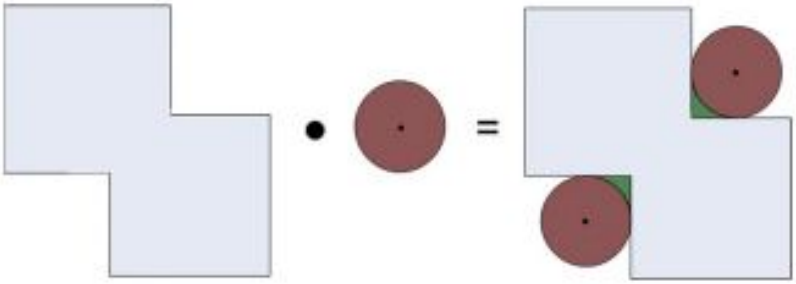

Figure 2.6: Closing of a square by a disk element [97].

In retinal vessel segmentation, morphological operations are used to remove noise and smooth the vessels, making them easier to detect and segment. The Figure 2.7 below is a simple example of applying dilatation and erosion operations to the gray retinal image by square element.

Where, the role of opening operation ($\circ$) is to keep patterns dark and features on the one hand, and to suppress bright appearances on the other hand. The closing operation ($\cdot$) preserves the bright features while suppressing the dark scores. Figure 2.8 shows an example of opening and closing operations on a retinal image. Figure 2.8(a) shows the original grayscale retinal image. Figure 2.8(b) and (c) show the results of applying opening and closing operations to the image, respectively.

2.5.3 Filtering

In retinal vessels segmentation, filtering methods are commonly used to pre-process the retinal images and enhance the visibility of the vessels. There are several filtering

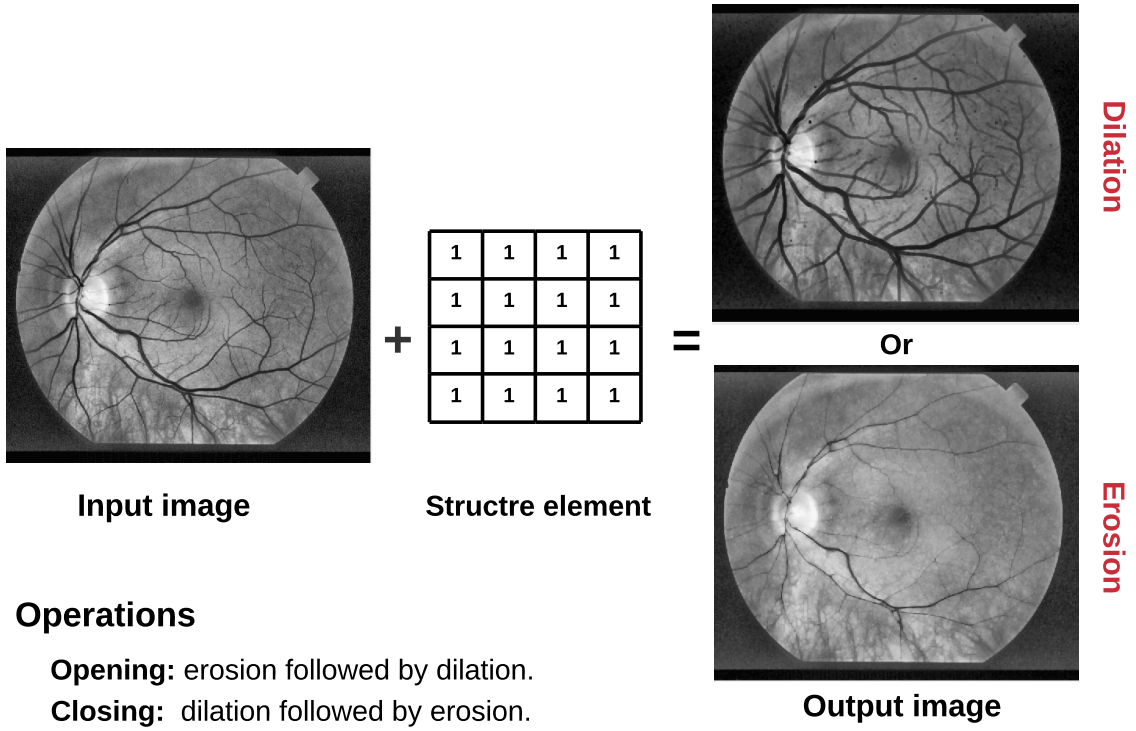

Figure 2.7: An example of morphological operation on a gray retinal image by square element.

Figure 2.8: An example of opening and closing operations on a retinal image: (a) the gray retinal image, (b) the result of the opening operation, and (c) the result of the closing operation.

methods that can be used for this purpose, such as: gaussian filtering, bilateral filtering, median filtering, anisotropic filtering, morphological filtering and, adaptive filtering, etc.

These filtering methods can be used alone or in combination to improve the visibility of the retinal vessels in the image and increase the accuracy of the segmentation results. The choice of filtering method will depend on the specific requirements of the application and the characteristics of the retinal images. In this dissertation, we will focus on morphological filtering.

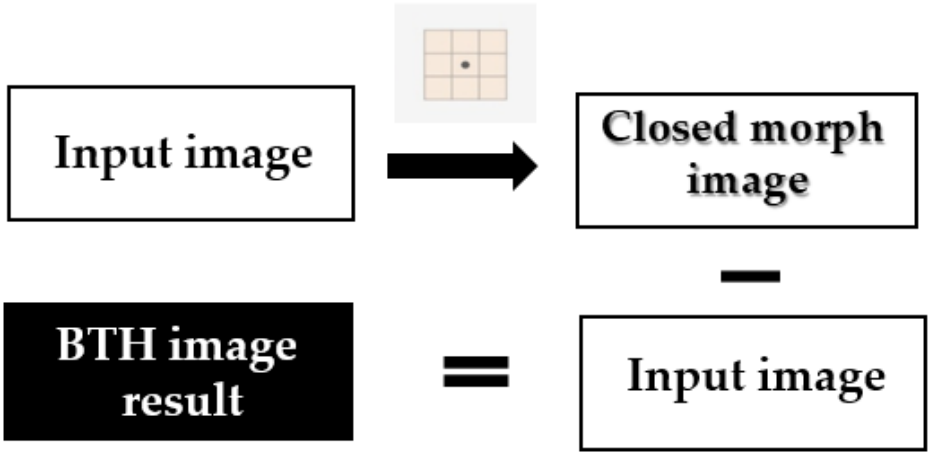

Figure 2.9: Bottom-Hat Filtering (BTH) process.

2.5.3.1 Bottom-Hat Filtering (BTH)

Bottom-Hat Filtering is used for various tasks such as background equalization, image enhancement, feature extraction, and others. The purpose of its use in improving the images of the retina is its effective ability to enhance the appearance of the eye's retinal vessels that appear black in a background that is considered less black. Bottom-hat filtering (BTH) process based on subtract the input image (I) from the result $\phi_S(I)$ of performing a morphological closing operation ($\cdot$) on the input image (I). The closure performs a dilation ($\oplus$) followed by Erosion ($\ominus$). The result is filling holes and connecting objects nearby [98]. The equation of the BTH filtering is given as follows:

$$BTH = \phi_S(I) - I \tag{2.8}$$

2.5.3.2 Bowler-Hat Filtering (BLH)

Bowler-Hat Filtering combines the outputs of morphological opening processes, which are executed on the image (I), as they are executed in two parallel tracks using different structural elements [99]. The first track uses the structural elements of the disk (S_d) with varying radii (d), is obtained:

$$I_{\text{disk}} = I \circ S_d : \forall d \in [1, d_{\max}] \tag{2.9}$$

where, (S_d) is the structural elements of diameter $d \in [1, d_{\max}]$ and $dmax$ is the expected maximum vessel size and the parameter specified by the user. The second track uses the structural elements of line ($S_{d,\theta}$) with varying radii(d) and rotation(θ), it can be

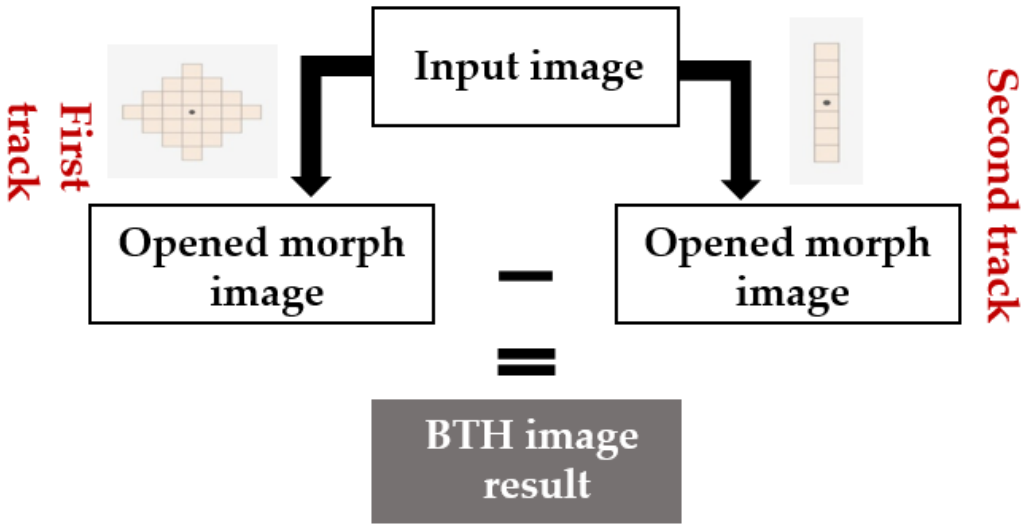

Figure 2.10: Bowler-Hat Filtering (BLH) process.

written as:

$$I_{line} = \max_{\theta} \left(\{ I \circ S_{d,\theta} : \forall \theta \} \right) : \forall d \in [1, d_{\max}] \tag{2.10}$$

where, $(S_{d,\theta})$ structural elements of line and each line is of length $d \in [1, d_{\max}]$ with a width of 1 pixel, and orientation $\theta \in [0, 180)$.

Then, the final results of the second track have been subtracted from those of the first track. The results of the two tracks are taken and linked between as follows:

$$BLH = \max_{d} \left(|I_{\text{line}} - I_{\text{disk}}| \right) \tag{2.11}$$

To test the effectiveness and the capacity of this filter in terms of promoting the appearance of the vessels, the same experiments were repeated, in the same way as with the previous filter, in order to prepare the image for the segmentation step.

2.5.3.3 Jerman Filtering

Jerman Filtering [100] is a filter that has been designed on the basis of enhancement filters [63, 101–104]. This filter is able to differentiate between different local structures, using the second order intensity derivatives for Hessian matrix at each point in the image $I(x, y)$. To intensify the local structures of different sizes, the analysis is usually carried out on a Gaussian scale space [105] of the image $I(x, y)$.

$$G(x, y, s) = \frac{1}{2\pi^2} e^{-\frac{x^2+y^2}{s^2}} \tag{2.12}$$

The Hessian matrix of $(2D)$ image $I(x, y)$ at a scale (s) is defined as:

$$H(x, s) = \left(B \cdot \frac{\partial^2}{\partial x^2} G(x, y, s) \right) * I(x, y) \tag{2.13}$$

The eigenvectors of a Hessian matrix explain the main local directions of curvature with eigenvalues (λ) corresponding to their magnitude. Selective improvement and enhancement of local image structures, based on background brightness versus shape and foreground, can be produced by studying and analyzing the magnitudes and the signs of Hessian eigenvalues. Consequently, the latter can distinguish between tube-like, blob-like, and plane-like features in a data set by decomposing the eigenvalue of the Hessian matrix. The contrast is maximized by harmonizing the enhancement function with eigenvalues, and it is performed by multiscale filtering on the extracted vessels of different scales (s). The scaling factor (s) values are determined according to the expected maximum and minimum size of the structures of interest. The modified Frangi enhancement function for $2D$ images is given by:

$$F = \exp\left(1 - \frac{(\lambda_1^2 + \lambda_2^2)}{2k^2}\right) \tag{2.14}$$

In the Frangi filtering [63], the improvement function is proportional to the magnitude of the squared eigenvalues. A modified form of Jerman filter for $(2D)$ vascularity enhancement is given by:

$$V_p = \begin{cases} 0 & \text{if } \lambda_2 \leq 0 \vee \lambda_\rho \leq 0 \\ 1 & \text{if } \lambda_2 \geq \lambda_\rho/2 > 0 \\ \lambda_2^2 \left(\lambda_\rho - \lambda_2\right) \left[\frac{3}{\lambda_2 + \lambda_\rho}\right]^3 & \text{otherwise} \end{cases} \tag{2.15}$$

where, $\lambda_\rho(s)$ define as:

$$\lambda_\rho(s) = \begin{cases} \lambda_3 & \text{if } \lambda_3 > \tau \max_x \lambda_3(x, s) \\ \tau \max_x \lambda_3(x, s) & \text{if } 0 < \lambda_3 \leq \tau \max_x \lambda_3(x, s) \\ 0 & \text{otherwise} \end{cases} \tag{2.16}$$

where (τ) is tuned to obtain the enhancement independently of the relative brightness of the structures. Often times, a value of (τ) is chosen between zero and one. A decrease in (τ) generally leads to an increase in (λ_ρ), since there is a higher probability that $(\lambda_2 > \lambda_\rho/2)$, for which (λ_ρ) is set to (1). The result is, in general, a more consistent response to the bright structures for $(\lambda < 1)$ [106]. In the case of retinal vessel segmentation, Jerman filtering is used to increase the clarity and contrast of the blood vessels in the retinal image. Table 2.3 all the symbols that are used in the equations with their meanings.

Table 2.3: Meaning of symbols.

Symbol	Meaning
B	Normalization factor
G	Gaussian function
s	Scale (size) factor
λ_1, λ_2	Eigen values
k	Controls the sensitivity
τ	Regularization factor
λ_ρ	Regularized eigen value of λ_2

2.6 Retinal vessel segmentation metrics

Retinal vessel segmentation metrics are used to assess the accuracy and reliability of a retinal vessel segmentation algorithm by comparing the segmented vessels in an image to the ground truth vessels (manually annotated vessels). The effectiveness and efficiency of any retinal vessel segmentation method can be evaluated based on its ability to correctly distinguish between the vessel and background pixels. Some of the commonly used the performance metrics in retinal vessel segmentation are:

- **TP:** Number of pixels detected in the structures of interest (retinal vessels) correctly.
- **TN:** Number of background pixels detected correctly.
- **FP:** Number of background pixels detected as the structures of interest pixels (retinal vessels).
- **FN:** Number of pixels in the structures of interest (retinal vessels) detected as background pixels.

The Table 2.4 and Figure 2.11 have been created to illustrate the concepts of these performance metrics. They demonstrate the relationship between the results of the segmentation algorithm and the ground truth images, clarifying the meaning of the performance metrics. The images in Figure 2.11(c, f) use different colors to represent different types of pixels: The white color represents true positive (TP) pixels, which correspond to blood vessels in the retina that have been correctly segmented. The purple color represents false positive (FP) pixels, which are background pixels that have been incorrectly identified as blood vessels. The green color represents false negative (FN) pixels, which correspond to blood vessels that were missed by the segmentation algorithm. By using these basic performance metrics, various metrics can be established to evaluate the comparative performance of different methods.

- **Sensitivity (Sn):** measures the proportion of true positive pixels (correctly identified vessels) to the total number of ground truth vessels. Sensitivity ranges from

Table 2.4: Semantics of the parameters between an algorithm's results and the ground truth.

	Ground truth	
Algorithm	Vessel	No vessel
Vessel	True Positive	False Positive
No vessel	False Negative	True Negative

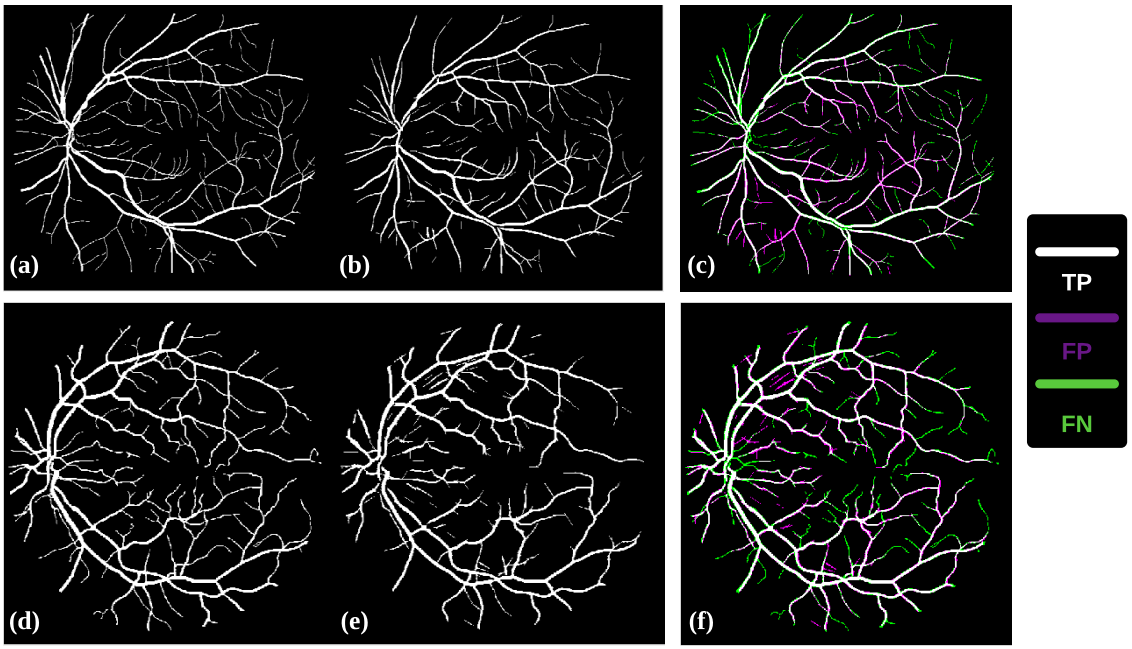

Figure 2.11: A comparison between the image obtained through a segmentation method and the ground truth in the STARE and DRIVE databases. (a,d) ground truth in STARE and DRIVE databases, respectively, (b,e) segmentation images results with a segmentation method, and (c,f) images of congruence, and the difference between ground truth and segmentation images results.

0 to 1, with 1 indicating perfect sensitivity (all vessels are correctly identified), and 0 indicating poor sensitivity (no vessels are correctly identified). A high sensitivity indicates that the retinal vessel segmentation algorithm has a low rate of false negative errors (vessels incorrectly identified as non-vessels), while a low sensitivity indicates that the algorithm has a high rate of false negative errors. The equation for sensitivity (Sn) is:

$$Sn = \frac{TP}{TP + FN} \tag{2.17}$$

- **Specificity (SP):** is another performance metric used in the evaluation of retinal vessel segmentation algorithms. It measures the proportion of true negative pixels (correctly identified non-vessel pixels) to the total number of ground truth non-vessel pixels. Specificity also ranges from 0 to 1, with 1 indicating perfect

specificity (all non-vessels are correctly identified), and 0 indicating poor specificity (no non-vessels are correctly identified). A high specificity indicates that the retinal vessel segmentation algorithm has a low rate of false positive errors (non-vessels that are incorrectly identified as vessels), while a low specificity indicates that the algorithm has a high rate of false positive errors. In other words, specificity is a measure of how well the algorithm can correctly identify regions that are not vessels, which is also an important aspect of its performance. The equation for Specificity (SP) is:

$$Sp = \frac{TN}{TN + FP} \tag{2.18}$$

- **Accuracy (Acc):** refers to the proportion of correctly classified pixels in an image, either as vessels or non-vessels. Accuracy is calculated as the ratio of the number of correctly classified pixels to the total number of pixels in the image. High accuracy indicates that the retinal vessel segmentation algorithm is able to correctly identify the majority of vessels in the image, while low accuracy indicates that the algorithm has difficulty distinguishing between vessels and non-vessels. The equation for Accuracy (Acc) is:

$$Acc = \frac{TP + TN}{TP + TN + FN + FP} \tag{2.19}$$

- **Matthews Correlation Coefficient (MCC):** ranges from -1 to 1, with 1 indicating perfect prediction, -1 indicating perfect mis-prediction, and 0 indicating random prediction. Unlike other metrics such as accuracy, precision, and recall, MCC takes into account both false positive and false negative errors, making it a more robust measure of performance when the distribution of vessels and non-vessels in an image is imbalanced. The equation for Matthews Correlation Coefficient (MCC) is:

$$MCC = \frac{TP \cdot TN - FP \cdot FN}{\sqrt{(TP + FP) \cdot (TP + FN) \cdot (TN + FP) \cdot (TN + FN)}} \tag{2.20}$$

- **Precision (Pr):** measures the proportion of true positive pixels (correctly identified vessels) to the total number of pixels identified as vessels by the algorithm. The equation for Precision (Pr) is:

$$Pr = \frac{TP}{TP + FP} \tag{2.21}$$

- **$\mathbf{F}_1$ score:** is the harmonic mean of precision and recall, and it ranges from 0

to 1, with 1 being the best possible score. An F_1 score of 1 indicates that the algorithm has both perfect precision and recall, while an F_1 Score of 0 indicates that the algorithm has poor precision and recall. The equation for F_1 score is:

$$F_1 = \frac{2TP}{2TP + FP + FN} = 2 \times \frac{Sn \times Pr}{Sn + Pr} \tag{2.22}$$

These metrics provide valuable information about the performance of a retinal vessel segmentation algorithm and can be used to guide further improvements and optimizations.

2.7 Conclusion

This chapter has carried out an extensive examination of the literature on the methods used for segmenting blood vessels in the eye. The methods were critically evaluated to identify their strengths and weaknesses, with particular emphasis on the enhancement methods relevant to our contributions to the field. Additionally, the different databases used for vessel segmentation were described in detail. Furthermore, the metrics used to evaluate the proposed methods and verify their effectiveness were discussed. The literature review provided in this chapter offers valuable insights into the current state of the art in this field. It lays the foundation for further advancements and explorations in the future.

Contributions

Chapter 3

Retinal image segmentation using improved FCM algorithms: performance analysis

3.1 Introduction

The blood vessels in retinal images are essential structures and critical indicators for diagnosing eye diseases. However, their classification presents challenges such as low contrast in the fundus image, varying background lighting, and noise. Fuzzy C-Means (FCM) clustering is a widely used algorithm in medical image segmentation because of its effectiveness. This has led to the development of various FCM method derivatives for improved noise robustness and efficiency.

This chapter aims to assess the performance of these improved FCM algorithms and recommend the best ones for retinal blood vessel segmentation. The study evaluates the following FCM algorithm derivatives for retinal blood vessel segmentation: FCM, EnFCM, SFCM, FGFCM, FRFCM, DSFCM_N, FCM_SICM, and SSFCA. The evaluation focuses on noise robustness, blood vessel segmentation performance, and running time. It uses synthetic images with varying noise levels and real images from the STARE and DRIVE databases. The results and observations are discussed at the end. It is mentioned that the results of this study have been published in an international journal [107].

3.2 Preliminary

Clustering is a technique used in image segmentation to group similar pixels into disjoint clusters. The number of clusters is either set or determined through a criterion. Clustering is unsupervised and does not use labels or prior knowledge. The resulting clusters represent regions or objects in the image. Common algorithms include k-means,

hierarchical clustering, and fuzzy c-means. In medical imaging, clustering algorithms have been used for tasks like blood vessel segmentation and tissue classification, providing more accurate results than manual segmentation. In this context, some comparative studies of different clustering algorithms on retinal image segmentation are conducted. Wiharto et al. [108] compared the effectiveness of fuzzy c-means and k-means for retinal blood vessel segmentation and found that fuzzy c-means performed better in terms of AUC. Our paper [109] studied the ability of various clustering algorithms to segment retinal images and isolate blood vessels. The process involved two phases: pre-processing to enhance image contrast and clustering segmentation of the pre-processed image. The algorithms studied were k-means (KM), k-medoids (KD), Gaussian Mixture Model (GMM), and fuzzy c-means (FCM). The results show that KD had better results on the DRIVE database and FCM on the STARE database in terms of accuracy. Depending on these studies, FCM is more flexible in cluster formation and better suited for more complex image segmentation tasks. Hence, we have chosen FCM for our study based on these findings. The Appendix A contains a detailed presentation of the work, allowing for thorough review and evaluation.

The fuzzy set theory suggested by Zadeh [110] provides a mighty tool for such soft partitioning. Based on this theory, Dunn [111] developed Fuzzy c-means clustering, and then Bezdek et al. [112] adapted it for image segmentation. The FCM algorithm, while widely used, has some limitations in image segmentation. To address these issues, various extensions of the FCM algorithm have been proposed. These extensions of the FCM algorithm can significantly improve its performance in image segmentation and other pattern recognition tasks, depending on the type of images and the targeted area. However, they may also increase the complexity of the algorithm and introduce additional computational overhead. This section presents some extensions of the FCM algorithm.

3.2.1 FCM

In image segmentation, FCM can categorize pixels into distinct regions or objects based on features such as color and intensity. The membership grades allow for a soft segmentation map to be generated, resulting in smooth transitions between regions in the image. The effectiveness of the FCM algorithm in finding an optimal solution is influenced by several factors, including the starting positions of the cluster centers and the method used to calculate the membership degree for each data point. The standard FCM method randomly initializes the cluster centers and only considers the gray feature in calculating the membership measure. During the clustering process, each data point is assigned a membership grade, indicating its degree of association with each cluster. These grades are used to recalculate the cluster centroids[113, 114].

Let's consider an image I with P pixels. Since each image pixel often implies a set of attributes (variables), I can be formulated as $\boldsymbol{X} = \{\boldsymbol{x}_1, \boldsymbol{x}_2, \cdots, \boldsymbol{x}_P\} \subset \mathbb{R}^P$. The FCM algorithm divides X into several clusters C by minimizing the following objective function:

$$\begin{cases} J_{FCM} = \sum_{i=1}^{c} \sum_{j=1}^{P} u_{ij}^{m} \left\| \boldsymbol{x}_j - \boldsymbol{v}_i \right\|^2 \\ \qquad Subject\ to \\ \sum_{i=1}^{c} u_{ij} = 1, \ \text{for } j \in \{1, 2, \cdots, P\}, \ \text{with } 0 \leq u_{ij} \leq 1 \end{cases} \tag{3.1}$$

where,

u_{ij} : is the degree of membership of x_j in the cluster c_i.

m : is the fuzzification exponent $(m > 1)$.

x_j : is the i^{th} of d-dimensional measured data.

v_i : is the d-dimension center of the cluster.

$\| \cdot \|$: is the Euclidean distance.

The minimization of Equation 3.1 can be realized by iteratively updating the partition matrix and the cluster centers:

$$u_{ij}^{m} = \frac{1}{\sum_{q=1}^{c} \left(\frac{\|\boldsymbol{x}_j - \boldsymbol{v}_i\|}{\|\boldsymbol{x}_j - \boldsymbol{v}_q\|} \right)^{\frac{2}{m-1}}} \text{ and } v_i = \frac{\sum_{j=1}^{n} u_{ij}^{m} \cdot \boldsymbol{x}_j}{\sum_{j=1}^{n} u_{ij}^{m}} \tag{3.2}$$

By presetting a Non-negative threshold ε, (FCM) [1] iterates until $\max_{ij} \left\{ \left\| u_{ij}^{(t+1)} - u_{ij}^{(t)} \right\| \right\} < (\varepsilon)$ has been met. Here, t is an iteration index. This procedure converges to a local minimum or a saddle point of J_{FCM}.

3.2.2 EnFCM

The Enhanced fuzzy c-means (EnFCM)[2] algorithm was proposed by Szilagyi et al. [115] on the basis of the research findings of [116], originally developed for the segmentation of MR brain images. It executes clustering based on gray-level histograms (l) rather than pixels of a summed image, which lessens the computational complexity. A linearly-weighted sum image (ξ) is formed in advance from the original image and its local neighbor average image in terms of:

$$\xi_l = \frac{1}{\alpha + 1} \left(x_l + \frac{\alpha}{N_R} \sum_{j \in N_l} x_j \right) \tag{3.3}$$

where,

ξ_l : is the gray value of the l^{th} pixel of the image (ξ).

[1] https://fr.mathworks.com/help/fuzzy/fcm.html

[2] https://github.com/marearth/fcm_m

x_j : is the neighbors of x_l.
α : is the control of the effect of the neighbors' terms (weight factor).
N_l represents the set of neighbors x_j falling into a window around x_l. Next, the clustering process is running on the gray level histogram of the newly formed image (ξ). As a result, the objective function, in this case is represented as:

$$\begin{cases} J_{EnFCM} = \sum_{i=1}^{c} \sum_{l=1}^{q} \gamma_l u_{il}^m \left(\xi_l - v_i\right)^2 \\ \qquad Subject\ to \\ \sum_{l=1}^{q} \gamma_l = N \text{ and } \sum_{i=1}^{c} u_{il} = 1 \end{cases} \tag{3.4}$$

where,
v_i : is the prototype of the i^{th} cluster (c).
u_{il}: is the fuzzy membership of gray value l with respect to cluster i.
q : is the number of gray levels of the addressed image, which usually much less N.
γ_l : is the total number of pixels with a gray value of l.
The J_{EnFCM} is minimized using the following equations to calculate the membership partition matrix and the cluster centers:

$$u_{il} = \left[\sum_{j=1}^{c} \left(\frac{\xi_l - v_i}{\xi_l - v_j} \right)^{\frac{2}{m-1}} \right]^1 \tag{3.5}$$

$$v_i = \frac{\sum_{l=1}^{q} \gamma_l u_{il}^m \xi_l}{\sum_{l=1}^{q} \gamma_l u_{il}^m}. \tag{3.6}$$

The iterative process of the EnFCM algorithm is similar to the FCM algorithm, but it is applied to the linearly-weighted sum image (ξ) by using Equation 3.5 and Equation 3.6. EnFCM does not automatically choose the weight factor value to achieve accurate results for segmenting MR images with noise content and MR sequences. To avoid this, some recent research have been used multi-objective particle swarm optimization to control the weight parameter, leading to maximum segmentation accuracy [117].

3.2.3 SFCM

Chuang et al. [118] suggested a Spatial fuzzy c-means (SFCM)[3] algorithm in which spatial information can be integrated into fuzzy membership functions directly using:

$$h_{ij} = \sum_{k \in N_b} u_{ik} \tag{3.7}$$

[3] https://fr.mathworks.com/matlabcentral/fileexchange/31068-spatial-fuzzy-clustering-and-level-set-segmentation

where,
N_b : is the local window (w) centered around the image pixel n.
u_{ik} :is the memberships of x_j in to i^{th} cluster.
h_{ij} : is the probability that pixel x_j belongs to i^{th} cluster.
The memberships u_{ij} is updated using the following relationships:

$$u_{ij} = \frac{u_{ij}^p h_{ij}^q}{\sum_{k=1}^{c} u_{kj}^p h_{kj}^q} \tag{3.8}$$

where,
p, q : two parameters controlling the respective contribution. The weighted u_{ij} and the centroid v_i are updated as usual according to Equation 3.2. In the literature, the SFCM algorithm has been presented for the first time to segment brain T1 and T2-weighted MR images. Similarly, this algorithm has been used for segmenting cerebrospinal fluid (CSF), fat, gray matter (GM), white matter (WM), air, and bone. In addition, SFCM has been combined with level set method to increase its effectiveness in automated medical image segmentation [119].

3.2.4 FGFCM

Cai et al. [120] proposed the fast generalized fuzzy c-means clustering (FGFCM) [4] that included a new factor S_{ij} as a local similarity measure. Its permits to ensure both detail preservation and noise-immunity for image segmentation. Another advantage, it dispenses with the empirically-adjusted parameter α that EnFCM requires, and it ultimately achieves gray-level histogram clustering. Its definition is given as follows:

$$S_{ij} = \begin{cases} \exp\Big\{-\max(|p_i - p_j|, |q_i - q_j|)/\lambda_s - \|x_i - x_j\|^2/\lambda_g \sigma_i^2\Big\} & i \neq j\,, \\ 0 & i = j\,. \end{cases} \tag{3.9}$$

where,
i^{th} : is the center of the local window.
j^{th} : is the set of the neighbors falling into the window around the i^{th} pixel.
p_i, q_i : is the coordinates of pixel i.
x_i : is the gray level the value i.
λ_s, λ_g: two scale factors playing a role similar to factor α in EnFCM.
σ_i is a function of the local density surrounding the central pixel, and its value indicates

[4] https://github.com/marearth/fcm_m

the local window's gray value homogeneity degree. σ_i is defined as:

$$\sigma_i = \sqrt{\frac{\sum_{j \in N_i} \|x_i - x_j\|^2}{N_R}} \tag{3.10}$$

FGFCM algorithm integrates local and gray level information Equation 3.9 inside the objective function producing a new image (ξ_i) defined as follows:

$$\xi_i = \frac{\sum_{j \in N_i} S_{ij} x_j}{\sum_{j \in N_i} S_{ij}} \tag{3.11}$$

where,
ξ_i : is the gray level value of the i^{th} pixel of the image ξ.
x_j : is the gray level value of the neighbors of window center.
N_i : is the set of neighbors falling in the local window.
S_{ij} : is the local similarity measure between the i^{th} and the j^{th} pixel.
FGFCM has been tested on a real brain MR image in order to study the effect of the window size w on the algorithm's effectiveness. A local window of 5×5 has proven to be effective [120].

3.2.5 FRFCM

Lei et al. [121] suggested a fast and robust fuzzy c-means clustering algorithm (FRFCM)[5], which is based on morphological reconstruction and membership filtering. They could be considered as pre-processing and post-processing, respectively. FRFCM is applied to gray level histogram in a similar manner to EnFCM. For the data point ($x_j = R^C(x)$) and its membership value (u_{ij}), the objective function is minimized using the Lagrange function, where ($R^C(x)$) is the morphological closing reconstruction of original image (x). The objective function is written as follows:

$$J_{FRFCM} = \sum_{j=1}^{N} \sum_{i=1}^{c} \gamma_j u_{ij}^m \|x_j - y_i\| - \lambda \left(\sum_{i=1}^{c} u_{ij} - 1 \right) \tag{3.12}$$

where,
γ_l : is the number of the pixels having the gray value equal to l.
u_{ij} : is the fuzzy membership of gray value l.
x_j : is the gray level of an image that has been reconstructed using MR ($R^C(x)$).
y_i : is the prototype of the i^{th} cluster (c).
λ : is a Lagrange multiplier.
Instead of using the distance vector (between the pixel values and cluster centers), a faster membership filtering is used. The following relationships are used to update the

[5] https://github.com/jiaxhsust/Significantly-Fast-and-Robust-FCM-Based-on-Morphological-Reconstruction-and-Membership-Filtering

memberships filtering:

$$u_{ij} = \|x_j - y_i\|^{-2/(m-1)} / \sum_{r=1}^{c} \|x_j - y_r\|^{-2/(m-1)} \tag{3.13}$$

The cluster centers (y_i) is updated using the following relationships:

$$y_i = \sum_{j=1}^{N} \gamma_j u_{ij}^m x_j / \sum_{j=1}^{N} \gamma_j u_{ij}^m \tag{3.14}$$

Motivated by the excellent performance of the FRFCM, [122] have suggested an optical selective encryption scheme for the medical image based on the FRFCM algorithm and face biometric.

3.2.6 DSFCM_N

In deviation-sparse fuzzy c-means with neighbor information (DSFCM_N) [6] algorithm, Zhang et al. [123] take into account the deviations e_k between measured values x_k and theoretical values $x_{\Delta k}$. Thus, the accuracy of the calculated deviations would have a great influence on the clustering results. To distinguish noise from outliers, the authors imposed sparsity constraint on the deviations between measured and theoretical values. Moreover, this sparsity could also ensure that the deviations would not diverge. The objective function is denoted as:

$$J_{DSFCM\_N} = \sum_{i=1}^{c}\sum_{j=1}^{N} u_{ij}^m \left(\sum_{k\in N_j} \frac{1}{1+d_{kj}} \|x_k - e_k - y_i\|_2^2 \right) + \sum_{t=1}^{l} \lambda_t \sum_{k\in N_j} \frac{\sum_{j=1}^{N} \|e_{jt}\|^p}{1+d_{kj}} \tag{3.15}$$

where,

k : is the neighbor of pixel j in the local window N_j.

N_j : is the local window centralized in j.

N_k : is the neighbor pixels including j.

d_{kj} : is the Euclidean distance between k and j.

e_k : is the deviation vector of pixel k.

l : is the dimension of the data.

λ : is a regulating vector of length l.

e_{jt} : represents the difference between x_{jt} and its theoretical value.

The deviation matrix (e_{jt}) is updated using the following relationships:

[6] https://github.com/zhangyuxuan1996/DSFCM_N

$$e_{jt} = \frac{\text{soft}\left(\sum_{i=1}^{c}\sum_{k\in N_j}\left(\frac{\left(u_{ik}\right)^m\left(x_{jt}-v_{iq}\right)}{1+d_{kj}}\right), \frac{\lambda_q/2}{\sum_{k\in N_j}\left(1+d_{kj}\right)}\right)}{\sum_{i=1}^{c}\sum_{k\in N_j}\frac{1}{1+d_{kj}}\left(u_{ik}\right)^m} \tag{3.16}$$

The memberships (u_{ij}) is updated using the following relationships:

$$u_{ij} = \left(\sum_{r=1}^{c}\left(\sum_{k\in N_j}\frac{1}{1+d_{kj}}\left\|x_k - e_k - y_i\right\|^2 / \sum_{k\in N_j}\frac{1}{1+d_{kj}}\left\|x_k - e_k - y_r\right\|^2\right)^{1/m-1}\right)^{-1} \tag{3.17}$$

The cluster centers (y_i) is updated using the following relationships:

$$y_i = \left(\sum_{j=1}^{N} u_{ij}^m \sum_{k\in N_j}\frac{1}{1+d_{kj}}\left(x_k - e_k\right)\right) / \sum_{k\in N_j}\frac{1}{1+d_{kj}}\sum_{j=1}^{N} u_{ij}^m \tag{3.18}$$

Real brain MR images were used by [123] to test the effectiveness of DSFCM_N algorithm for segmenting white matter (GM), grey matter (GM), and cerebrospinal fluid (CSF).

3.2.7 FCM_SICM

Robust fuzzy c-means clustering algorithm with adaptive spatial, constraint, and membership (FCM_SICM)[7] linking for noisy image segmentation has been proposed by [124]. Firstly, the fast bilateral filter is applied to obtain local spatial and intensity information. Secondly, an absolute difference image between the original image and the bilateral filtered one is used, and the reciprocal of the different image whereas the different image itself constrain conventional FCM, as well as, the local spatial and intensity information, respectively. Finally, membership linking is reached by summing each membership degree calculated from the earlier iteration within every cluster in squared logarithmic form as the denominator of the objective function as follows:

$$\begin{cases} J_{FCM\_SICM}^{(t)} = \sum_{i=1}^{K}\dfrac{\sum_{j=1}^{N}\frac{1}{\Delta y_j}\left(u_{ij}^{(t)}\right)^m\left\|y_j - c_i^{(t)}\right\|^2 + \sum_{j=1}^{N}\Delta y_j\left(u_{ij}^{(t)}\right)^m\left\|\bar{y}_j - c_i^{(t)}\right\|^2}{\ln^2\left(\sum_{e=1}^{N}u_{ie}^{(t-1)}+1\right)} \\ \quad Subject\ to \\ \quad \sum_{i=1}^{K}u_{ij}^{(t)} = 1 \end{cases} \tag{3.19}$$

where, I is the original image, I' is the bilateral filtered image. $\triangle I$ is the difference between I and I' and $\triangle y_j$ is the j^th value of $\triangle I$.

[7] https://github.com/wqshmzh/FCM_SICM-Algorithm

u_{ie} : is the memberships degrees computed from previous iteration.
The center (c_i) is updated using the following relationships:

$$c_i^{(t)} = \frac{\sum_{j=1}^{N} \left(\frac{1}{\Delta y_j} y_j + \Delta y_j \bar{y}_j\right) \left(u_{ij}^{(t)}\right)^m}{\sum_{j=1}^{N} \left(\frac{1+\Delta y_j^2}{\Delta y_j}\right) \left(u_{ij}^{(t)}\right)^m} \tag{3.20}$$

The membership (u_{ij}) is updated using the following relationships:

$$u_{ij}^{(t)} = \frac{1}{\sum_{r=1}^{K} \left[\frac{\frac{1}{\Delta y_j} \left\| y_j - c_i^{(t)} \right\|^2 + \Delta y_j \left\| \bar{y}_j - c_i^{(t)} \right\|^2}{\frac{\ln^2\left(\sum_{e=1}^{N} u_{ie}^{(t-1)} + 1\right)}{\frac{1}{\Delta y_j} \left\| y_j - c_r^{(t)} \right\|^2 + \Delta y_j \left\| \bar{y}_j - c_r^{(t)} \right\|^2} \ln^2\left(\sum_{e=1}^{N} u_{re}^{(t-1)} + 1\right)} \right]^{\frac{1}{m-1}}} \tag{3.21}$$

3.2.8 SSFCA

Self-Sparse Fuzzy Clustering Algorithm (SSFCA)[8] was proposed by Jia et al. [125]. This algorithm is based on integrating into the objective function a regularization under Gaussian metric. The objective is to obtain fuzzy membership with sparsity, which reduces a proportion of noisy features and improves clustering results. The final objective function is defined as:

$$J_{SSFCA} = \sum_{i=1}^{c} \sum_{j=1}^{n} u_{ij} \Phi' \left(\boldsymbol{x}_j \mid \boldsymbol{v}_i, \Sigma_i\right) + \gamma \sum_{i=1}^{c} \sum_{j=1}^{n} u_{ij}^2 \tag{3.22}$$

where,
γ : is a balance factor used for controlling the sparsity of memberships.
Σ_i : is covariance matrix.
$\Phi' \left(\boldsymbol{x}_j \mid \boldsymbol{v}_i, \Sigma_i\right)$: is the distance function between x_j and v_i.

By setting the value of (γ), fuzzy memberships with varying degrees of sparsity can be obtained using the optimization approach suggested in [126] to to solve Equation 3.22. The memberships matrix can be rewritten as:

$$\begin{cases} J_{SSFCA} = \min \left\| u_{ij} - h_{ij} \right\|^2 \\ \qquad Subject\ to \\ h_{ij} = -\Phi' \left(\boldsymbol{x}_j \mid v_i, \Sigma_i\right) / 2\gamma \end{cases} \tag{3.23}$$

h_{ij} : the fuzzy memberships with different degrees of sparsity.

[8] https://github.com/jiaxhsust/Robust-Self-Sparse-Fuzzy-Clustering-for-Image-Segmentation

The cluster centers is updated using the following relationships:

$$\boldsymbol{v}_i = \frac{\sum_{j=1}^{n} u_{ij} \boldsymbol{x}_j}{\sum_{j=1}^{n} \boldsymbol{u}_{ij}} \tag{3.24}$$

The covariance matrix is updated using the following relationships:

$$\Sigma_i = \frac{\sum_{j=1}^{n} u_{ij} \left(\boldsymbol{x}_j - \boldsymbol{v}_i\right)^T \left(\boldsymbol{x}_j - \boldsymbol{v}_i\right)}{\sum_{j=1}^{n} u_{ij}} \tag{3.25}$$

In summary, after discussing the FCM algorithms used in this study, it is important to note the following points:

- All the improved FCM algorithms are built on fuzzy theory and have some common parameters such as fuzzy exponent, convergence threshold, and maximum iteration number. However, the specific parameters for each algorithm need to be individually adjusted to achieve optimal results.
- The improved FCM algorithms are designed to overcome the limitations of the conventional FCM, such as the neglect of spatial information in the objective function.
- SFCM, FGFCM, FRFCM, and FCM_SICM algorithms have a similar approach in that they include local spatial information in their objective function and use a fixed-sized window to enhance image segmentation.
- On the other hand, DSFCM_N and SSFCA algorithms incorporate deviation and sparsity into their objective function, making them more resilient to noise.
- To address the challenge of high computational complexity, EnFCM performs clustering on gray levels and FRFCM uses morphological reconstruction and membership filtering, resulting in faster processing time.

3.3 Noise robustness analysis

In this study, our objective is to comprehensively assess the ability of the improved FCM algorithms to handle noise and other challenging factors in image segmentation. For this purpose, we have selected a synthetic image as the test case and analyzed several variants of the FCM algorithm. These variants include FCM, EnFCM, SFCM, FGFCM, FRFCM, DSFCM_N, FCM_SICM, and SSFCA. Each of these algorithms has its strengths and limitations regarding noise robustness and performance, and our experiments aim to quantify and systematically compare these attributes.

3.3.1 Synthetic image

The synthetic images created by computers serve a valuable purpose in computer vision tasks, such as image classification, instance segmentation, and anomaly detection. This synthetic image is designed to have a specific size, in this case, 269×260, and is comprised of three classes, represented by tree intensity values of 75, 100, and 175 as shown in Figure 3.1(a) [121].

In order to conduct a comprehensive study, the synthetic image is intentionally corrupted with varying degrees of two types of noise: Gaussian (2% & 4% intensity) and Salt & Pepper (3% & 6% intensity). This allows us to evaluate the impact of these noises on the performance of algorithms.

- **Gaussian** is a type of random noise that follows a normal distribution and is often added to images to simulate real-world conditions. This type of noise is characterized by a mean value and a standard deviation, affecting the image pixels randomly. In the context of our study, Gaussian noise is added to the synthetic image at varying levels to assess the impact on the performance of improved FCM algorithms (see Figure 3.1(b)).
- **Salt & Pepper** also known as impulse noise, is another type of random noise that is added to images. Unlike Gaussian noise, this type of noise affects only a few pixels in the image and is characterized by random black and white pixels, hence the name "Salt & Pepper." This type of noise is used to simulate real-world scenarios where some pixels in an image may be corrupted or lost. In our study, we introduce Salt & Pepper noise at various levels to the synthetic image to observe its impact on the performance of computer vision algorithms (see Figure 3.1(c)).

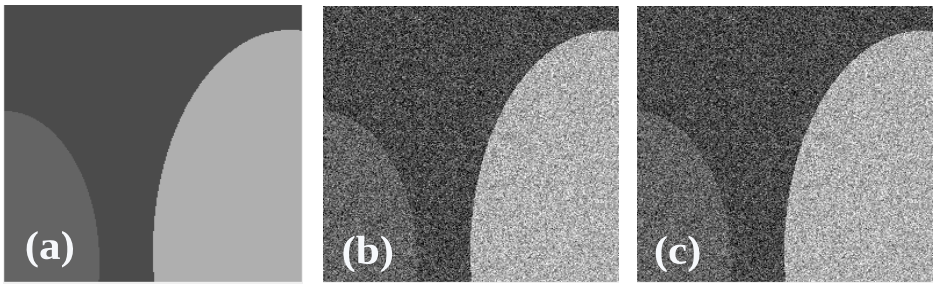

Figure 3.1: Synthetic image with two types of noise. (b) with Gaussian noise. (b) with Salt & Papper noise.

3.3.1.1 Parameter setting

The parameters for all improved FCM Algorithms were set as follows: the fuzzy exponent was set to $m = 2$ the convergence threshold was set to $e = 10^5$, and the

maximum iteration number was set to $T = 100$. These parameters were carefully selected through numerous experiments to attain optimal results for all improved FCM algorithms. The individual parameters for each algorithm are presented Table 3.1. The experiments were conducted on a workstation with a 2.5 GHz Intel® Core (TM) i5-2520 processor and 2G of memory, and computed using MATLAB software.

Table 3.1: Parameters used in all improved FCM.

Algorithms	**Parameters**
EnFCM	$\alpha = 4.2$
SFCM	$w = 5$, $p = 1$, $q = 1$
FGFCM	$\alpha\,(\lambda_s, \lambda_g) = 6.2$
FRFCM	w = 1, se = 1, shape = disk
DSFCM_N	w = 3, $\lambda = 10$
FCM_SICM	$\sigma\_d = 0.5$, $\sigma\_r = 2$
SSFCA	$\gamma = 3$

3.3.1.2 Metrics

In order to evaluate the effectiveness of retinal blood vessels, we will employ several metrics, including Precision (Pr), Sensitivity (Sn), Specificity (SP), F1 score, and Accuracy (Acc), which are outlined in section 2.6. These metrics will enable us to distinguish the blood vessels from the surrounding tissue accurately. By utilizing these metrics, we can precisely identify and differentiate the blood vessels, allowing us to make informed decisions during the segmentation process. Using these metrics will guarantee efficient and effective segmentation of the blood vessels.

3.3.2 Results and Discussion

The objective of this subsection is to showcase the results and analysis of the validation experiments. Firstly, the segmentation outcomes achieved from various algorithms are illustrated in Figure 3.2 and Figure 3.3. Moreover, a comprehensive overview of the metric scores is presented in Table 3.2 and Table 3.3.

A closer look at Table 3.2 and Figure 3.2 reveals that the FRFCM and DSFCM_N algorithms perform better in terms of segmentation results on synthetic images corrupted by Gaussian noise with 2% and 4% intensity. This is attributed to the fact that the FRFCM algorithm includes local spatial information by incorporating morphological reconstruction, ensuring noise immunity and detail preservation. On the other hand, the DSFCM_N algorithm reduces noise by considering the sparsity of deviations between measured and theoretical values, without imposing any limitations on artifacts,

resulting in a better visual outcome.

Furthermore, when the improved FCM algorithms were tested on synthetic images corrupted by Salt & Pepper noise with 3% and 6% intensity, the results shown in Table 3.3 and Figure 3.3 demonstrate that the FRFCM and DSFCM_N algorithms are more effective. This confirms the findings from the first experiment, further solidifying the superiority of the FRFCM and DSFCM_N algorithms in terms of segmentation results on images corrupted by Gaussian and Salt & Pepper noise.

Table 3.2: The metrics values achieved by different algorithms on the synthetic images corrupted by various ratios of Gaussian noise.

Gaussian noise						
Ratio	Algorithms	Pr	Sp	Sn	F_1	Acc
2%	FCM	0.9380	0.9711	0.7269	0.8793	0.8191
	EnFCM	0.9848	0.9914	0.9225	0.9655	0.9526
	SFCM	0.95861	0.9794	0.7890	0.9079	0.8656
	FGFCM	0.9855	0.9917	0.9342	0.9701	0.9592
	FRFCM	**0.9991**	**0.9994**	**0.9962**	**0.9982**	**0.9977**
	DSFCM_N	**0.9951**	**0.9970**	**0.9986**	**0.9976**	**0.9968**
	FCM_SICM	0.9465	0.9759	0.7082	0.8753	0.8102
	SSFCA	0.7305	0.8193	0.8137	0.8172	0.7698
4%	FCM	0.8512	0.9361	0.6066	0.8123	0.7084
	EnFCM	0.9564	0.9786	0.7792	0.9037	0.8588
	SFCM	0.8857	0.9521	0.6159	0.8258	0.7266
	FGFCM	0.9588	0.9795	0.7909	0.9086	0.8668
	FRFCM	**0.9928**	**0.9957**	**0.9749**	**0.9879**	**0.9838**
	DSFCM_N	**0.9762**	**0.9854**	**0.9900**	**0.9872**	**0.9831**
	FCM_SICM	0.8563	0.9401	0.5926	0.8095	0.7005
	SSFCA	0.7300	0.8175	0.8199	0.8184	0.7724

3.4 Blood vessel segmentation analysis

This section provides a quantitative comparison of the effectiveness and speed of vessel segmentation using improved FCM algorithms. We compare the performance of these algorithms to evaluate their suitability for this task. The analysis focuses on several key metrics, including accuracy, sensitivity, specificity, and computational time. By comparing the results of the different algorithms, we aim to identify the most effective approach for vessel segmentation.

3.4.1 Methodology

The methodology for analyzing the enhanced FCM algorithms is outlined in this section. As previously stated, several variations of the FCM clustering algorithm were

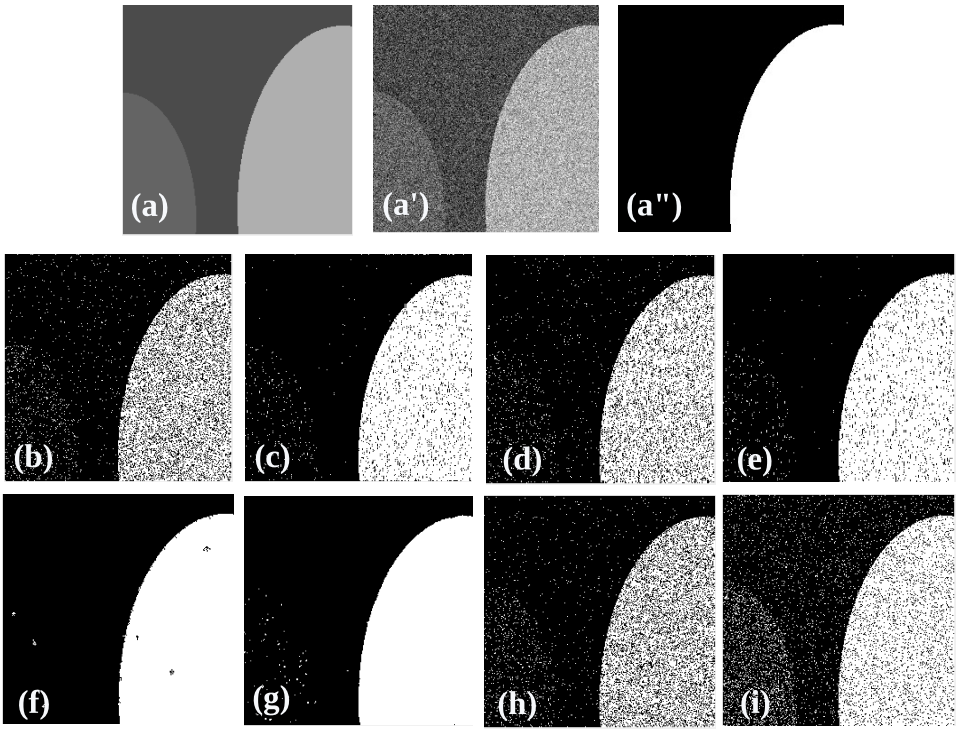

Figure 3.2: Comparison of segmentation results on the synthetic image. (a) Original image. (a') Noisy image (Gaussian noise with zero mean and 2% variance). (a") Ground truth. (b) FCM result. (c) EnFCM result. (d) SFCM result. (e) FGFCM result. (f) FRFCM result. (g) DSFCM_N result. (h) FCM_SICM result. (i) SSFCA result.

Table 3.3: The metrics values achieved by different algorithms on the synthetic images corrupted by various ratios of Salt & Pepper noise.

Salt & Pepper noise						
Ratio	Algorithms	Pr	Sp	Sn	F_1	Acc
3%	FCM	0.9753	0.9850	0.9851	0.9850	0.9802
	EnFCM	0.9673	0.9803	0.9673	0.9754	0.9673
	SFCM	0.9886	0.9931	0.9933	0.9932	0.9910
	FGFCM	0.9688	0.9812	0.9669	0.9759	0.9679
	FRFCM	**0.9996**	**0.9997**	**0.9998**	**0.9998**	**0.9997**
	DSFCM_N	**0.9985**	**0.9991**	**0.9829**	**0.9930**	**0.9907**
	FCM_SICM	0.9754	0.9850	0.9841	0.9847	0.9797
	SSFCA	0.9744	0.9844	0.9851	0.9847	0.9797
6%	FCM	0.9519	0.9704	0.9704	0.9704	0.9611
	EnFCM	0.9409	0.9644	0.9408	0.9555	0.9409
	SFCM	0.9886	0.9931	0.9933	0.9932	0.9910
	FGFCM	0.9394	0.9636	0.9357	0.9531	0.9375
	FRFCM	**0.9996**	**0.9998**	**0.9997**	**0.9997**	**0.9996**
	DSFCM_N	**0.9944**	**0.9967**	**0.9692**	**0.9864**	**0.9816**
	FCM_SICM	0.9514	0.9702	0.9697	0.9700	0.9605
	SSFCA	0.9517	0.9704	0.9701	0.9703	0.9608

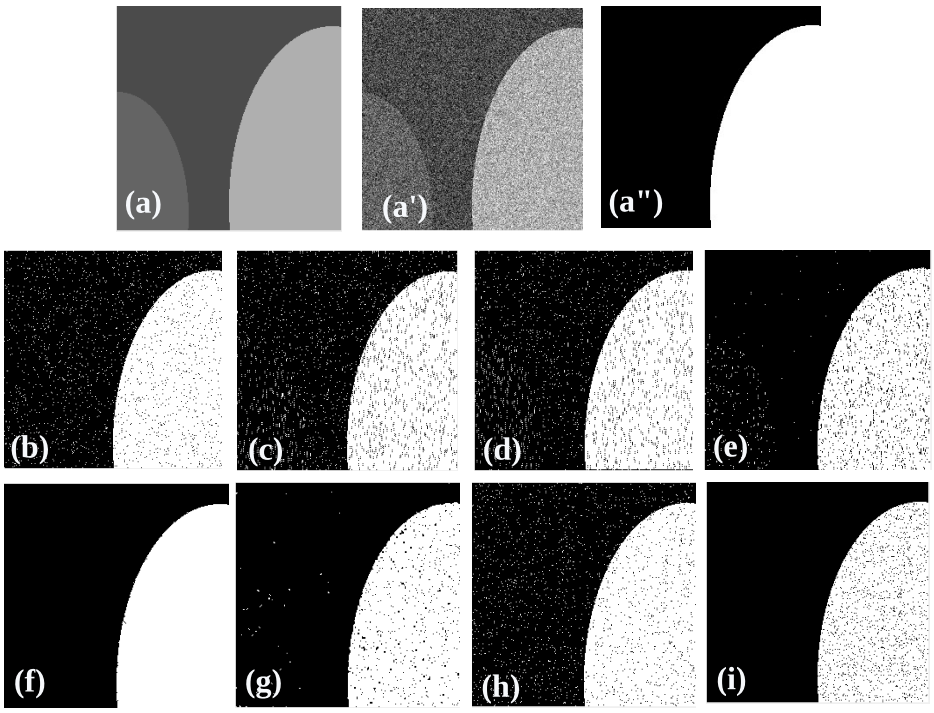

Figure 3.3: Comparison of segmentation results on the synthetic image. (a) Original image. (a') Noisy image (Salt & Pepper, the noise intensity is 6%). (a") Ground truth.(b) FCM result. (c) EnFCM result. (d) SFCM result. (e) FGFCM result. (f) FRFCM result. (g) DSFCM_N result. (h) FCM_SICM result. (i) SSFCA result.

tested, including FCM, EnFCM, SFCM, FGFCM, FRFCM, DSFCM_N, FCM_SICM, and SSFCA. Note that FCM_SICM and SSFCA were also tested.

The flowchart of the retinal image segmentation process using the improved FCM algorithms is depicted in Figure 3.4. It comprises five stages: retinal image acquisition from the database, extraction of the green channel, image enhancement, image segmentation, and separation of the vascular structure.

3.4.1.1 Pre-processing phase

Various techniques and Algorithms are employed in the pre-processing stage prior to the segmentation of retinal images in order to enhance their quality and make them more suitable for segmentation. The pre-processing stage includes extracting the green channel from the original image as part of the image enhancement process. This is followed by two techniques, namely, CLAHE (Contrast Limited Adaptive Histogram Equalization) subsection 2.5.1 and the bottom-hat filter subsection 2.5.3 , respectively, to improve the final segmentation outcome. The filter settings are chosen after many experiments, and at the end, the value 11 is chosen for the structural element with the square shape, for it gives satisfactory results. These techniques enhance the image and make it more appropriate for accurate and effective segmentation.

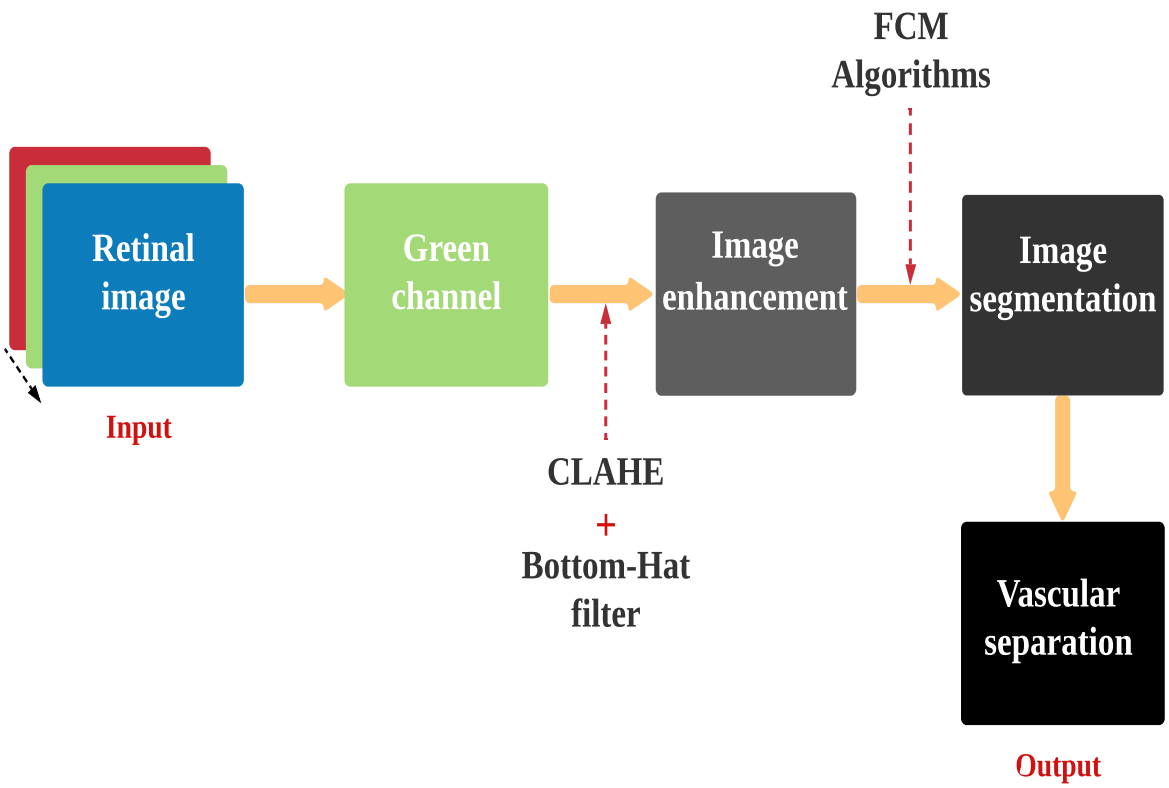

Figure 3.4: Flowchart of the retinal image segmentation phases.

3.4.1.2 Segmentation phase

The segmentation phase involves using improved FCM algorithms to categorize retinal images into three distinct groups: background, retinal vessels, and other tissues. The retinal vessels, known as the region of interest, are given particular attention. The performance of each improved FCM algorithm is measured by its capability to accurately separate the pixels belonging to the retinal vessels from those in the background. The accuracy of segmentation between the vessels and background is essential to determining these algorithms' effectiveness.

In order to highlight the interest in the retinal image pre-processing phases before the segmentation process, we conducted several experiments by employing the improved FCM algorithms. The main idea is to show retinal image segmentation results before and after each pre-processing step.

Figure 3.5(a-d) illustrates the results of this study. Some algorithms like FCM, En-FCM, SFCM, and FGFCM have poor segmentation result on the color images because they are designed to segment only the grayscale images.

The images in Figure 3.5(a) are the segmentation results performed on the three channels illustrated on one image. Moreover, the images Figure 3.5(a-c) demonstrate the inability of the improved FCM algorithms to segment retinal images and their need for pre-processing phases. The images in Figure 3.5(d) demonstrate that the

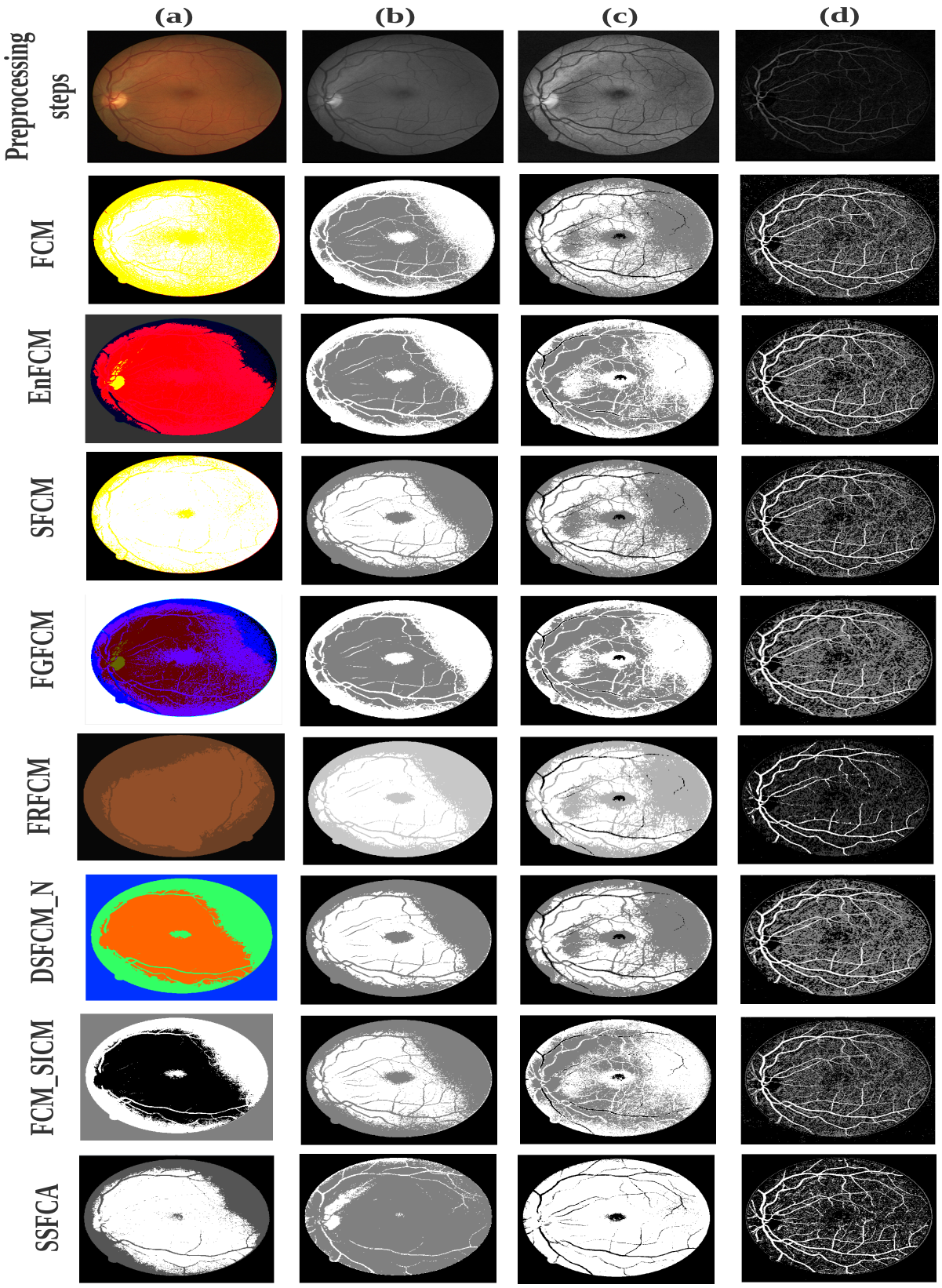

Figure 3.5: The algorithms results from different pre-processing on the retinal image. (a) Results of algorithms on the color image of the retina. (b) Results of algorithms on the green channel image of the retina. (c) Results of algorithms after CLAHE process. (d) Results of algorithms after bottom-hat filtering process.

proposed pre-processing operations (CLAHE and bottom-hat filter) have contributed to achieving the desired segmentation.

3.5 Results and Discussion

3.5.1 Image database

A comprehensive examination was performed on the STARE and DRIVE database in order to validate the improved version of the FCM algorithm. The details of the database can be found in the chapter entitled "Literature review: Retinal vessel segmentation" section 2.2.

3.5.2 Blood vessel extraction

As mentioned above, the experiments have been conducted on two well-known open-access databases, STARE and DRIVE. Hence, the results obtained on the STARE database are illustrated in Table 3.4. As indicated in this table, the FGFCM algorithm has the highest value in terms of the segmentation accuracy (Acc = 0.9517), which is a little higher compared with the FRFCM algorithm (Acc = 0.9511). Moreover, the highest F_1 score is reached by the FRFCM algorithm. However, the SFCM algorithm achieved the highest specificity value (Sp = 0.9911), and the best precision value is obtained by the EnFCM algorithm (Pr = 0.8831). Figure 3.6 depicts the comparison of the segmentation results on the STARE database.

However, the results obtained on the DRIVE database are illustrated in Table 3.5 and Figure 3.7. As shown in Table 3.5, the DSFCM_N algorithm has the highest values in terms of the segmentation accuracy (Acc = 0.9522) and F_1 score (F_1 = 0.3323). This latter is followed by the conventional FCM algorithm with an accuracy value of (Acc= 0.9504) and the FRFCM algorithm (Acc = 0.9499), while the highest specificity value is achieved by the SFCM algorithm (Sp = 0.9971), and the best sensitivity value is obtained by the SSFCA algorithm (Sn = 0.7289).

It should also be mentioned that the results of this performance analysis are fully compatible with those obtained in the section dealing with noise robustness analysis. In fact, the algorithms DSFCM_N, FRFCM, and FGFCM provide the best segmentation accuracy since these algorithms use several mathematical tools such as morphological reconstruction and membership filters to suppress noises and achieve a better visual effect and segmentation accuracy.

Broadly speaking, the performance in terms of segmentation accuracy of the improved FCM algorithms is close to each other, even though the objective functions are

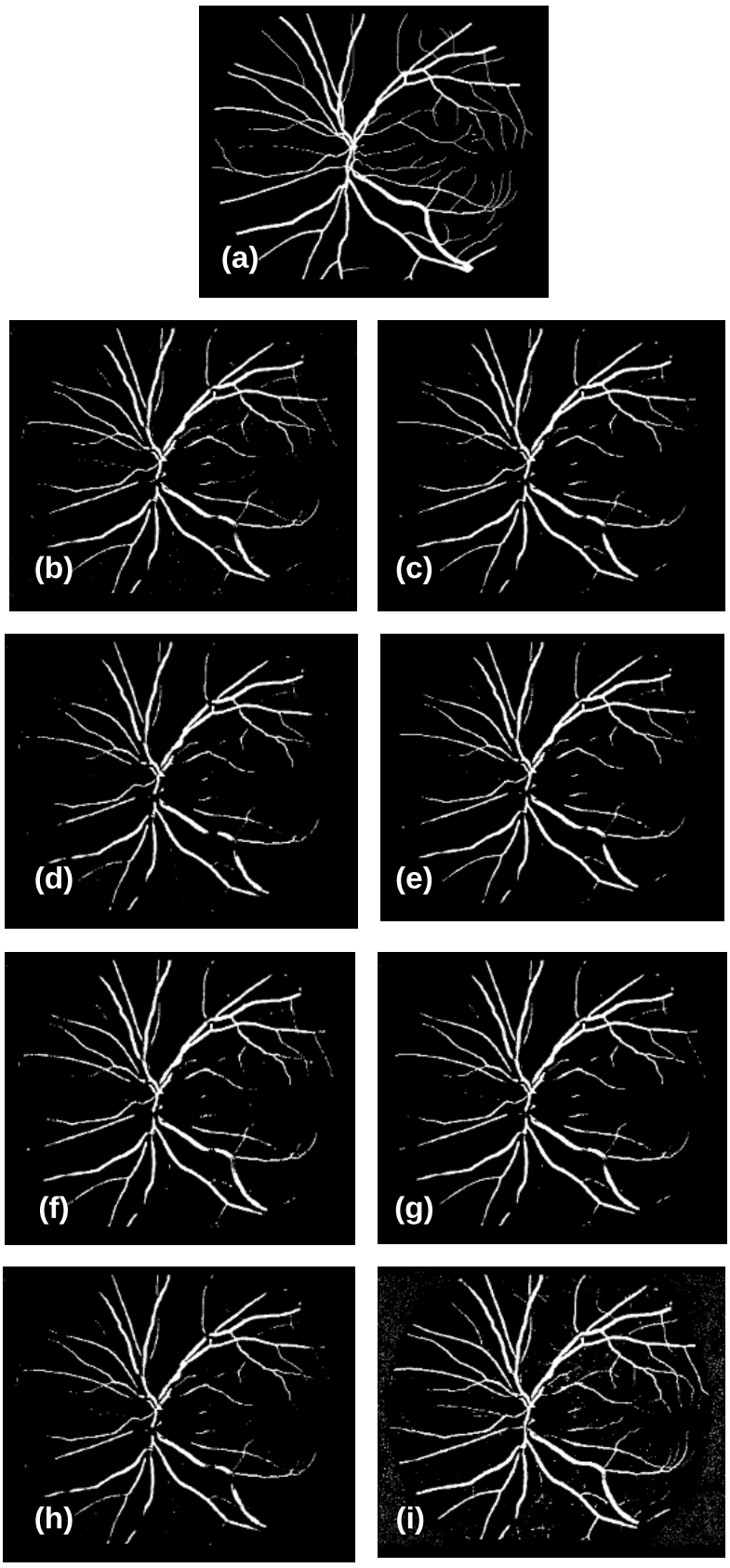

Figure 3.6: Comparison of segmentation results on STARE database. (a) Ground truth, (b) FCM result. (c) EnFCM result. (d) SFCM result. (e) FGFCM result. (f) FRFCM result. (g) DSFCM_N result. (h) FCM_SICM result. (i) SSFCA result.

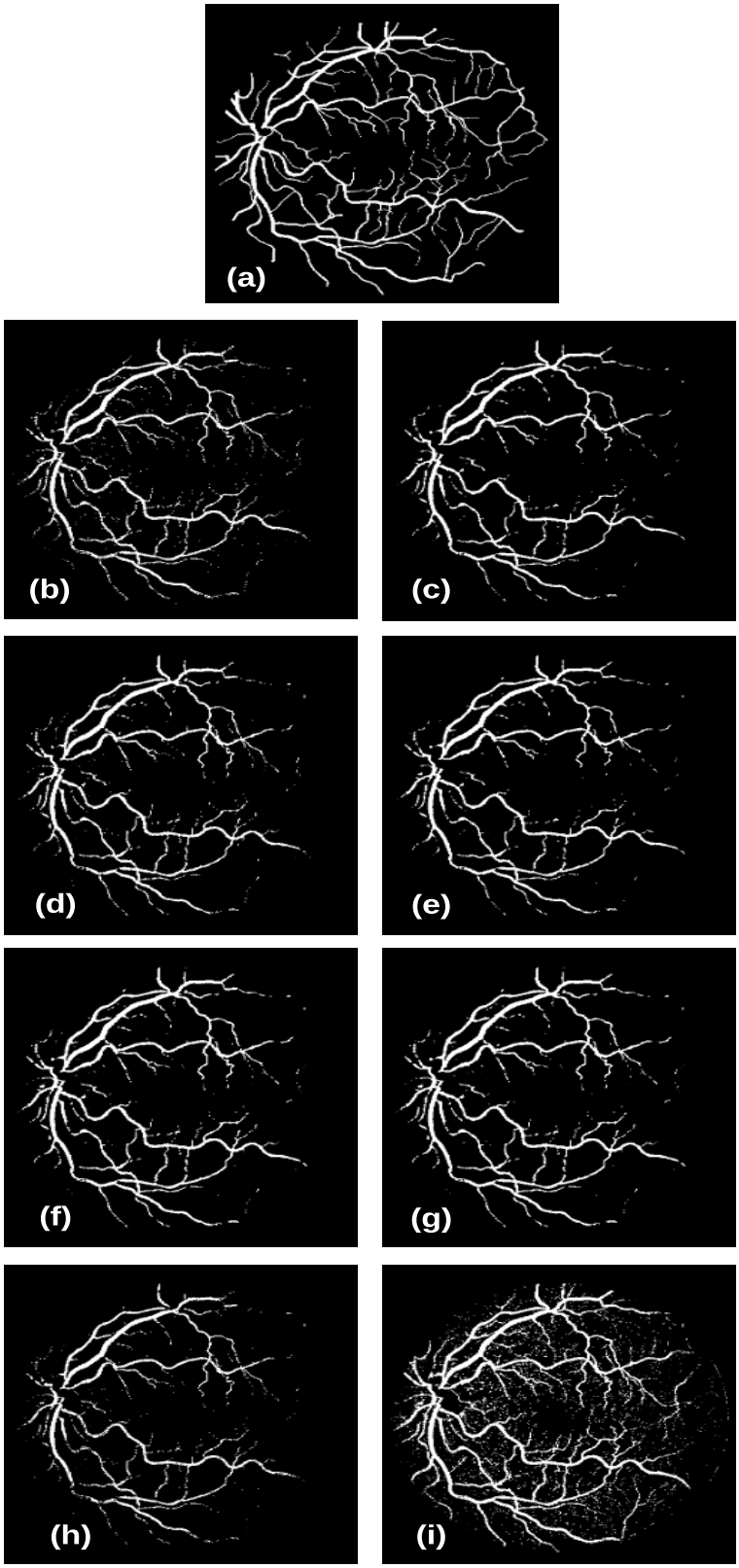

Figure 3.7: Comparison of segmentation results on DRIVE Database. (a) Ground truth, (b) FCM result. (c) EnFCM result. (d) SFCM result. (e) FGFCM result. (f) FRFCM result. (g) DSFCM_N result. (h) FCM_SICM result. (i) SSFCA result.

different. Consequently, we tend to say that there is a significant similarity between the improved FCM algorithms.

Table 3.4: Segmentation precision (Pr), sensitivity (Se), specificity (Sp), F_1 score, and accuracy (Acc) achieved by different algorithms on the STARE database.

STARE						
Algorithms	Pr	Sp	Sn	F_1	Acc	
FCM	0.7322	0.9788	0.5727	0.3214	0.9474	MATLAB
EnFCM	0.8831	0.9802	0.5654	0.3447	0.9482	
SFCM	0.8146	0.9911	0.4632	0.2952	0.9509	
FGFCM	0.7804	0.9854	0.5464	0.3214	**0.9517**	
FRFCM	0.7525	0.9815	0.5870	**0.4201**	**0.9511**	
DSFCM_N	0.7264	0.9742	0.6059	0.3303	0.9455	
FCM_SICM	0.7749	0.9847	0.5026	0.3048	0.9475	
SSFCA	0.4872	0.9194	0.7919	0.3016	0.9089	

Table 3.5: Segmentation precision (Pr), sensitivity (Se), specificity (Sp), F_1 score, and accuracy (Acc) achieved by different algorithms on the DRIVE database.

DRIVE						
Algorithms	Pr	Sp	Sn	F_1	Acc	
FCM	0.8913	0.9939	0.4944	0.3180	**0.9504**	MATLAB
EnFCM	0.8831	0.9935	0.4902	0.3152	0.9497	
SFCM	0.9331	0.9971	0.4012	0.2805	0.9453	
FGFCM	0.7748	0.9819	0.5979	**0.3374**	0.9492	
FRFCM	0.8803	0.9929	0.4996	0.3187	0.9499	
DSFCM_N	0.8762	0.9922	0.5354	**0.3323**	**0.9522**	
FCM_SICM	0.9231	0.9965	0.4165	0.2870	0.9460	
SSFCA	0.6516	0.9581	0.7289	0.3440	0.9377	

3.5.3 Running time

To evaluate the practicability of improved FCM algorithms, their execution times are compared in this subsection. All experiments are executed on a workstation with an Intel ® Core (TM) i5-2520. 2.5GHz CPU and 2G memory and by using MATLAB. The Table 3.7 and Table 3.6 show the running times of different algorithms measured on the STARE and DRIVE databases, respectively. The running time is the average value calculated by executing each algorithm five times on the databases.

As indicated in the tables, it is obvious that the SSFCA algorithm is the slower one (243,31 s on STARE and 165.73 s on DRIVE). Since the SSFCA integrates into the objective function the regularization under Gaussian metric to obtain fuzzy membership with sparsity. However, the running time of the algorithms SFCM, FGFCM,

Table 3.6: Comparison of execution times (in seconds) performed by different algorithms on STARE database.

Algorithms	FCM	EnFCM	SFCM	FGFCM	FRFCM	DSFCM_N
Average time	11,73	**7,29**	31,15	21,80	**0.40**	13,78
	FCM_SICM	SSFCA				
	14,05	243,31				

Table 3.7: Comparison of execution times (in seconds) performed by different algorithms on DRIVE database.

Algorithms	FCM	EnFCM	SFCM	FGFCM	FRFCM	DSFCM_N
Average time	8.15	**5.79**	22.03	17.29	**0.32**	10.96
	FCM_SICM	SSFCA				
	10.93	165.73				

DSFCM_N, FCM_SICM are very close to each other. They are around of 10 to 22 seconds. The best running times are achieved by the FRFCM and EnFCM algorithms. In fact, working on gray level, which is significantly less than the number of pixels in an image, makes EnFCM fast. As regard the FRFCM algorithm, its timeliness is due to the incorporation of the morphological reconstruction and membership filtering in the objective function.
Furthermore, the FRFCM algorithm employs the concept of the histogram. Therefore, the objective function of FRFCM converges rapidly. Given the previous experiments, we feel that the FRFCM algorithm, and to a lesser degree, the DSFCM_N algorithm, represent the best possible compromise in terms of the noise robustness, the retinal vessel segmentation effectiveness, and the time-consuming.

3.6 Conclusion

In this chapter, the performance of some improved FCM algorithms have been analyzed and compared in terms of the retinal vascular segmentation. Sereval derivatives of the FCM algorithm have been detained in this study: FCM, EnFCM, SFCM, FGFCM, FRFCM, DSFCM_N, FCM_SICM and SSFCA. The performance analysis have been conducted from three viewpoints: noise robustness, blood vessels segmentation performance, and time-consuming. The algorithms have been compared on the basis of several metrics like segmentation precision, sensitivity, specificity, F_1 score and accuracy. As a result, the FRFCM algorithm, and to a lesser degree the DSFCM_N algorithm, represent the best possible compromise between the three comparison criteria.

The experiments demonstrate that the FRFCM and DSFCM_N algorithms achieve

better results in terms of noise robustness and blood vessels segmentation. Regarding the running time, the FRFCM algorithm requires less time than other algorithms in the segmentation of retinal images.

Although the obtained results are satisfactory, retinal vessels segmentation based on the FCM algorithms could be further improved to achieve more accurate results. As a future scope, it will be interesting to focus on improving the pre-processing phase through the use of filters whose work is appropriate to the structure of the retinal vessels, such as Jerman filtering, morphological reconstructions, etc. Another avenue that could be explored is the use of the Field-of-View mask (FoV) to create an image without background pixels on the one hand, and to decrease the time-consuming by reducing the mathematical operations on the other hand. The next chapter presents the second contribution ,a high accuracy segmentation method for retinal blood vessel detection based on hybrid filters and an adaptive thresholding.

Chapter 4

An improved method for segmentation of retinal images based on hybrid filters and adaptive threshold

4.1 Introduction

Recently, different methods of segmenting retinal vessels have been proposed to improve their segmentation accuracy. This chapter presents a new unsupervised retinal vascular segmentation method that addresses challenges such as pseudo vascularization, difficulty detecting vessels, and enhancing low-resolution images. The proposed method utilizes a hybrid combination of well-known intensity transformations, filters, and an adaptive thresholding algorithm. The method involves applying CLAHE and BTH filtering to increase image contrast and Jerman filtering to bring up the vessel tree structure against a non-uniform image background. Reconstruction processes, BLH filtering, and a generated Field of View (FoV) mask are also used to remove noise and preserve image details. The proposed method is evaluated on the STARE and DRIVE databases. The chapter concludes with a discussion of the results and observations. The results of this study have been published in an international journal [127].

4.2 Methodology

The proposed methodology for retinal vessel segmentation involves a series of steps aimed at enhancing the quality of the image and increasing the visibility of vessels to achieve accurate segmentation, as outlined in the flow chart in Figure 4.1. The process comprises three phases: mask generation, pre-processing, and segmentation.

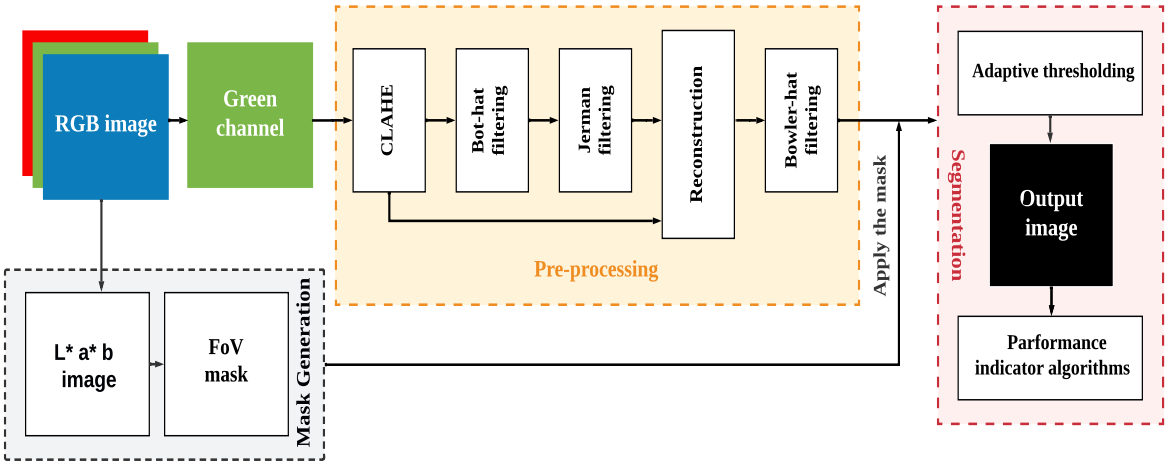

Figure 4.1: The flow chart of the proposed method for retinal image segmentation.

4.2.1 Mask generation phase

4.2.1.1 L*a*b image

The initial image has been captured using the RGB (Red, Green, Blue) color space. This color space is commonly used in image processing but is not always the best option for the task at hand. Converting an image from one color space to another can enhance the properties or characteristics of the objects in the image, making them easier to distinguish from their surroundings. In this study, we explore the process of converting an RGB image to the L*a*b color space. The L*a*b color space is based on the CIE XYZ tristimulus values, which consist of three components: a luminosity channel represented by L*and two chromaticity channels represented by a* and b*. The a* channel represents the green-red Channel, while the b* channel represents the blue-yellow Channel. These two channels contain all the color information that the image holds [96, 128]. The aim of converting the image to the L*a*b color space is to reduce the number of color dimensions, which in turn leads to a better separation between the intensity groups. This will allow us to create a mask for the original image, improving our image analysis results (see Figure 4.2) [129].

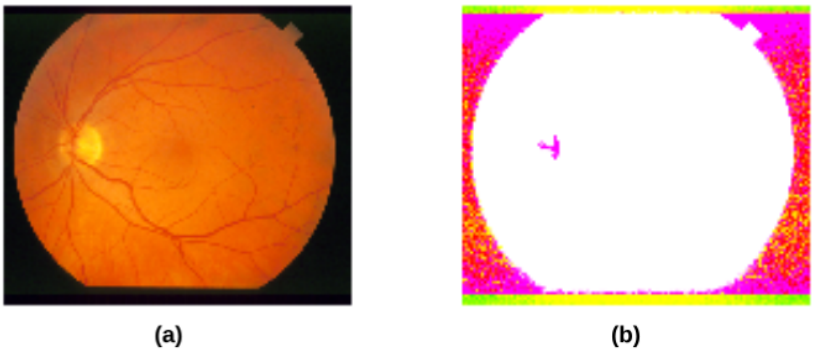

Figure 4.2: (a) Original Image and (b) converted L*a*b Image.

4.2.1.2 FoV mask process

Researchers often focus on the structures of interest and exclude the dark background from the analysis. To enhance efficiency and simplify mathematical operations, a mask image is typically generated as a binary image consisting of two values: zero (0) for the background and one (1) for the structures of interest.

In this study, the proposed method employs a Field-of-View (FoV) mask created by converting the RGB fundus image to the L*a*b color space, as mentioned above. The b chromaticity channel is then selected and converted into a binary image (0,1). Finally, a morphological erosion operation is performed using a disk-shaped structure element with a size of 6. This operation helps achieve the desired mask results by removing unwanted pixels in the image's background.

An illustration of the FoV mask generated using the proposed method is shown in Figure 4.3. This mask generation method has been tested and applied to both the STARE and DRIVE database.

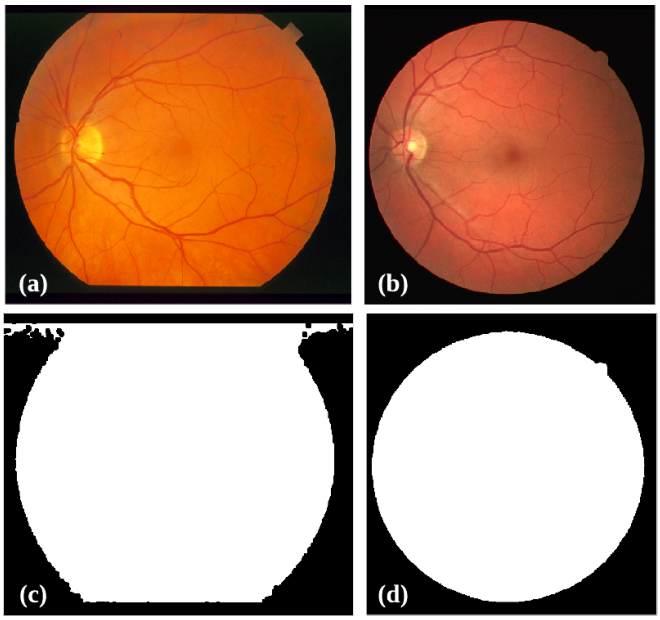

Figure 4.3: Mask generate. (a,b) RGB images of STARE and DRIVE databases, (c,d) FoV mask generated with our proposed method for the STARE and DRIVE databases, respectively.

4.2.2 Pre-processing phase

The first step of the pre-processing involves extracting the green channel of the RGB retina image with the highest contrast, followed by a series of enhancements applied to it.

4.2.2.1 Enhancement

Most of the time, using only the green channel is insufficient for a successful retinal image segmentation process. To improve the image quality, intensity transformations and filters are used. The CLAHE intensity transformation is used to clarify vessels and the background as outlined in subsection 2.5.1. Moreover, the low and varying contrast of retinal images poses a significant challenge for precise vessel segmentation in retinal image analysis. To overcome this challenge, it is necessary to enhance the quality of the retinal image by preserving details, improving poor contrast, and removing noise. This can be achieved through the application of a series of well-known filters, including BTH, BLH, and Jerman filtering. A complete explanation of the operation of each of these filters and their distinctive features that make them useful in the filtering process is provided in subsection 2.5.3.

4.2.2.2 Reconstruction

In image processing, reconstruction refers to the process of building or restoring an image from smaller parts or elements. Moreover, in morphological image processing, reconstruction is a technique for creating a new image from a given mask (I) and marker (h) image. The mask (I) image defines the desired properties for the final image, while the marker (h) image serves as the starting point for the reconstruction process. This process can be used to remove unwanted features, enhance objects, and count objects in an image, as the following equation:

$$Mr = I - h \tag{4.1}$$

Reconstruction is typically performed on binary or grayscale images and has a variety of applications in fields such as medical imaging, computer vision, and pattern recognition [121].

4.2.3 Segmentation phase

4.2.3.1 Adaptive thresholding

Thresholding is the process of converting a grayscale image into a binary image. There are two main types of thresholding techniques: global and local adaptive thresholding. Global thresholding has its limitations because images often have variable contrasts, imaging artifacts, and illumination changes, which makes it difficult to segment an image with a single global threshold. To overcome these limitations, local adaptive thresholding was developed. This technique uses different thresholds for each pixel location in the image, allowing for better segmentation of images with variable contrasts

and lighting conditions. The local threshold value in adaptive thresholding can be based on various statistics, such as the mean, which is calculated as:

$$T = \text{mean} + C \tag{4.2}$$

Where (T) is the threshold of the local neighborhood of $(W \times W)$ pixels surrounding each pixel. The choice of W is critical. It must be large enough to cover enough background and foreground pixels at each point. However, it should not be so large that it affects the threshold, and (C) sets the threshold above the general image noise variance in uniform pixel areas [130].

Several attempts have been made to improve traditional thresholding techniques. One example is the method proposed in [131], which is based on the Bradley algorithm and uses fuzzy integrals for the optimization of the thresholding process. However, this method is time-consuming and requires tuning of parameters to achieve optimal results. After conducting experiments specifically on retinal images Appendix B, we decided to use traditional adaptive thresholding due to its simplicity and effectiveness in segmenting thick and thin blood vessels in retinal images, especially after thorough pre-processing.

4.2.4 Combination phases

In the first step of our image processing phases, we create a FoV mask by converting the color image to the L*a*b color space (explained in detail in subsection Figure 4.3). The resulting mask is used in the penultimate stage before the vessels' segmentation and extraction, reducing calculation complexity and increasing segmentation accuracy. Without the FoV mask, the accuracy rate is low.

Next, in the second step, we extract the green channel of the RGB retina image, which has higher contrast than the other channels. However, we find that the green channel alone is insufficient for successful clustering.

To further enhance the image and improve the assembly performance, we apply some intensity transformations and enhancement filters. In the third step, we apply the CLAHE intensity transformation (as shown in Figure 4.4(d)), which helps improve image contrast while preserving image components.

In the fourth step, we apply the BTH and Jerman filtering to highlight the blood vessels and make them more visible, as well as to define the edges and curves well. The BTH filter helps to avoid the protrusion of the lens of the eye, while the Jerman filtering makes both thin and large blood vessels stand out. We show the results of these filters in Figure 4.4(e) and Figure 4.4(f), respectively.

In the fifth step, we reconstruct the image (using Figure 4.4(d) and Figure 4.4(f)) to preserve its objects, and apply the BLH filtering as a final tool before performing the

segmentation (as shown in Figure 4.4(h)). This filtering eliminates noise significantly. After that, we apply the generated FoV mask.

- It should be noted that in the image reconstruction step, the image size and shape change, so it is important to apply the mask to the resulting image after this step to ensure that only regions of interest are included in the segmentation.

Finally, in the last step, we apply adaptive thresholding for pixel classification and retinal vessel extraction (as illustrated in Figure 4.4(i)). This step completes the segmentation process and provides the final output. The steps are summarized in a table (Table 4.1). The table provides a concise and easy-to-read overview of the entire image processing phases.

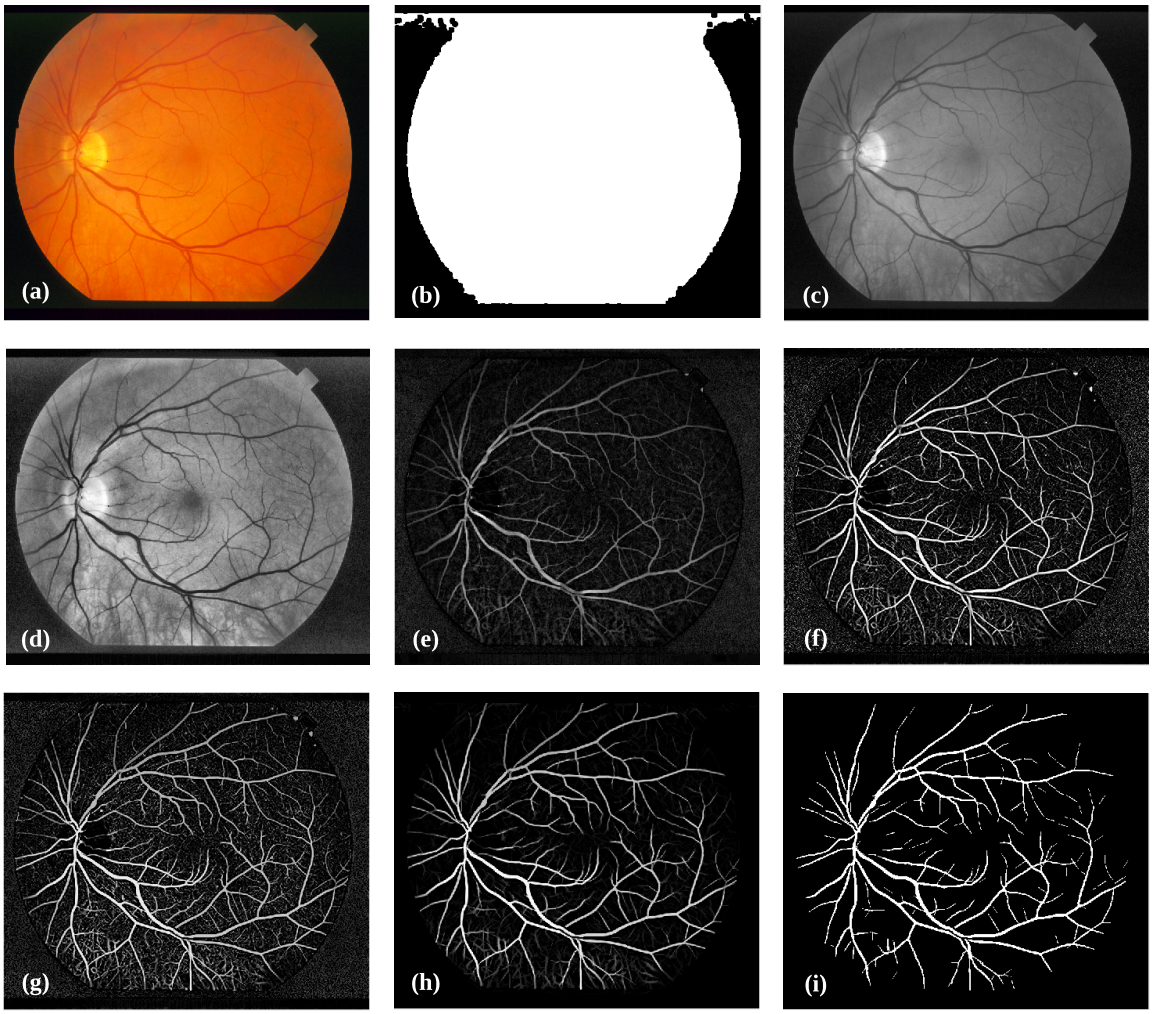

Figure 4.4: Sample image from the STARE database illustrating the various stages of our method. (a) Original image, (b) FoV mask, (c) green channel, (d) CLAHE, (e) image after bottom-hat filtering, (f) Jerman filtering, (g) image reconstruction, (h) image after bowler-hat filtering, and (i) image segmentation results.

Table 4.1: The main steps of the proposed method.

Proposed method
1. Generate a mask based on the fundus images. 2. Extract the green channel. 3. Normalized image output and apply CLAHE. 4. Perform the BTH filtering and Jerman filtering on the resulting image. 5. Implement reconstruction on the image from step 3 with the image from step 4. 6. Use BLH filtering on the resulting image. 7. Apply the mask generated on the resulting image. 8. Segment the image using adaptive thresholding.

4.3 Experiments

4.3.1 Image database

As previously done in our contribution, we verified the method proposed in this study using the STARE and DRIVE database, which served as the tool to validate the efficacy of the proposed method.

4.3.2 Parameterization of the proposed method

The Table 4.2 comprises a comprehensive list of the different values employed in the proposed method. The experiments conducted to test the method were carried out on a workstation equipped with an Intel® Core (TM) i5-2520 processor with a clock speed of 2.5 GHz and 2G of memory. The computations were performed using MATLAB software.

Table 4.2: Parameters used in the proposed method.

Parameters	**Value**
CLAHE	Default parameters
Bottom-hat filtering (BTH)	Shape (square) SE (11)
Jerman filtering	Default parameters
Bowler-hat filtering (BLH)	Shape (default parameters)
	σ=15, θ= 10
Adaptive thresholding	W_{STARE}= 55 , W_{DRIVE}= 150 C_{STARE}= 0.05 , C_{DRIVE} = 0.01

4.3.3 Metrics

In our second contribution, we adopted the same metrics used in the first contribution. These metrics are crucial in evaluating the performance of the segmentation algorithm. The metrics used in the first contribution include Sensitivity (Sn), Specificity (SP), Accuracy (Acc), Precision (Pr), and F_1 score (see section 2.6). In order to have a more comprehensive analysis of the segmentation results, we added the Matthews Correlation Coefficient (MCC) metric to the list. The utilization of these metrics will provide us with a clear understanding of the performance of our segmentation algorithm.

4.4 Results and discussion

This section presents the results of the experimental evaluations of our proposed retinal vascular segmentation method. The experiments were conducted in MATLAB, and a detailed analysis of the results is provided. We evaluated our method on two well-known open-access databases, STARE and DRIVE, and compared the results with those obtained by some of the unsupervised methods in the literature. We used sensitivity (Sn), specificity (Sp), and accuracy (Acc) as the evaluation metrics for vascular segmentation, where higher values of these coefficients indicate better performance

In Table 4.3, we compare the performance of different methods for retinal vessel segmentation on the STARE database, including 16 works selected for this study [45, 56, 61, 62, 67, 68, 82–89, 91, 132]. Our proposed method achieves better specificity and accuracy values than most of the other methods, with (Sp = 0.9810) and (Acc = 0.9618), respectively. It's worth noting that [89] achieved a high sensitivity value (Sn = 0.8949), but at the cost of reduced accuracy (Acc = 0.9354). In comparison, our proposed method achieves a sensitivity index of (Sn = 0.7253), which is closer to the typical values reported in the literature.

In the context of the DRIVE database, we have compared the performance of our proposed method with related works methods [45, 56, 61, 62, 67, 68, 82–89, 91, 132], as shown in Table 4.4. Our method achieves the highest specificity (Sp = 0.9874) and accuracy (Acc = 0.9586) compared to the other works analyzed. However, it's worth noting that the sensitivity index achieved by our method (Sn = 0.6595) is relatively lower than the other approaches tested.

To assess the effectiveness of our proposed method, we evaluated it using additional metrics, namely, the Matthews Correlation Coefficient (MCC), Precision, and F_1 score as described in Table 4.5. The results show that our method achieves satisfactory MCC values of (MCC = 0.7211, MCC = 0.7193) on STARE and DRIVE databases, respectively, which is within the expected range since the MCC coefficient varies between -1

Table 4.3: Comparison with related works methods on the STARE database.

STARE					
	Year	Sn	Sp	Acc	Method
Fraz et al. [61]	2012	0.7311	0.9680	0.9442	
Fathi and Naghsh-Nilchi [87]	2013	0.8061	0.9717	0.9591	
Azzopardi et al. [45]	2015	0.7716	0.9701	0.9497	
Zhao et al. [67]	2015	0.7800	0.9780	0.9560	
Oliveira et al. [82]	2016	0.8254	-	0.9532	
Zhang et al. [83]	2016	0.7791	0.9758	0.9554	
Neto et al. [56]	2017	0.8344	0.9443	0.8894	
Zhao et al. [91]	2017	0.7890	0.9780	0.9560	
Khomri et al. [88]	2018	0.7371	0.9620	0.9400	Unsupervised
Soomro et al. [85]	2018	0.7840	0.9760	0.9510	methods
Khawaja et al. [132]	2019	0.7980	0.9732	0.9561	
Wang et al. [62]	2019	0.7654	0.9735	0.9502	
Shah et al. [89]	2019	**0.8949**	0.9390	0.9354	
Roy et al. [84]	2019	0.4317	0.9718	0.9488	
da Rocha et al. [86]	2020	0.7932	0.9664	0.9533	
Mahtab and Hossein [68]	2022	0.7336	0.9741	0.9430	
Proposed method	2022	0.7253	**0.9810**	**0.9618**	

Table 4.4: Comparison with related works methods on the DRIVE database.

DRIVE					
	Year	Sn	Sp	Acc	Method
Fraz et al. [61]	2012	0.7152	0.9759	0.9430	
Fathi and Naghsh-Nilchi [87]	2013	0.7768	0.9759	0.9581	
Azzopardi et al. [45]	2015	0.7655	0.9704	0.9442	
Zhao et al. [67]	2015	0.7420	0.9820	0.9540	
Oliveira et al. [82]	2016	**0.8644**	0.9464	0.7425	
Zhang et al. [83]	2016	0.7743	0.9725	0.9476	
Neto et al. [56]	2017	0.7806	0.9629	0.8718	
Zhao et al. [91]	2017	0.7820	0.9790	0.9570	
Khomri et al. [88]	2018	0.7390	0.9740	0.9450	Unsupervised
Soomro et al. [85]	2018	0.7450	0.9620	0.9480	methods
Khawaja et al. [132]	2019	0.8027	0.9733	0.9561	
Wang et al. [62]	2019	0.7287	0.9771	0.9443	
Shah et al. [89]	2019	0.7760	0.9724	0.9473	
Roy et al. [84]	2019	0.4392	0.9622	0.9295	
da Rocha et al. [86]	2020	0.8100	0.9593	0.9462	
Mahtab and Hossein [68]	2022	0.7831	0.9553	0.9372	
Proposed method	2022	0.6595	**0.9874**	**0.9586**	

and 1. In addition, the precision values of (Pr = 0.7625, Pr = 0.8381) and the F_1 scores of (F_1 = 0.7389, F_1 = 0.7315) achieved on the STARE and DRIVE databases are also in line with typical values reported in the field of medical image segmentation.

Table 4.5: The results obtained using other metrics on STARE and DRIVE databases.

Database	MCC	Pr	F_1
STARE	0.7211	0.7625	0.7389
DRIVE	0.7193	0.8381	0.7315

In general, the proposed method has achieved good results in terms of accuracy and specificity indexes in both databases, which confirms once again the reliability of the proposed method.

4.5 Conclusion

This chapter introduces a novel unsupervised method for vessel segmentation in medical images using hybrid filters, which addresses two main challenges: low and varying image contrast levels and noise. To enhance the visibility of the vessels, we utilized CLAHE and morphological filters, and for highlighting both wide and thin vessels, we employed the Jerman filtering technique.

To improve the efficiency of the vessel detection process, we created a mask to reduce the number of mathematical operations. Finally, we utilized adaptive thresholding to extract the vessel features and segment the image pixels into vessels and non-vessels.

We evaluated our proposed method on two established clinical databases, STARE and DRIVE, and found that it outperformed current methods, particularly in terms of detection accuracy. This is a significant improvement and a promising result for our proposed method, which demonstrates its potential for accurately detecting vessels in medical images.

Chapter 5

Contributions in brain images segmentation

5.1 Introduction

In recent years, significant advancements have been made in the development of segmentation algorithms for brain images. These advancements are driven by the increasing availability of high-resolution imaging modalities such as magnetic resonance imaging (MRI), coupled with the growing demand for automated and efficient image analysis techniques. The quest for improved segmentation methods has led to the exploration of diverse computational approaches, ranging from traditional thresholding techniques to sophisticated machine learning algorithms.

This chapter provides three brain image segmentation techniques: multi-Otsu thresholding and morphological reconstruction, fast K-means clustering, and an advanced clustering approach combining K-means with Darwinian Particle Swarm Optimization (DPSO) and morphological reconstruction. Each method is meticulously designed to address specific challenges encountered in brain image segmentation, such as tissue heterogeneity, noise variability, and computational complexity.

The first method employs multi-Otsu thresholding and morphological reconstruction for tumor detection, demonstrating efficiency in contrast-enhanced preprocessing and accurate segmentation of brain tissues [8]. The second method introduces a fast K-means clustering algorithm enhanced with histogram information, offering improved accuracy and reduced computational overhead compared to conventional K-means clustering [9]. The third method presents an innovative integration of DPSO with K-means clustering and morphological reconstruction, addressing issues like centroid initialization and noise sensitivity to achieve superior segmentation results [7].

Throughout the chapter, rigorous experimental validation is conducted to evaluate the performance of each segmentation method. Comparative analysis with existing algorithms further highlights the superiority of the proposed methods in terms of both accuracy and computational efficiency.

5.2 Automatic Brain Tumor Segmentation Using Multi-OTSU Thresholding and Morphological Reconstruction

Images segmentation aims to divide an image into several segments. They can be selected according to the composition of the region of interest, the types of tissues, and the functional zones [133]. In this contribution, we present a new segmentation method, based on the multi-thresholding method and morphological reconstruction for brain tumor separation from Magnetic Resonance Imaging (MRI). Firstly, we use a pre-processing to enhance image contrast and quality by intensity adjustment. Secondly, the improved image is segmented using the multi-Otsu method and finally, a morphological reconstruction was performed with the appropriate structuring element parameter on the segmented image to determine the tumor. A comparison with some state-of-the-art algorithms demonstrated the efficiency of the proposed method with regard to accuracy.

5.2.1 Proposed Methodology

In this section, we explain in detail the proposed method for segmenting a brain tumor in MRI. Firstly, we start by applying a pre-processing operation on the image that we want to segment. The objective of this step is to improve the contrast of the considered image by adjusting its intensity. After that, we apply a method based on multi-threshold represented by the multi-Otsu method. It segments the image into several clusters by determining the n-1 thresholds. Then, the morphological reconstruction process was applied to the segmented image. The purpose of the last step is to detect the tumor and isolate it from the rest of the brain tissues. Figure 5.1 is a clear explanation of the proposed method. Based on the above described, the proposed algorithm can be summarized as follows:

Algorithm 1: Proposed method

1. **Input:** Load Image MR.
2. **Initialize:** Number of thresholds (t=3) and structuring element (SE=9).
3. Apply an intensity adjustment on the loaded image.
4. **Multi-thresholding:** Segment the image into clusters using the multi-Otsu method.
5. **Morphological reconstruction operation:** Apply morphological closing reconstruction on the segmentation image.
6. **Output:** Tumor separation.
7. **Evaluation:** Performance indicators.

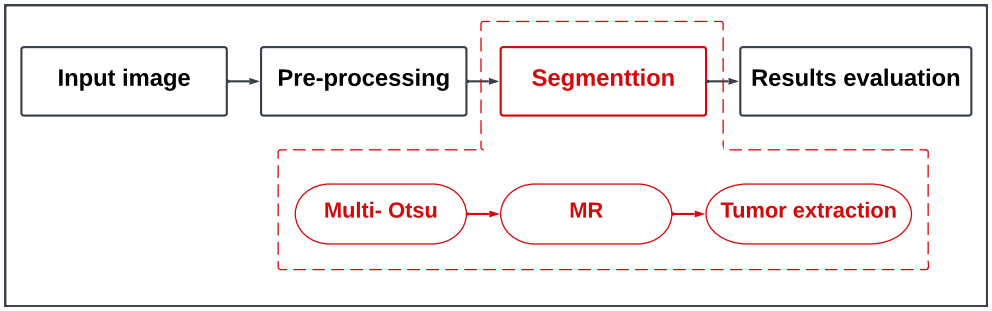

Figure 5.1: The framework of the proposed algorithm.

5.2.2 Experimental

5.2.2.1 Database

Brain tumors are usually classified according to their source or degree of aggression. Until, now the most used grading system presented by the World Health Organization (WHO), where brain tumors are classified from grade 1 to grade 4 with increased aggression. Among these tumors are WHO grade 4 gliomas, also known as glioblastoma multiform (GBM). These are the most common primary malignant brain tumors in humans, showing very rapid growth [133].

In this contribution, we use an improved T1-weighted MR image which is selected from a set of images acquired from patients with multiple glioblastoma (GBM). The segmentation of ground truth images has been performed by expert neurosurgeons [134].

5.2.2.2 Validation

In this subsection, a comparative study is performed to clarify and demonstrate the effectiveness of the proposed method for image segmentation of brain tumors. Indeed, the results of the proposed method will be compared to some state-of-the-art clustering algorithms such as multi-Otsu [135], K-means (KM), HKM [9], Fuzzy c-means (FCM),FRFCM and PSO [136]. For all methods, the number of segmented regions is four.

As regards the evaluation of medical image segmentation, we utilize some commonly-used metrics: sensitivity, specificity ,precision and Accuracy section 2.6.

The experimental results conducted on the database used a MATLAB (2020a) software and a computer with the following characteristics: an Intel Core i3-2328 MCPU@ 2.20 GHz processor and 1.89 RAM system. The results and images obtained from our experience of the proposed method and other methods have been shown in Table 5.1 and Figure 5.2 (The red arrow in the figures indicates the tumor region).

As regards the proposed method, we can observe in table 5.1 that the values of *Sp*, *Se* and *Pr* indicators are better than the values obtained using multi-Otsu, K-means

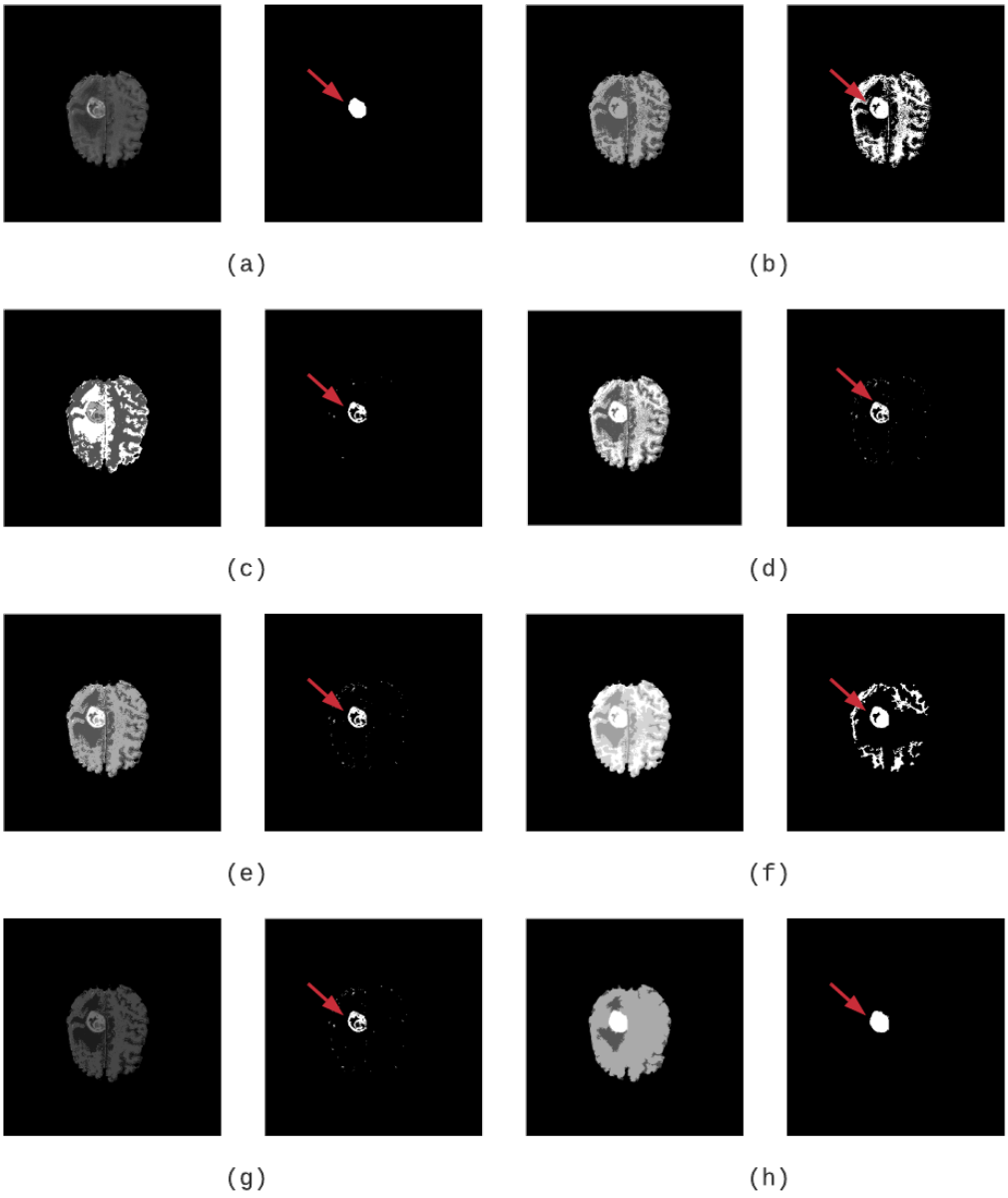

Figure 5.2: Segmentation results for different methods on the MR image (T1-weighted Axial slice, number 190). (a) Original image and ground truth. (b) Result of the multi-Otsu and tumor separation. (c) Result of the KM and tumor separation. (d) Result of the HKM and tumor separation. (e) Result of the FCM and tumor separation. (f) Result of the FRFCM and tumor separation. (g) Result of the PSO and tumor separation. (h) Result of the proposed method and tumor separation.

HKM, FCM, FRFCM, and PSO algorithms. While, the value of *Sp* obtained by HKM is slightly better than other values in the proposed method algorithm. Moreover, the value of *Se* and *Pr* is much better than other methods, as we seeing the value of *Se* is equal to 1, which means that the region of interest (tumor) is segmented almost correctly. Furthermore, accuracy indicator values demonstrate that the proposed method is more effective than other methods to isolate brain tumors in MR images.

Table 5.1: The performance results of multi-Otsu, KM , HKM, FCM, FRFCM, PSO and Proposed method,with *Sp*, *Se*, *Pr* and *Ac*.

Methods	*Sp*	*Se*	*Pr*	*Ac*
Multi-Otsu	0.9435	0.8922	0.0811	94.3180
KM	0.9987	0.6026	0.7286	99.6544
HKM	**0.9993**	0.6088	0.8259	99.7000
FCM	0.9985	0.6376	0.6985	99.6456
FRFCM	0.9783	0.8751	0.1837	97.7699
PSO	0.9987	0.6150	0.7226	99.6548
Proposed method	**0.9988**	**1.000**	**0.8302**	**99.8772**

5.2.3 Conclusion

Localization and discovery of the tumor are necessary to treat the tumor. Therefore, an effective method with certain characteristics such as robustness and accuracy is necessary to segment medical images. In this contribution, we used an image segmentation technique based on threshold and some morphological reconstruction operation to detect the brain tumor, contour, and calculate the tumor area. The performances of the proposed method were compared with the multi-Otsu, K-means, HKM, FCM, FRFCM, and PSO clustering algorithms using some indexes frequently utilized in the field of medical image segmentation. The results obtained clearly indicate the effectiveness of the proposed method, where the percentage of accuracy with the proposed approach is higher than in other methods.

5.3 A Fast K-means Clustering Algorithm for Separation of Brain Tissues in MR

Efficient separation of brain tissues in Magnetic Resonance Imaging (MRI) is a very important step for the quantitative diagnosis of brain diseases. To identify important brain regions such as the gray matter (GM), white matter (WM) and the cerebrospinal substance fluid spaces (CSF), we proposed in this contribution a new improved K-means algorithm (called HKM: Histogram-based K-Means) based on the image histogram and the median filter. The proposed algorithm is characterized by its ability to segment image faster and robustness in the presence of noise and non-uniform tissues. Moreover, it reduces the computational complexity and improves the performances of K-means algorithm in terms of the Jaccard and Dice Indexes. The obtained results demonstrate that the proposed HKM algorithm requires less times and achieves better results than the standard K-means clustering algorithm.

5.3.1 Proposed method

In this part, we show the contribution of this work. Differently from the computational procedure used in K-means algorithm, our idea consists in employing histogram information to initialize randomly the clustering centers and calculate Euclidean distance between the center and each pixel of an image. Histogram information is able to calculate distance in less time than classical method K- means. Distance between the center and the gray level of an image $I\,(x,\,y)$, can be written as:

$$D = \|i_l - Cn_k\| \tag{5.1}$$

where i_l are gray levels values of image $I\,(x,\,y)$.

Updating centers Cn_k again depends on gray levels values i_l and the number n_l of pixels in the image $I\,(x,\,y)$ with the intensity value i_l. It can be said that it is the same equation of the traditional K-means that was formulated by used the number of pixels in the image n_l and gray levels values i_l:

$$Cn_k = \frac{1}{n_l} \sum_{l \in Cn_k} i_l \times n_l \tag{5.2}$$

When we get the final centers through the equation above, we re-calculate the distance between the centers and all the values of the image as follows:

$$D_k^{'} = \|I(x,y) - Cn_k\| \tag{5.3}$$

where $D_k^{'}$ is the distance matrice which corresponds to the k^{th} cluster. Thus, we have k distance matrices.

Then, a median filter is used over the distance matrices to remove the different noises found in the image. The size of filtering window used is (3×3).

$$D_k^{''} = med[D_k^{'}] \tag{5.4}$$

Distance filtering has the ability to correct misclassified pixels. It is implemented only once on the final distance partition matrix.

The proposed algorithm HKM for medical image can be display as follows:

1. Image input normalization.
2. Set the prototype value k and the size of filtering window w.
3. Compute the histogram $H\,(i_l)$ of image $I\,(x,\,y)$ and initialize randomly the clustering centers Cn_k of the gray levels i_l.
4. Calculate the Euclidean distance between the centers and the gray levels of the image $I\,(x,\,y)$ using the equation (5.1).

5. The position of the new centers Cn_k updated by using the relationship (5.2).
6. Steps 4 and 5 are done until the center does not change.
7. Calculate the distance matrices D'_k using the equation (5.3).
8. Implement median filtering on distances matrices D'_k using the relationship (5.4).
9. Every pixels of the image is assigned to its nearest center based on distance matrices D''_k.
10. Reshape the pixels of each cluster into image.

5.3.2 Experiments

The performances of the proposed HKM algorithm in terms of the tissue segmentation of brain MR image are evaluated in this section. The phases of the tests using the proposed algorithm HKM are simplified in the figure Figure 5.3.

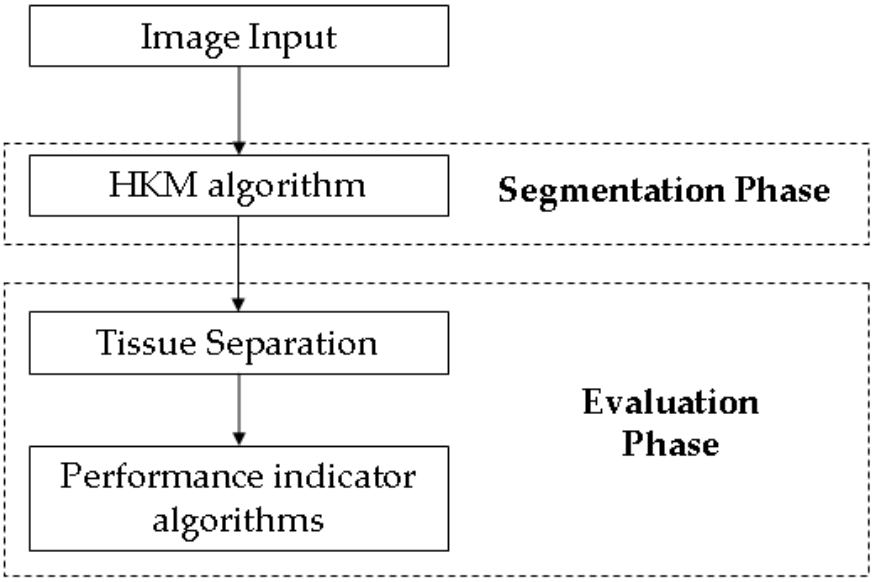

Figure 5.3: Phases of the segmentation using HKM.

Before performing the tests, some materials and mathematical tools are presented.

5.3.2.1 Image Base

The evaluation of our segmentation approach was performed on simulated MR images. We built by the simulator Brainweb, a ghost (T1) of size $181 \times 217 \times 181$, and the size of voxel $1 \times 1 \times 1$ mm^3. The volume is affected by Gaussian noise (7%). the images are accompanied by a ground truth which makes it possible to evaluate and compare the proposed approach [137]. Moreover, skull removing (structures that are not in the

interest) is a necessary steps to decrease the amount of memory used and to increase the speed of treatment and segmentation quality. Skull removing is done by using an automated cortical surface identification tool [138].

5.3.2.2 Data processing time

Experiments are performed on an Intel® Core™ i3-2328M CPU@ 2.20 GHz processor and 1.89 RAM system using MATLAB R2019a. The final data obtained is the average of the results after 30 times. Table 5.2 shows execution times of K-means and HKM algorithms obtained on tested image. According to the Table 5.2, we can see that

Table 5.2: The performance results of the K-means and HKM algorithms in terms of execution times.

Methods	KM	HKM
Running time [s]	2.9841 s	**0.6948** s

HKM requires less time than K-means algorithm. Furthermore, in percentage terms, the proposed approach reduces around of **76%** the computation time of the standard KM clustering algorithm. The reason behind the high performance of HKM is the use of histogram information instead of using the entire image .

5.3.2.3 Quality of tissues brain MRI segmentation

In this section, a comparison study is performed to illustrate the performance of the proposed HKM approach and to demonstrate its effectiveness. Indeed, the results of the proposed HKM algorithm will be compared to those obtained by K-means clustering algorithm and to the ground truth. The comparison is made for the three main brain substances which are: gray matter (MG), white matter (WM) and Cerebrospinal fluid (CSF). Figure Figure 5.4 shows segmentation results obtained by K-means and HKM. Looking at figure Figure 5.4, It should be noted that the proposed HKM algorithm is more robust than the standard K-means algorithm. Moreover, it may be mentioned that HKM algorithm removes all parasitic noises on brain tissues contrary to results obtained by K-means algorithm. In the sequel, Jaccard and Dice indexes are are used to evaluate the performance of K-means and HKM algorithms.

- Jaccard Index is defined as the overlap measurement between the segmented C image and ground truth D. It is expressed as [139]:

$$Jaccard = \frac{(C \cap D)}{(C \cup D)} \tag{5.5}$$

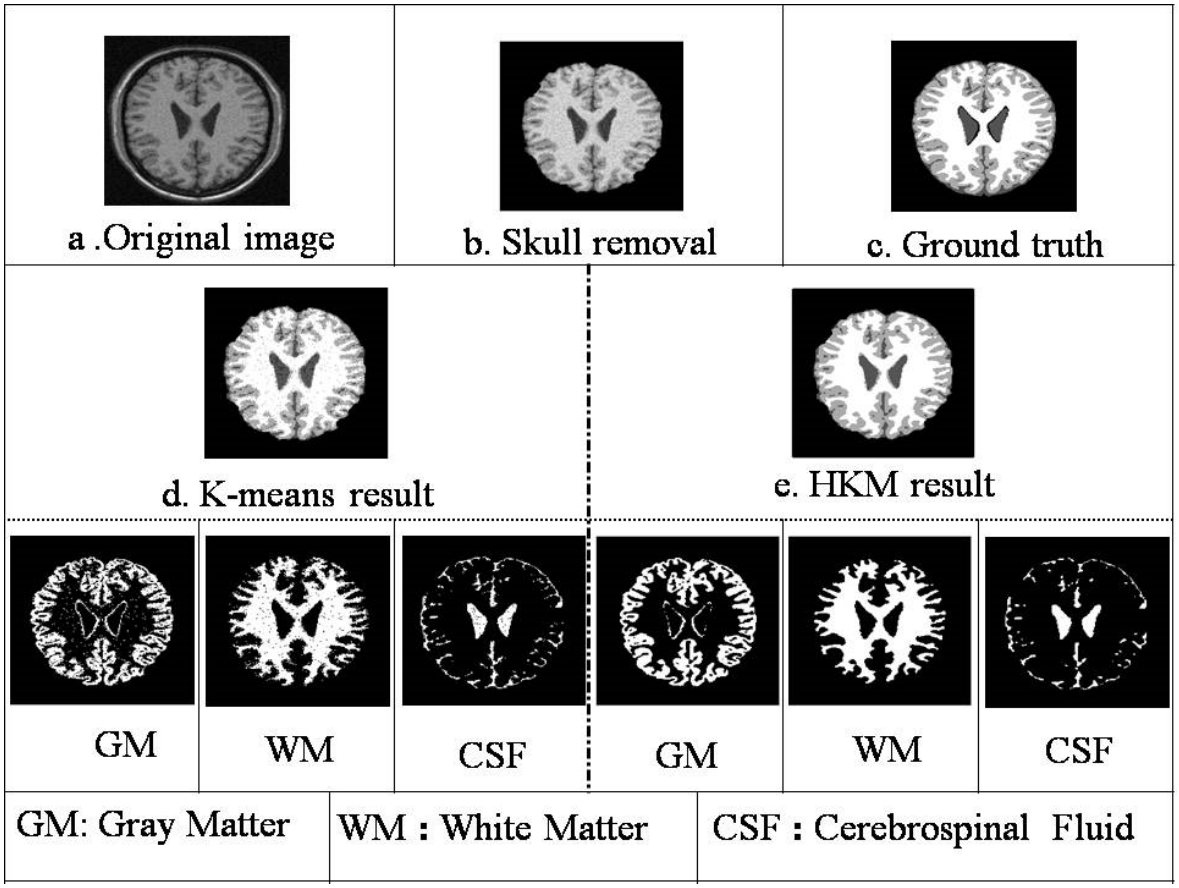

Figure 5.4: Illustration for the steps and results of the segmentation phase for K-means (KM) and HKM algorithms. Segmentation results done on a $T1$-weighted Axial slice (number 98) from SBD with 7% noise.

- Dice Index is the most used index in the validation of medical image segmentation. This one compares directly between the automatic segmentation C of images and truth of ground D, defined as:

$$Dice = \frac{2\,(C \cap D)}{(C) + (D)} \tag{5.6}$$

Indeed, the higher values of the Jaccard coefficients and Dice similarity can be interpreted as better performance.

Table 5.3: Comparison of Jaccard Index for K-means (KM) and HKM algorithms.

Jaccard Index		
Images	**KM**	**HKM**
GM	0.5894	**0.7863**
WM	0.9421	**0.9578**
CSF	**0.0842**	0.0596
Average %	53.85	**60.12**

Table 5.4: Comparison of Dice Index for K-means (KM) and HKM algorithms.

Dice Index		
Images	**KM**	**HKM**
GM	0.6978	**0.8804**
WM	0.9702	**0.9784**
CSF	**0.1553**	0.1125
Average %	60.77	**65.71**

Thus, the results of this study are summarized in the tables Table 5.3 and Table 5.4, which present the performances of K-means and HKM clustering algorithms. As regard the results presented in Table 5.3, we can observe that the values of the Jaccard indicator for the HKM algorithm are better concerning the separation of GM and WM tissues. However, K-means algorithm is a slightly better to separate the CSF tissue.

Moreover, Table 5.4 presents the values of the Dice index. Indeed, we clearly notice that the values obtained by the proposed algorithm are better than one obtained by using K-means algorithm for the separation of GM and WM tissues. However, for the CSF tissue, K-means algorithm is a bit better. The reason that the Jaccard and Dice indexes are better when using K-means for the case of CFS tissue is that the noise is considered as CSF tissue.

In general, the average values of Jaccard and Dice indexes mount us that the proposed HKM algorithm is more efficient than the K-means algorithm to the separation of brain tissues in MRI.

5.3.3 Conclusion

In this contribution, an improved K-means clustering algorithm for tissue segmentation of brain MR has been developed. The proposed approach permits to identify important brain regions such as the gray matter (GM), white matter (WM) and the cerebrospinal substance fluid spaces (CSF). Different performed tests validating the performances of the proposed scheme have been operated on simulated MR images. The performance of the proposed HKM algorithm was compared to K-means clustering algorithms using some indexes commonly used in the field of medical image. The results of the experiment confirm that the proposed HKM algorithm has a a computation time less than K-means algorithm and it gives better segmentation results for medical images.

5.4 An Improved Clustering Method Based on K-Means Algorithm for MR Brain Tumor Segmentation

The field of medical image segmentation is incredibly broad. Several works has been conducted on the study of such a field, especially Magnetic Resonance Imaging (MRI). This contribution aims to perform brain tumor segmentation on MR images using an improved clustering method based on K-Means (KM) algorithm. The proposed approach deals with some limitations of the standard KM algorithm such as, the random initialization of clusters centroids, and the noise sensitivity. The main idea consists to combine the Darwinian Particle Swarm Optimization (DPSO) technique, the KM algorithm and the Morphological Reconstruction (MR) operation. The DPSO technique is applied to the MR medical images for initialization of cluster centroids. Moreover, the MR filter is used to eliminate the noise and generate more compact and well separated clusters. The performance of the proposed method was evaluated by comparing it to some state of the art segmentation algorithms such as, standard KM clustering algorithm and DPSO-based multilevel thresholding [140]. The results show the effectiveness of the proposed method.

5.5 Proposed method

In this section, we describe the proposed method for brain tumor segmentation on MR images. This method is particularly useful in remedying some serious limitations of the KM clustering algorithm such as, the initialization of cluster centroids randomly and the imprecise determination of the tumor shape. The proposed approach consists in combining three types of algorithm such as, the DPSO algorithm, the KM clustering algorithm and the morphological reconstruction as a post processing to achieve a good detection of the tumor. Indeed, we chose MR operator and precisely reconstruction morphological closing because it allows the preservation of object contours and it is able to remove noise without knowing the noise type in advance [121].

Thus, the hybridization of these two methods (KM and MR) allows the extraction of the tumor area with high precision and less noise. The main steps of the proposed method are described as follows: firstly, the initial cluster centers are got by using DPSO algorithm. This step allows to obtain optimized values for the initial cluster centers. Then, the images are segmented using standard KM algorithm.

Afterwards, the MR is applied to the segmented image in order to separate correctly the tumor shape. The Figure 5.5 shows the schema illustrating the different phases of the proposed method.

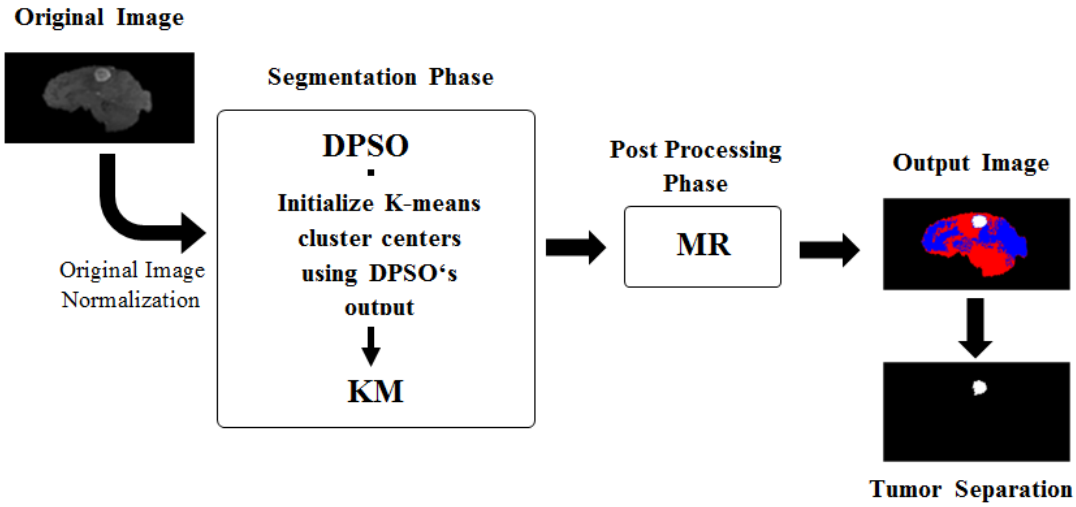

Figure 5.5: Different phases of the proposed method.

The pseudo-code of the proposed method algorithm is given as follows:

- Original image is normalized in the range [0 1].
- Adjust the parameters of the DPSO [140] (Table 5.5).
- Perform the DPSO algorithm.
- The results of DPSO algorithm are used as the initial cluster centers of KM algorithm.
- Run KM algorithm.
- Apply the MR operation on the image segmented by KM algorithm.

Noting that, a pseudo-color is added to output image in order to distinguish the regions more readily. Moreover, the performance of the MR operator depends on the selection of SE (a square with R=7), marker images and mask images.

5.5.1 Experimental validation

The performances of the proposed method approach in terms of the segmentation of brain tumors are evaluated in this section. Before performing such tests, some materials and mathematical tools are presented.

5.5.1.1 Database

The images operated in this section are T1-weighted MR images improved. They are obtained from patients with multiple glioblastoma (GBM). The segmentation of ground truth images has been performed by expert neurosurgeons. The datasets were

Table 5.5: Initial parameters of the DPSO.

Parameter	**Value**
R_1	0.8
R_2	0.8
$C1$ & $C2$	*Random*
W	1.2
V_{min}	-1.5
V_{max}	1.5
Current population of the swarm	30
Minimum number of swarms	2
Maximum number of swarms	6
Minimum population	10
Maximum population	50
Stagnancy	10
Number of iteration	100

skull-stripped and the segmentation is executed only at the enhancing tumor and the necrotic core [134].

5.5.1.2 Performance measure

Segmentation of medical image, which consists to extracting from the image one or more regions forming the area of interest, represents one of the essential image processing operations. Hence, the quality characterization of the segmentation method is very necessary task. In the field of medical image segmentation, there are several indices assessing the quality and reliability of the segmentation approach. Among these indices, one cited accuracy, sensitivity, precision, specificity section 2.6, Jaccard and Dice. where,

- True Positive (TP): tumor pixels detected correctly.
- False Positive (FP): healthy pixels detected as tumor pixels.
- False Negative (FN): Tumor pixels detected as healthy pixels.
- True Negative (TN): healthy pixels detected correctly.

5.5.1.3 Results and discussion

The purpose of this subsection is to report and discuss the results of the validation experiment. We present also the analysis of the obtained results.
The algorithms were implemented with MATLAB 9.6 (R2019a) on an Intel® Core™ i3-2328M CPU@ 2.20 GHz processor and 1.89 RAM system.

In order to assess the performance of the proposed segmentation method, we present a comparison study between our method and some state of the art segmentation algorithms such as, standard KM clustering algorithm and DPSO-based multilevel thresholding [141].

Thus, the results of this study are summarized in the Tables Table 5.6, Table 5.7 and Table 5.8, which present the performance results of KM, DPSO-based multilevel thresholding and proposed method algorithms for the number of classes equal to K=4. Moreover, the final data of each metric index are calculated on the basis of the average value of 50 running's.

Furthermore, the resultants output images of the proposed segmentation approach and the other methods are shown in Figure 5.6. Broadly speaking, we can notice that the proposed method allows a precise characterization of the tumor compared to the standard KM clustering and DPSO-based multilevel thresholding algorithms. These latter classed a part of the healthy tissue as a tumor which means they over estimate the size of the tumor. As shown in the Figure 5.6, these methods present a bad tumor localization.

Indeed, that could lead to serious problems related to lesion removal in cranial surgery or to over dose in radiotherapy.

Table 5.6: The performance results of KM, DPSO-based multilevel thresholding and Proposed Method result for K= 4 with Jaccard and Dice indexes.

Methods	JSC	DSC
KM	0.5185	0.6829
DPSO	0.5175	0.6819
Proposed Method	**0.8708**	**0.9309**

Table 5.7: The performance results of KM, DPSO-based multilevel thresholding and Proposed Method result for K= 4 with Specificity, Sensitivity ,Precision and Accuracy.

Methods	Specificity	Sensitivity	Precision	Accuracy
KM	0.9965	0.7345	0.6381	99.44
DPSO	0.9963	0.7493	0.6253	99.42
Proposed Method	**0.9992**	**0.9502**	**0.9123**	**99.88**

As shown in Table 5.6, the average values of Jaccard and Dice indicators for the proposed method are better than those of the standard KM clustering and DPSO-based multilevel thresholding algorithms. This means that our method presents the higher value of TP (see Table 5.8). Therefore, the tumor shape and its localization are well represented in the resulted segmentation.

Table 5.8: TP, FP, FN and TN results of KM, DPSO-based multilevel thresholding and Proposed Method for K= 4.

Methods	TP	FP	FN	TN
KM	797	452	288	131583
DPSO	813	487	272	131548
Proposed Method	**1031**	**99**	**54**	**131936**

Moreover, the Table 5.7 presents the average values of the following indexes: Specificity, Sensitivity, Precision and Accuracy. We can notice that all the metrics, calculated for the proposed method, are betters. Indeed, Sensitivity and Precision values of the proposed method are particularly higher comparing to the others methods. This means that the proposed segmentation method decreases the values of FP and FN (see Table 5.8), which involves that the overlap between the ground truth and the resultant image has increased.

Hence, based on this comparison study, the improved segmentation method gives better results comparing to the KM algorithm and the PSO-based multilevel thresholding. Moreover, we can say that the proposed method is able to generate more compact and well separated clusters.

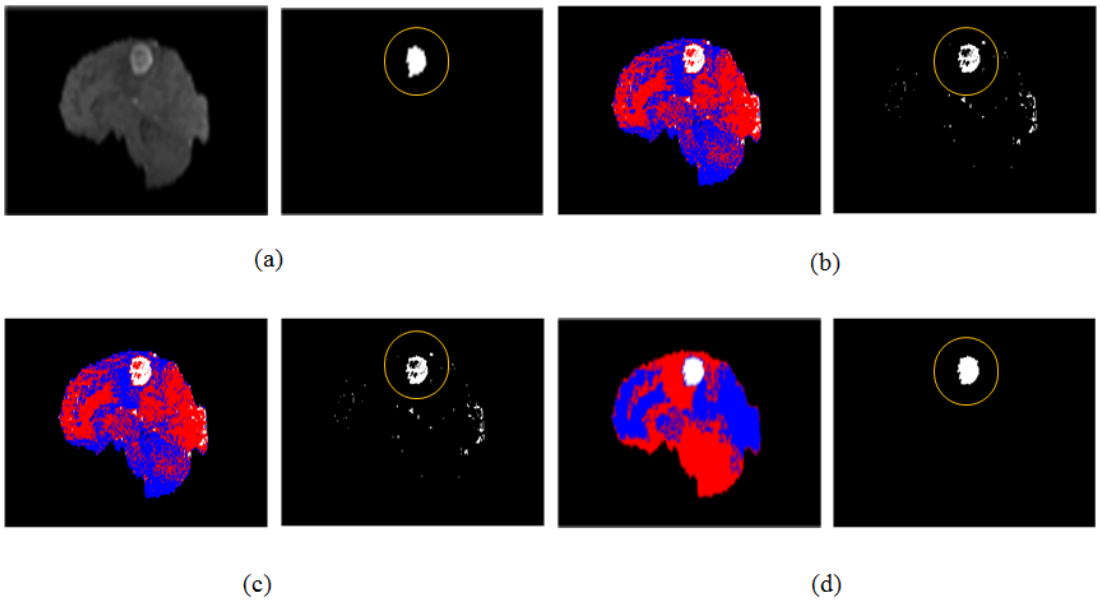

Figure 5.6: Comparison between different segmentation methods on MR image (T1-weighted Sagittal T slice, number 230). (a) Original image and ground truth. (b) Result of the KM and tumor separation. (c) Result of the DPSO-based multilevel thresholding and tumor separation. (d) Result of the proposed method and tumor separation.

5.5.2 Conclusion

In this contribution, a new improved segmentation method based on K-means clustering algorithm and MR operator has been developed for MR brain tumor segmentation. The DPSO algorithm was used as a pre-processing step to determine better centers for initialization of the KM clustering algorithm. However, MR is applied as a post-processing step to separate the brain tumor. Different performed tests validating the performances of the proposed scheme have been operated on T1-weighted MR images improved. The performance of the proposed method algorithm was compared to those of KM clustering algorithm and DPSO-based multilevel thresholding by using some indexes that commonly used in the field of medical image. Hence, the obtained results with different tests demonstrate that the proposed scheme guarantees the best performances in terms of sensitivity, specificity ,Precision and accuracy of the segmentation operation. Moreover, the proposed method approach is more efficient than other methods and it is very effective.

Chapter 6

Conclusion and Future Outlook

Conclusions

This dissertation covers the anatomy and functioning of the human eye and medical techniques. It emphasizes the importance of accurate diagnosis and monitoring through identifying landmarks in fundus photography and discusses the challenges of automated retinal blood vessel segmentation. The literature review evaluates different segmentation methods, databases, and metrics for vessel segmentation, paving the way for future advancements in the field. In this dissertation, we investigated various methods for segmenting blood vessels in the retina. Following a review of existing research, we presented two approaches. The main focus of this study was to address the following questions:

- How effective are some improved FCM algorithms for segmenting retinal blood vessels?
- What is the accuracy of the proposed methods for separating blood vessels from fundus images?
- Do the proposed automated blood vessel extraction methods outperform current methods?

There are different blood vessel segmentation algorithms available. However, to test and evaluate the algorithms, fundus images are needed. Thus, the publicly available image databases STARE and DRIVE play an essential role in evaluating and measuring the performance of algorithms. In addition, these databases include the corresponding ground truth images. Thanks to its availability to the general public, studying and estimating the performance of vessel segmentation algorithms has become easy.

The first contribution analyzed and compared the performance of some improved FCM algorithms in terms of retinal vascular segmentation. This study focused on eight FCM algorithm derivatives: FCM, EnFCM, SFCM, FGFCM, FRFCM, DSFCM_N, FCM_SICM, and SSFCA. The performance evaluation was carried out from three perspectives: noise robustness, blood vessel segmentation performance, and time-consuming.

The algorithms were compared using metrics such as segmentation precision, sensitivity, specificity, F_1 score, and accuracy. As a result, the FRFCM and, to a lesser extent, the DSFCM_N algorithms represent the best possible compromise among the three comparison metrics.

The experiments show that the FRFCM and DSFCM_N algorithms outperform each other in terms of noise robustness and blood vessel segmentation. In terms of running time, the FRFCM algorithm is faster than other algorithms for segmenting retinal images.

The second contribution is a new unsupervised method that uses hybrid filters before the vessel segmentation step to improve low and varying contrast on the one hand and reduce noise surges in devices on the other. As a result, CLAHE and morphological filters have been used to reduce low-frequency noise and improve vessel performance. Furthermore, Jerman filtering has been used to depict wide and thin vessels in images. Furthermore, the created mask was used to reduce mathematical operations and increase the effectiveness of segmentation. Finally, adaptive thresholding was used to extract vessel features as well as segment image pixels into the vessel and non-vessel images. These steps significantly improve the effectiveness of vessel detection capabilities. The proposed method has been validated using the established clinical databases STARE and DRIVE. It significantly outperforms the most recent methods, particularly in detection accuracy.

Beyond the main contributions of this dissertation, we have made advancements in the segmentation of MR brain images for tumor and tissue identification. Our techniques have been evaluated using diverse databases and have shown promising results in accurately detecting brain tumors and different types of tissues with high sensitivity and specificity. These supplementary contributions have been outlined in a separate chapter. Overall, our research makes valuable contributions towards developing efficient and effective methods for medical image segmentation.

Future Outlook

The proposed work depends on the hybridization of the filters and the use of unsupervised methods to divide and identify blood vessels in the eye to increase the accuracy of the division and facilitate the task for experts.

Still, with the development in the field of deep learning and proving its effectiveness and ability to provide good results, as a future scope, we hope to expand our research by applying methods of deep learning to the image of the eye network, as well as attempts to divide and identify the various parts of the eye that the expert is interested in studying, not only the blood vessels [51, 52].

Furthermore, it will also be interesting to extend the results of our research to

detect other ocular structures such as the optic disc, fovea and macula. Additionally, predicting various retinal diseases such as glaucoma, diabetic retinopathy, age-related macular degeneration, and others could be achieved by recording historical context data to perform retinal blood vessel segmentation for disease prediction. This is a promising avenue of research that could potentially improve the early detection and treatment of these diseases [142–144].

Appendices

Appendix A

Retinal Image Segmentation Using Clustering Methods: Performance Analysis

Clustering is a popular method for segmenting retinal images due to its efficacy and good performance. This paper analyzes the performance of some clustering algorithms for retinal image segmentation in terms of their ability to segment and isolate blood vessels. The flowchart of this study consists of two phases. The pre-processing phase aims to increase the contrast and clarity of the image by applying a series of operations: Contrast Limited Adaptive Histogram Equalization (CLAHE), median filtering, and bottom-hat filtering. Furthermore, the second phase deals with the segmentation of the preprocessed image using one of the clustering algorithms selected for this study: k-means, k-medoids, Gaussian Mixture Model (GMMs) and fuzzy c-means. The experimental part is carried out on the DRIVE and STARE databases, and the performance measure of each algorithm is accomplished using sensitivity, specificity and accuracy performance metrics. The running times of different algorithms are compared. The obtained results are extensively discussed and some suggestions are proposed at the end of this paper.

A.1 Experimental

On images acquired from two public databases Table 2.1. The flowchart for the approach used to segment retinal vessels is presented in Figure A.1. The green channel G of the RGB retinal image is extracted in the first stage due to its higher contrast, and this channel is analyzed in the following steps. Despite its higher contrast rate, the G channel alone is insufficient for successful clustering, as evidenced by the analyses. As a result, the retinal image was subjected to three additional pre-processing steps. The CLAHE is the initial phase, followed by median filtering, and finally bottom-hat filtering. The k-means, k-medoids, GMMs, and fuzzy c-means clustering methods are

used to segment retinal images produced after the pre-processing step (see Figure A.2 and Figure A.3). Different clustering algorithms were employed to segment the retinal image into 2 clusters, which represent the background, and retinal vessels. Noting that the retinal vessels are the region of interest that we aim to achieve. All experiments are executed using MATLAB. We used to evaluate the effectiveness of the algorithms sensitivity, precision and specificity, accuracy section 2.6.

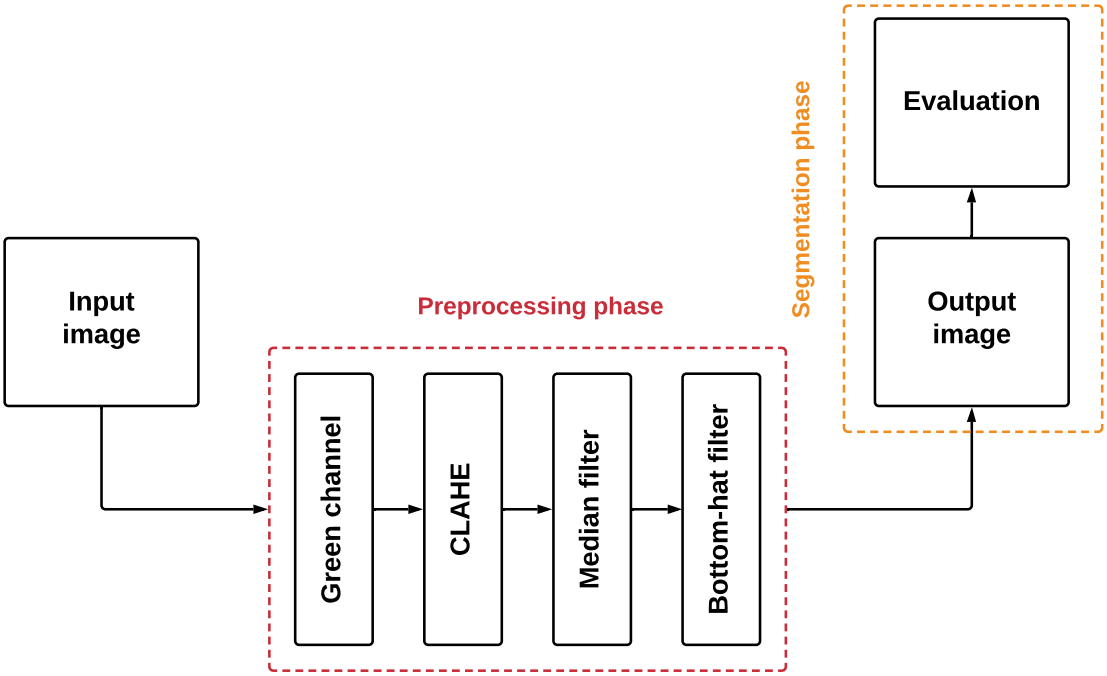

Figure A.1: Flowchart of the retinal image segmentation phases.

A.1.1 Results and Discussion

The performance of the k-means, k-medoids, GMMs, and fuzzy c-means algorithms in metrics of specificity, sensitivity, and accuracy section 2.6 for retinal images from the DRIVE and STARE databases section 2.2.

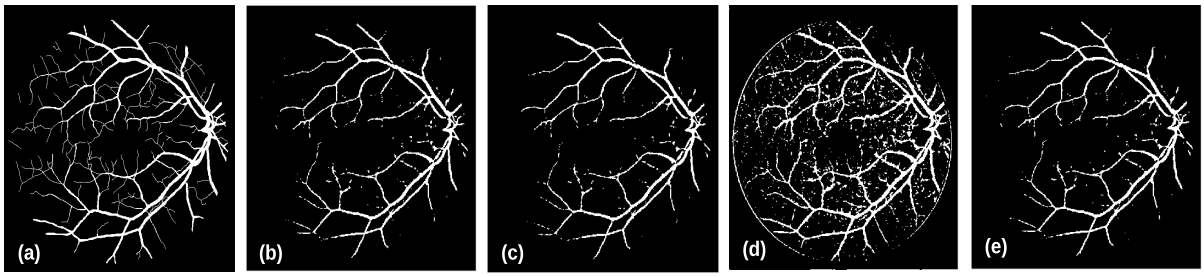

Figure A.2: Comparison of segmentation results on DRIVE Database. (a) ground truth, (b) K-means result. (c) K-medoids result. (d) GMMs result. (e) Fuzzy c-means result.

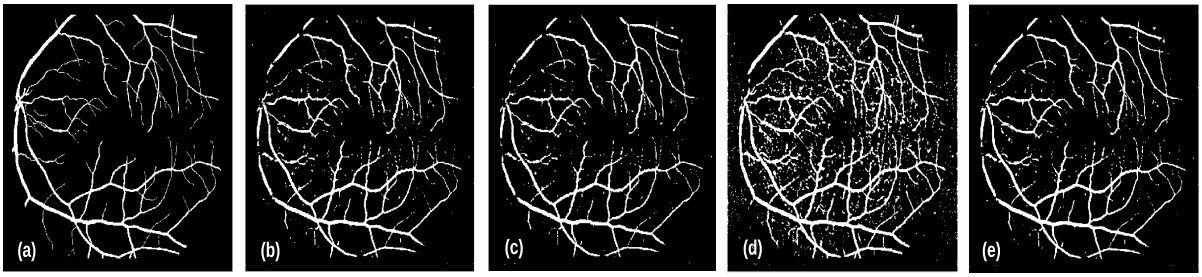

Figure A.3: Comparison of segmentation results on STARE Database. (a) ground truth, (b) K-means result. (c) K-medoids result. (d) GMMs result. (e) Fuzzy c-means result.

Table A.1: The performance of clustering algorithms on the drive database.

Metrics	**DRIVE**			
	K-means	K-medoids	GMMs	Fuzzy c-means
Sp	**0.9845**	0.9668	0.9127	**0.9837**
Sn	0.6112	0.5906	**0.8379**	0.6349
Acc	0.9534	**0.9563**	0.9054	0.9531

It can be observed from Figure A.2 and Figure A.3, that the specificity (Sp) results of each algorithm is capable of distinguishing between the vessel and background pixels and the sensitivity (Sn) results indicate that each method can achieve good performance in terms of the ratio of correctly classified vessel pixels. Furthermore, when the accuracy (Acc) the results demonstrated that each algorithm has a high ratio of correctly classified vessels and background pixels . In terms of values, the performance of the k-means algorithm in the specificity (Sp) metric appears to be better compared to GMMs and k-medoids algorithms. While, with fuzzy c-means algorithm the difference appears to be small. Whereas, the value of k-means ($Sp = 0.9845$) and the value of fuzzy c-means ($Sp = 0.9837$) on the DRIVE database and on the STARE database, the value of k-means ($Sp = 0.9703$), and the value of fuzzy c-means ($Sp = 0.9684$). While, the GMMs algorithm appears to do significantly better than that of the other algorithms in metric of sensitivity on DRIVE and STARE databases with the values ($Sn = 0.8379$) and ($Sn = 0.8760$), respectively. Moreover, the k-medoids algorithm showed the best results in metric of accuracy ($Acc = 0.9563$) while the fuzzy c-means algorithm showed the best performance with the STARE database with the value ($Acc = 0.9506$) . In general, it can be seen that the clustering performance of the selected algorithms is

Table A.2: The performance of clustering algorithms on the stare database.

Metrics	**STARE**			
	K-means	K-medoids	GMMs	Fuzzy c-means
Sp	**0.9703**	0.9605	0.9108	**0.9684**
Sn	0.6813	0.7166	**0.8760**	0.7307
Acc	0.9501	0.9482	0.9143	**0.9506**

Table A.3: Comparison of execution times of clustering algorithms on drive database

Algorithm	K-means	K- medoids	GMMs	Fuzzy c-means
Running time (s)	0.0617	1.1556	2.6991	0.6189

Table A.4: Comparison of execution times of clustering algorithms on stare database

Algorithm	K-means	K- medoids	GMMs	Fuzzy c-means
Running time (s)	0.1156	1.6641	3.1558	0.8729

successful and similar to each other and, that each of them is effective in one of the metrics used.

To assess the feasibility of the clustering algorithms, the running times of the selected algorithms were compared. Table A.3 and Table A.4 show running times of selected algorithms on DRIVER and STARE databases, respectively. The average value obtained was performed three (3) times for each algorithm. From Table A.3 and Table A.4, it is clear that k-means is very fast compared to other clustering algorithms.

Table A.5 shows the computational complexity of various algorithms based on the foregoing analysis, where N is the number of pixels in an image, K is the number of clustering prototypes, and t is the number of iterations, D is the problem dimension. According to Table A.5 k-means and fuzzy c-means have low computational complexity and GMMs have high computational complexity compared to other clustering algorithms.

Table A.5: Computational complexity of clustering algorithms

Algorithm	Computational complexity
K-means	$O(N \times K \times t)$
K-medoids	$O(N^2 \times K \times t)$
GMMs	$O(N \times K \times D^2 \times t)$
Fuzzy c-means	$O(N \times K \times t)$

A.2 Conclusion

In this study, The effectiveness and quality of various clustering algorithms for segmenting retinal images are compared. Different metrics such as specificity, sensitivity, and accuracy are used to evaluate the algorithms. According to experimental results, the k-means algorithm provides the best results on both the DRIVE and STARE databases in term of sensitivity. While, the gaussian mixture model algorithm produces the best results on both the DRIVE and STARE databases in metric of specificity. Whereas, the k-medoids algorithm gets better results on the DRIVE database,

while the fuzzy c-means algorithm provides better results on the STARE database in metric of accuracy. On the other hand, in term of running times the k-means algorithm requires less time than other algorithms for retina segmentation on both DRIVE and STARE databases.

Based on this study, it can be seen that the selected clustering algorithms in retinal vessel segmentation have challenges and drawbacks that must be addressed and resolved, such as identifying and segmenting the retinal vessels in a better way, especially the thin vessels or the dendrites of vessels, and also more robust and durable in the segmentation with the low contrast of the images of the retina.

Appendix B

Results obtained using (CF1,2)

We have studied the segmentation phase using the Sugeno integral ($CF_{1,2}$) at the *optimum*. Following our flow chart Figure 4.1, the fuzzy-based adaptive threshold method has been used instead of the traditional one. In addition, several metrics have been used in the evaluation phase, like sensitivity, specificity, accuracy, Matthews correlation coefficient, and F_1 score. The study was carried out on retinal images from the STARE and DRIVE databases. As indicated by the authors of the article **"Sugeno integral generalization applied to improve adaptive image binarization"**- Bardozzo et al., the adaptive thresholding method using Sugeno integral depends on the choice of parameters a_1 and a_2. These two parameters affect the size of the sliding window, and their value must be tuned to optimize the segmentation result. We chose different values for each of a_1 and a_2: at first we chose small values, then bigger ones, and we have noted their effect on the segmentation. The results obtained are presented in the following Table E.1:

B.1 Discussion

The results obtained are shown in Table 1. We can remark that the value of metrics varies depending on the variation of a_1 and a_2.

As regard the results with the STARE database, we can remark that sensitivity, MCC, and F1 are better with $a_1 = 60$ and $a_2 = 30$. However, the best value of accuracy is with $a_1 = 5$ and $a_2 = 3$. Whereas, the best specificity value is with $a_1 = 4$ and $a_2 = 1$. While the DRIVE database, the best results were with $a_1 = 60$ and $a_2 = 30$, except for specificity, which the best valued is with $a_1 = 2$ and $a_2 = 1$.
The experimental result shows that fuzzy adaptive binarization has a significant potential and it can achieve good results. Noting that the value of metrics obtained by fuzzy adaptive binarization are marginally weaker than obtained by the traditional algorithms used in our method. It should also be noted that several experiments have been conducted to improve the results obtained by fuzzy adaptive binarization. Unfortunately, we have not reached values that are better compared with those obtained previously by the proposed method.

Table B.1: The results obtained using ($CF_{1,2}$) at the *optimum*.

STARE					
Parameters	Sn	Sp	Acc	MCC	F1
a_1=2, a_2=1	0.4626	0.9953	0.5539	0.6205	0.6021
a_1=3, a_2=1	0.4628	0.9952	0.9554	0.6206	0.6023
a_1=4, a_2=1	0,4668	**0,9953**	0,9552	0,6239	0,6061
a_1=5, a_2=3	0,4657	0,9952	**0,9555**	0,6223	0,6046
a_1=16, a_2=2	0,4513	0,9943	0,9538	0,5961	0,5823
a_1=23, a_2=25	0,5707	0,9862	0,9553	0,6498	0,6604
a_1=60, a_2= 30	**0,8071**	0,9581	0,9469	**0,6791**	**0,6976**
a_1=150, a_2=150	0.7724	0.9646	0.4133	0.6463	0.6684
DRIVE					
Parameters	Sn	Sp	Acc	MCC	F1
a_1=2, a_2=1	0.3460	**0.9990**	0.9409	0.5572	0.5047
a_1=3, a_2=1	0.3385	0.9967	0.9406	0.5493	0.4944
a_1=4, a_2=1	0,3435	0,9968	0,9400	0,5386	0,4950
a_1=5, a_2=3	0,3619	0,5681	0,9430	0,5214	0,5215
a_1=16, a_2=2	0,3669	0,9975	0,9442	0,5711	0,5248
a_1=23, a_2=25	0,6732	0,9752	0,9493	0,6711	0,6944
a_1=60, a_2= 30	**0,7256**	0,9751	**0,9525**	**0,7078**	**0,7299**
a_1=150, a_2=150	0.7125	0.9770	0.5382	0.7031	0.7244

It is worth mentioning that the proposed method is based on matched filters to improve the quality of the initial image. These filter have been selected after several experiments to increase the performance of the traditional adaptive thresholding method. As future scope, it will be interesting to deepen our study by using other kind of filters which correspond the best with fuzzy adaptive binarization method.

Moreover, a text addressing the highs, lows and reasons to use traditional adaptive thresholding algorithms with respect to the fuzzy ones has been added to the revised version in the subsection 3.5.

Remarks:

- The values presented in the previous table are selected among several tests.
- The final results obtained are the average values of 20 images in both the STARE and DRIVE databases.
- Among the three suggested methods in the paper **"Sugeno integral generalization applied to improve adaptive image binarization"**-Bardozzo et al.[131], we have only presented the best algorithm in terms of results owing to time constraints.
- We did the same work with the Bradley method before choosing the traditional method.

Bibliography

[1] Semchedine, M. *Contribution à la segmentation d'images médicales par les algorithmes bio-inspirés*. PhD thesis, Université Ferhat Abbas, 2018.

[2] Mookiah, M.R.K., Hogg, S., MacGillivray, T.J., Prathiba, V., Pradeepa, R., Mohan, V., Anjana, R.M., Doney, A.S., Palmer, C.N., and Trucco, E. A review of machine learning methods for retinal blood vessel segmentation and artery/vein classification. *Medical Image Analysis*, 68:101905, 2021.

[3] Abdulsahib, A.A., Mahmoud, M.A., Mohammed, M.A., Rasheed, H.H., Mostafa, S.A., and Maashi, M.S. Comprehensive review of retinal blood vessel segmentation and classification techniques: intelligent solutions for green computing in medical images, current challenges, open issues, and knowledge gaps in fundus medical images. *Network Modeling Analysis in Health Informatics and Bioinformatics*, 10(1):1–32, 2021.

[4] Niemeijer, M., Staal, J., van Ginneken, B., Loog, M., and Abramoff, M.D. Comparative study of retinal vessel segmentation methods on a new publicly available database. In *Medical imaging 2004: image processing*, volume 5370, pages 648–656. International Society for Optics and Photonics, 2004. doi: 10.1117/12.535349.

[5] Srinidhi, C.L., Aparna, P., and Rajan, J. Recent advancements in retinal vessel segmentation. *Journal of medical systems*, 41(4):70, 2017. doi: 10.1007/s10916-017-0719-2.

[6] Almotiri, J., Elleithy, K., and Elleithy, A. Retinal vessels segmentation techniques and algorithms: a survey. *Applied Sciences*, 8(2):155, 2018. doi: 10.3390/app8020155.

[7] Mehidi, I., Belkhiat, D.E.C., and Jabri, D. An improved clustering method based on k-means algorithm for mri brain tumor segmentation. In *2019 6th International Conference on Image and Signal Processing and their Applications (ISPA)*, pages 1–6, Mostaganem, Algeria, November 2019. IEEE.

[8] Mehidi, I., Belkhiat, D.E.C., and Jabri, D. Automatic brain tumor segmentation using multi-otsu thresholding and morphological reconstruction. In *Advances*

in Computing Systems and Applications: Proceedings of the 4th Conference on Computing Systems and Applications, pages 289–300, Algiers, Algeria, February 2021. Springer.

[9] Mehidi, I., Belkhiat, D.E.C., and Jabri, D. A fast k-means clustering algorithm for separation of brain tissues in mri. In *2020 2nd International Conference on Mathematics and Information Technology (ICMIT)*, pages 132–137, Adrar, Algeria, February 2020. IEEE.

[10] Drake, R.L., Gray, H., Vogl, W., and Mitchell, A.W. *Gray's anatomy for students*. Elsevier Health Sciences TW, 2005.

[11] Kolb, H. *Gross Anatomy of the Eye*. University of Utah Health Sciences Center, Salt Lake City (UT), 1995. URL http://europepmc.org/books/NBK11534.

[12] Team, H.P. Human Eye Anatomy. https://www.healthpages.org/health-a-z/human-eye-anatomy-surgery-types/, dec 22 2017. [Online; accessed 2023-01-31].

[13] Mookiah, M.R.K., Acharya, U.R., Chua, C.K., Lim, C.M., Ng, E., and Laude, A. Computer-aided diagnosis of diabetic retinopathy: A review. *Computers in biology and medicine*, 43(12):2136–2155, 2013.

[14] Scientists identify natural chemical that causes blinding blood vessel growth. URL https://www.jaymulaney.com/diabetic-retinopathy. [Online; accessed 2023-02-06].

[15] Paredes Soto, D.A. *Probabilistic labelling for enhancement of vessel networks applied to retinal images*. PhD thesis, University of Sheffield, 2016.

[16] Jelinek, H. and Cree, M.J. *Automated image detection of retinal pathology*. Crc Press, 2009.

[17] Miller, J.W., Adamis, A.P., and Aiello, L.P. Vascular endothelial growth factor in ocular neovascularization and proliferative diabetic retinopathy. *Diabetes/metabolism reviews*, 13(1):37–50, 1997.

[18] Melmed, S., Polonsky, K.S., Larsen, P.R., and Kronenberg, H.M. *Williams textbook of endocrinology E-Book*. Elsevier Health Sciences, 2015.

[19] Oloumi, F., Rangayyan, R.M., Oloumi, F., Eshghzadeh-Zanjani, P., and Ayres, F.J. Detection of blood vessels in fundus images of the retina using gabor wavelets. In *2007 29th Annual International Conference of the IEEE Engineering in Medicine and Biology Society*, pages 6451–6454, Lyon, France, August 2007. IEEE.

[20] Rosenfield, M. and Logan, N. *Optometry: Science, Techniques and Clinical Management E-Book*. Elsevier Health Sciences, 2009.

[21] Saine, P.J. and Tyler, M.E. *Ophthalmic photography: retinal photography, angiography, and electronic imaging*, volume 132. Butterworth-Heinemann Boston, 2002.

[22] Trc-NW8/8f. https://topconhealthcare.com/products/trc-nw8f/.

[23] Bernardes, R., Serranho, P., and Lobo, C. Digital ocular fundus imaging: a review. *Ophthalmologica*, 226(4):161–181, 2011.

[24] Yannuzzi, L.A., Ober, M.D., Slakter, J.S., Spaide, R.F., Fisher, Y.L., Flower, R.W., and Rosen, R. Ophthalmic fundus imaging: today and beyond. *American journal of ophthalmology*, 137(3):511–524, 2004.

[25] Organization, W.H. *Prevention of blindness from diabetes mellitus: report of a WHO consultation in Geneva, Switzerland, 9-11 November 2005*. World Health Organization, 2006.

[26] Tasman, W., Jaeger, E., and Duane's Ophthalmology, L.W. Helmut greim 3.11. 1 structure and function. *Toxicology and Risk Assessment: A Comprehensive Introduction*, page 343, 2008.

[27] Williams, G.A., Scott, I.U., Haller, J.A., Maguire, A.M., Marcus, D., and McDonald, H.R. Single-field fundus photography for diabetic retinopathy screening: a report by the american academy of ophthalmology. *Ophthalmology*, 111(5): 1055–1062, 2004.

[28] UCL. The retina and retinal pigment epithelium (RPE), jul 28 2020. URL https://www.drugdiscoveryonline.com/doc/scientists-identify-natural-chemical-that-cau-0001. [Online; accessed 2023-02-06].

[29] Liu, W., Jiang, Y., Zhang, J., and Ma, Z. Rfarn: Retinal vessel segmentation based on reverse fusion attention residual network. *Plos one*, 16(12):e0257256, 2021.

[30] Khan, K.B., Khaliq, A.A., Jalil, A., Iftikhar, M.A., Ullah, N., Aziz, M.W., Ullah, K., and Shahid, M. A review of retinal blood vessels extraction techniques: challenges, taxonomy, and future trends. *Pattern Analysis and Applications*, 22: 767–802, 2019.

[31] Qureshi, I., Ma, J., and Abbas, Q. Recent development on detection methods for the diagnosis of diabetic retinopathy. *Symmetry*, 11(6), 2019. ISSN 2073-8994.

[32] Ahamed, A.T., Jothish, A., Johnson, G., and Krishna, S.B. Automated system for retinal vessel segmentation. In *2018 Second International Conference on Inventive Communication and Computational Technologies (ICICCT)*, pages 717–722, Coimbatore, India, April 2018. IEEE.

[33] Fraz, M.M., Remagnino, P., Hoppe, A., Uyyanonvara, B., Rudnicka, A.R., Owen, C.G., and Barman, S.A. Blood vessel segmentation methodologies in retinal images–a survey. *Computer methods and programs in biomedicine*, 108(1):407–433, 2012.

[34] Dash, S., Verma, S., Khan, M., Wozniak, M., Shafi, J., Ijaz, M.F., et al. A hybrid method to enhance thick and thin vessels for blood vessel segmentation. *Diagnostics*, 11(11):2017, 2021.

[35] URL https://salepeaket.live/product_details/12409487.html.

[36] Despotović, I., Goossens, B., and Philips, W. Mri segmentation of the human brain: challenges, methods, and applications. *Computational and mathematical methods in medicine*, 2015, 2015.

[37] Hua, L., Gu, Y., Gu, X., Xue, J., and Ni, T. A novel brain mri image segmentation method using an improved multi-view fuzzy c-means clustering algorithm. *Frontiers in Neuroscience*, 15:662674, 2021.

[38] Bansal, P., Singh, S.P., and Gopal, K. Human brain mri segmentation approaches and challenges: A review. In *International Conference on Emergent Converging Technologies and Biomedical Systems*, pages 1–8. Springer, 2022.

[39] Chaki, J. Brain mri segmentation using deep learning: background study and challenges. In *Brain Tumor MRI Image Segmentation Using Deep Learning Techniques*, pages 1–12. Elsevier, 2022.

[40] Hoover, A.D., Kouznetsova, V., and Goldbaum, M. Locating blood vessels in retinal images by piecewise threshold probing of a matched filter response. *IEEE Transactions on Medical Imaging*, 19(3):203–210, March 2000. ISSN 0278-0062. doi: 10.1109/42.845178. Accessed: (2020-05-16).

[41] Staal, J., Abràmoff, M.D., Niemeijer, M., Viergever, M.A., and Van Ginneken, B. Ridge-based vessel segmentation in color images of the retina. *IEEE transactions on medical imaging*, 23(4):501–509, 2004. doi: 10.1109/tmi.2004.825627. Accessed: (2020-05-16).

[42] Fraz, M.M., Remagnino, P., Hoppe, A., Uyyanonvara, B., Rudnicka, A.R., Owen, C.G., and Barman, S.A. An ensemble classification-based approach applied to

retinal blood vessel segmentation. *IEEE Transactions on Biomedical Engineering*, 59(9):2538–2548, Sep. 2012. ISSN 0018-9294. doi: 10.1109/TBME.2012.2205687.

[43] Budai, A., Bock, R., Maier, A., Hornegger, J., and Michelson, G. Robust Vessel Segmentation in Fundus Images. *International Journal of Biomedical Imaging*, 2013. doi: 10.1155/2013/154860. URL https://www.hindawi.com/journals/ijbi/2013/154860/.

[44] Porwal, P., Pachade, S., Kamble, R., Kokare, M., Deshmukh, G., Sahasrabuddhe, V., and Meriaudeau, F. Indian diabetic retinopathy image dataset (idrid). IEEE Dataport, 2018. doi: 10.21227/H25W98. URL https://dx.doi.org/10.21227/H25W98.

[45] Azzopardi, G., Strisciuglio, N., Vento, M., and Petkov, N. Trainable cosfire filters for vessel delineation with application to retinal images. *Medical image analysis*, 19(1):46–57, 2015.

[46] Mendonca, A.M. and Campilho, A. Segmentation of retinal blood vessels by combining the detection of centerlines and morphological reconstruction. *IEEE transactions on medical imaging*, 25(9):1200–1213, 2006.

[47] Kumar, K.S. and Singh, N.P. Analysis of retinal blood vessel segmentation techniques: a systematic survey. *Multimedia Tools and Applications*, 82(5):7679–7733, 2023.

[48] Hoover, A., Kouznetsova, V., and Goldbaum, M. Locating blood vessels in retinal images by piecewise threshold probing of a matched filter response. *IEEE Transactions on Medical imaging*, 19(3):203–210, 2000.

[49] Holland, J.H. Genetic algorithms and adaptation. *Adaptive control of ill-defined systems*, pages 317–333, 1984.

[50] Schmidhuber, J. Deep learning in neural networks: An overview. *Neural networks*, 61:85–117, 2015.

[51] Balasubramanian, K. and Ananthamoorthy, N. Robust retinal blood vessel segmentation using convolutional neural network and support vector machine. *Journal of Ambient Intelligence and Humanized Computing*, 12(3):3559–3569, 2021.

[52] Saravanan, V., Samuel, R., Krishnamoorthy, S., and Manickam, A. Deep learning assisted convolutional auto-encoders framework for glaucoma detection and anterior visual pathway recognition from retinal fundus images. *Journal of Ambient Intelligence and Humanized Computing*, pages 1–11, 2022.

[53] Chaudhuri, S., Chatterjee, S., Katz, N., Nelson, M., and Goldbaum, M. Detection of blood vessels in retinal images using two-dimensional matched filters. *IEEE Transactions on medical imaging*, 8(3):263–269, 1989.

[54] Zhang, B., Zhang, L., Zhang, L., and Karray, F. Retinal vessel extraction by matched filter with first-order derivative of gaussian. *Computers in biology and medicine*, 40(4):438–445, 2010.

[55] Li, Q., You, J., and Zhang, D. Vessel segmentation and width estimation in retinal images using multiscale production of matched filter responses. *Expert Systems with Applications*, 39(9):7600–7610, 2012.

[56] Neto, L.C., Ramalho, G.L., Neto, J.F.R., Veras, R.M., and Medeiros, F.N. An unsupervised coarse-to-fine algorithm for blood vessel segmentation in fundus images. *Expert Systems with Applications*, 78:182–192, 2017. doi: 10.1016/j.eswa.2017.02.015.

[57] Winder, R.J., Morrow, P.J., McRitchie, I.N., Bailie, J., and Hart, P.M. Algorithms for digital image processing in diabetic retinopathy. *Computerized medical imaging and graphics*, 33(8):608–622, 2009.

[58] Zana, F. and Klein, J.C. Segmentation of vessel-like patterns using mathematical morphology and curvature evaluation. *IEEE transactions on image processing*, 10(7):1010–1019, 2001.

[59] Ayala, G., León, T., and Zapater, V. Different averages of a fuzzy set with an application to vessel segmentation. *IEEE Transactions on Fuzzy Systems*, 13(3): 384–393, 2005.

[60] Soares, J.V., Leandro, J.J., Cesar, R.M., Jelinek, H.F., and Cree, M.J. Retinal vessel segmentation using the 2-d gabor wavelet and supervised classification. *IEEE Transactions on medical Imaging*, 25(9):1214–1222, 2006.

[61] Fraz, M.M., Barman, S.A., Remagnino, P., Hoppe, A., Basit, A., Uyyanonvara, B., Rudnicka, A.R., and Owen, C.G. An approach to localize the retinal blood vessels using bit planes and centerline detection. *Computer methods and programs in biomedicine*, 108(2):600–616, 2012. doi: 10.1016/j.cmpb.2011.08.009.

[62] Wang, W., Wang, W., and Hu, Z. Retinal vessel segmentation approach based on corrected morphological transformation and fractal dimension. *IET Image Processing*, 13(13):2538–2547, 2019. doi: 10.1049/iet-ipr.2018.5636.

[63] Frangi, A.F., Niessen, W.J., Vincken, K.L., and Viergever, M.A. Multiscale vessel enhancement filtering. In *International conference on medical image computing*

and computer-assisted intervention, pages 130–137, Berlin, 1998. Springer. doi: 10.1007/bfb0056195.

[64] Martinez-Perez, M.E., Hughes, A.D., Thom, S.A., Bharath, A.A., and Parker, K.H. Segmentation of blood vessels from red-free and fluorescein retinal images. *Medical image analysis*, 11(1):47–61, 2007.

[65] Xiao, Z., Adel, M., and Bourennane, S. Bayesian method with spatial constraint for retinal vessel segmentation. *Computational and mathematical methods in medicine*, 2013, 2013.

[66] Zhao, Y., Liu, Y., Wu, X., Harding, S.P., and Zheng, Y. Retinal vessel segmentation: An efficient graph cut approach with retinex and local phase. *PloS one*, 10(4):e0122332, 2015.

[67] Zhao, Y., Rada, L., Chen, K., Harding, S.P., and Zheng, Y. Automated vessel segmentation using infinite perimeter active contour model with hybrid region information with application to retinal images. *IEEE transactions on medical imaging*, 34(9):1797–1807, 2015. doi: 10.1109/tmi.2015.2409024.

[68] Mahtab, S. and Hossein, P. An active contour model using matched filter and hessian matrix for retinal vessels segmentation. *Turkish Journal of Electrical Engineering & Computer Sciences*, 30(1):295–311, 2022.

[69] Can, A., Shen, H., Turner, J.N., Tanenbaum, H.L., and Roysam, B. Rapid automated tracing and feature extraction from retinal fundus images using direct exploratory algorithms. *IEEE Transactions on information Technology in Biomedicine*, 3(2):125–138, 1999.

[70] Vlachos, M. and Dermatas, E. Multi-scale retinal vessel segmentation using line tracking. *Computerized Medical Imaging and Graphics*, 34(3):213–227, 2010.

[71] Adel, M., Moussaoui, A., Rasigni, M., Bourennane, S., and Hamami, L. Statistical-based tracking technique for linear structures detection: Application to vessel segmentation in medical images. *IEEE Signal Processing Letters*, 17(6): 555–558, 2010.

[72] Yin, Y., Adel, M., and Bourennane, S. Retinal vessel segmentation using a probabilistic tracking method. *Pattern Recognition*, 45(4):1235–1244, 2012.

[73] Delibasis, K.K., Kechriniotis, A.I., Tsonos, C., and Assimakis, N. Automatic model-based tracing algorithm for vessel segmentation and diameter estimation. *Computer methods and programs in biomedicine*, 100(2):108–122, 2010.

[74] Hassanien, A.E., Emary, E., and Zawbaa, H.M. Retinal blood vessel localization approach based on bee colony swarm optimization, fuzzy c-means and pattern search. *Journal of Visual Communication and Image Representation*, 31:186–196, 2015.

[75] Akram, M.U. and Khan, S.A. Multilayered thresholding-based blood vessel segmentation for screening of diabetic retinopathy. *Engineering with computers*, 29: 165–173, 2013.

[76] Dash, J. and Bhoi, N. Retinal blood vessel segmentation using otsu thresholding with principal component analysis. In *2018 2nd international conference on inventive systems and control (ICISC)*, pages 933–937, Coimbatore, India, January 2018. IEEE.

[77] Soomro, T.A., Khan, T.M., Khan, M.A., Gao, J., Paul, M., and Zheng, L. Impact of ica-based image enhancement technique on retinal blood vessels segmentation. *IEEE Access*, 6:3524–3538, 2018.

[78] Marín, D., Aquino, A., Gegúndez-Arias, M.E., and Bravo, J.M. A new supervised method for blood vessel segmentation in retinal images by using gray-level and moment invariants-based features. *IEEE Transactions on medical imaging*, 30 (1):146–158, 2010.

[79] Tuba, E., Mrkela, L., and Tuba, M. Retinal blood vessel segmentation by support vector machine classification. In *2017 27th International Conference Radioelektronika (RADIOELEKTRONIKA)*, pages 1–6, Brno, Czech Republic, April 2017. IEEE.

[80] Bandyopadhyay, S., Choudhury, S., Latib, S., Kole, D.K., and Giri, C. Gradation of diabetic retinopathy using knn classifier by morphological segmentation of retinal vessels. In *International Proceedings on Advances in Soft Computing, Intelligent Systems and Applications: ASISA 2016*, pages 189–198. Springer, 2018.

[81] Melinscak, M., Prentasic, P., and Loncaric, S. Retinal vessel segmentation using deep neural networks. In *VISAPP (1)*, pages 577–582, 2015.

[82] Oliveira, W.S., Teixeira, J.V., Ren, T.I., Cavalcanti, G.D., and Sijbers, J. Unsupervised retinal vessel segmentation using combined filters. *PloS one*, 11(2): e0149943, 2016.

[83] Zhang, J., Dashtbozorg, B., Bekkers, E., Pluim, J.P., Duits, R., and ter Haar Romeny, B.M. Robust retinal vessel segmentation via locally adaptive

derivative frames in orientation scores. *IEEE transactions on medical imaging*, 35(12):2631–2644, 2016. doi: 10.1109/tmi.2016.2587062.

[84] Roy, S., Mitra, A., Roy, S., and Setua, S.K. Blood vessel segmentation of retinal image using clifford matched filter and clifford convolution. *Multimedia Tools and Applications*, 78(24):34839–34865, 2019.

[85] Soomro, T.A., Gao, J., Lihong, Z., Afifi, A.J., Soomro, S., and Paul, M. Retinal blood vessels extraction of challenging images. In *Australasian Conference on Data Mining*, pages 347–359, Western Sydney, NSW, Australia, December 2018. Springer. doi: 10.1007/978-981-13-6661-1_27.

[86] da Rocha, D.A., Barbosa, A.B.L., Guimarães, D.S., Gregório, L.M., Gomes, L.H.N., da Silva Amorim, L., and Peixoto, Z.M.A. An unsupervised approach to improve contrast and segmentation of blood vessels in retinal images using clahe, 2d gabor wavelet, and morphological operations. *Research on Biomedical Engineering*, 36(1):67–75, 2020. doi: 10.1007/s42600-019-00032-z.

[87] Fathi, A. and Naghsh-Nilchi, A.R. Automatic wavelet-based retinal blood vessels segmentation and vessel diameter estimation. *Biomedical Signal Processing and Control*, 8(1):71–80, 2013. doi: 10.1016/j.bspc.2012.05.005.

[88] Khomri, B., Christodoulidis, A., Djerou, L., Babahenini, M.C., and Cheriet, F. Retinal blood vessel segmentation using the elite-guided multi-objective artificial bee colony algorithm. *IET Image Processing*, 12(12):2163–2171, 2018. doi: 10.1049/iet-ipr.2018.5425.

[89] Shah, S.A.A., Shahzad, A., Khan, M.A., Lu, C.K., and Tang, T.B. Unsupervised method for retinal vessel segmentation based on gabor wavelet and multiscale line detector. *IEEE Access*, 7:167221–167228, 2019.

[90] Salazar-Gonzalez, A., Kaba, D., Li, Y., and Liu, X. Segmentation of the blood vessels and optic disk in retinal images. *IEEE journal of biomedical and health informatics*, 18(6):1874–1886, 2014.

[91] Zhao, Y., Zhao, J., Yang, J., Liu, Y., Zhao, Y., Zheng, Y., Xia, L., and Wang, Y. Saliency driven vasculature segmentation with infinite perimeter active contour model. *Neurocomputing*, 259:201–209, 2017. ISSN 0925-2312. doi: https://doi.org/10.1016/j.neucom.2016.07.077. Multimodal Media Data Understanding and Analytics.

[92] Jebaseeli, T.J., Durai, C.A.D., and Peter, J.D. Extraction of retinal blood vessels on fundus images by kirsch's template and fuzzy c-means. *Journal of medical physics*, 44(1):21, 2019.

[93] Sindhusaranya, B., Geetha, M., Rajesh, T., and Kavitha, M. Hybrid algorithm for retinal blood vessel segmentation using different pattern recognition techniques. *Journal of Intelligent & Fuzzy Systems*, 43(6):7605–7615, nov 11 2022.

[94] Zuiderveld, K. *Contrast Limited Adaptive Histogram Equalization*, page 474–485. Academic Press Professional, Inc., USA, 1994. ISBN 0123361559.

[95] Pizer, S.M., Amburn, E.P., Austin, J.D., Cromartie, R., Geselowitz, A., Greer, T., ter Haar Romeny, B., Zimmerman, J.B., and Zuiderveld, K. Adaptive histogram equalization and its variations. *Computer vision, graphics, and image processing*, 39(3):355–368, 1987. doi: 10.1016/s0734-189x(87)80156-1.

[96] Koschan, A. and Abidi, M.A. *Digital Color Image Processing*. Wiley-Interscience, USA, 2008. ISBN 0470147083.

[97] Jiang, X.J. and Scott, P.J. Chapter 7 - morphological filtering of free-form surfaces. In Jiang, X.J. and Scott, P.J., editors, *Advanced Metrology*, pages 143–176. Academic Press, 2020. ISBN 978-0-12-821815-0. doi: https://doi.org/10.1016/B978-0-12-821815-0.00007-1. URL https://www.sciencedirect.com/science/article/pii/B9780128218150000071.

[98] Soille, P. et al. *Morphological image analysis: principles and applications*, volume 2. Springer, 1999.

[99] Sazak, Ç., Nelson, C.J., and Obara, B. The multiscale bowler-hat transform for blood vessel enhancement in retinal images. *Pattern Recognition*, 88:739–750, 2019. doi: 10.1016/j.patcog.2018.10.011.

[100] Jerman, T., Pernuš, F., Likar, B., and Špiclin, Ž. Enhancement of vascular structures in 3D and 2D angiographic images. *IEEE transactions on medical imaging*, 35(9):2107–2118, 2016. doi: 10.1109/TMI.2016.2550102.

[101] Sato, Y., Westin, C.F., Bhalerao, A., Nakajima, S., Shiraga, N., Tamura, S., and Kikinis, R. Tissue classification based on 3D local intensity structures for volume rendering. *IEEE Transactions on visualization and computer graphics*, 6 (2):160–180, 2000. doi: 10.1109/2945.856997.

[102] Li, Q., Sone, S., and Doi, K. Selective enhancement filters for nodules, vessels, and airway walls in two-and three-dimensional CT scans. *Medical physics*, 30(8): 2040–2051, 2003. doi: 10.1118/1.1581411.

[103] Erdt, M., Raspe, M., and Suehling, M. Automatic hepatic vessel segmentation using graphics hardware. In *International workshop on medical imaging and*

virtual reality, pages 403–412. Springer, 2008. doi: 10.1007/978-3-540-79982-5_44.

[104] Zhou, C., Chan, H.P., Sahiner, B., Hadjiiski, L.M., Chughtai, A., Patel, S., Wei, J., Ge, J., Cascade, P.N., and Kazerooni, E.A. Automatic multiscale enhancement and segmentation of pulmonary vessels in CT pulmonary angiography images for CAD applications. *Medical physics*, 34(12):4567–4577, 2007. doi: 10.1118/1.2804558.

[105] Voorn, M., Exner, U., and Rath, A. Multiscale hessian fracture filtering for the enhancement and segmentation of narrow fractures in 3D image data. *Computers & geosciences*, 57:44–53, 2013. doi: 10.1016/j.cageo.2013.03.006.

[106] Meleppat, R.K., Miller, E.B., Manna, S.K., Zhang, P., Pugh Jr, E.N., and Zawadzki, R.J. Multiscale Hessian filtering for enhancement of OCT angiography images. In *Ophthalmic Technologies XXIX*, volume 10858, page 108581K. International Society for Optics and Photonics, 2019. doi: 10.1117/12.2511044.

[107] Mehidi, I., Belkhiat, D.E.C., and Jabri, D. Comparative analysis of improved fcm algorithms for the segmentation of retinal blood vessels. *Soft Computing*, 27 (4):2109–2123, 2023.

[108] Wiharto, W. and Suryani, E. The comparison of clustering algorithms k-means and fuzzy c-means for segmentation retinal blood vessels. *Acta Informatica Medica*, 28, 2020. doi: 10.5455/aim.2020.28.42-47.

[109] Mehidi, I., Jabri, D., and Belkhiat, D.E.C. Retinal image segmentation u sing clustering methods: Performance analysis. pages 1058–1066, May 2022. doi: 10.1109/SSD54932.2022.9955670.

[110] Zadeh, L. Fuzzy sets. *Information and Control*, 8(3):338–353, 1965. ISSN 0019-9958. doi: https://doi.org/10.1016/S0019-9958(65)90241-X.

[111] Dunn, J.C. A fuzzy relative of the isodata process and its use in detecting compact well-separated clusters. *Journal of Cybernetics*, 3(3):32–57, 1973. doi: 10.1080/01969727308546046.

[112] Bezdek, J.C., Ehrlich, R., and Full, W. Fcm: The fuzzy c-means clustering algorithm. *Computers & geosciences*, 10(2-3):191–203, 1984.

[113] Nageswara Reddy, P., Satyanarayana, C., and Mohan Rao, C. Brain tumour segmentation using hybrid approach. In *Machine Learning and Internet of Things for Societal Issues*, pages 117–125. Springer, 2022.

[114] Chaira, T. Neutrosophic set based clustering approach for segmenting abnormal regions in mammogram images. *Soft Computing*, pages 1–11, 2022.

[115] Szilagyi, L., Benyo, Z., Szilágyi, S.M., and Adam, H. Mr brain image segmentation using an enhanced fuzzy c-means algorithm. In *Proceedings of the 25th annual international conference of the IEEE engineering in medicine and biology society (IEEE Cat. No. 03CH37439)*, volume 1, pages 724–726, Cancun, Mexico, September 2003. IEEE.

[116] Ahmed, M.N., Yamany, S.M., Mohamed, N., Farag, A.A., and Moriarty, T. A modified fuzzy c-means algorithm for bias field estimation and segmentation of mri data. *IEEE transactions on medical imaging*, 21(3):193–199, 2002.

[117] Singh, M., Asha, C., and Sharma, N. Multi-objective particle swarm optimization based enhanced fuzzy c-means algorithm for the segmentation of mri data. In *Recent Trends in Electronics and Communication*, pages 1031–1041. Springer, 2022.

[118] Chuang, K.S., Tzeng, H.L., Chen, S., Wu, J., and Chen, T.J. Fuzzy c-means clustering with spatial information for image segmentation. *computerized medical imaging and graphics*, 30(1):9–15, 2006.

[119] Li, B.N., Chui, C.K., Chang, S., and Ong, S.H. Integrating spatial fuzzy clustering with level set methods for automated medical image segmentation. *Computers in biology and medicine*, 41(1):1–10, 2011.

[120] Cai, W., Chen, S., and Zhang, D. Fast and robust fuzzy c-means clustering algorithms incorporating local information for image segmentation. *Pattern recognition*, 40(3):825–838, 2007.

[121] Lei, T., Jia, X., Zhang, Y., He, L., Meng, H., and Nandi, A.K. Significantly fast and robust fuzzy c-means clustering algorithm based on morphological reconstruction and membership filtering. *IEEE Transactions on Fuzzy Systems*, 26(5): 3027–3041, 2018. doi: 10.1109/tfuzz.2018.2796074.

[122] Shen, Y., Tang, C., Xu, M., and Lei, Z. Optical selective encryption based on the frfcm algorithm and face biometric for the medical image. *Optics & Laser Technology*, 138:106911, 2021.

[123] Zhang, Y., Bai, X., Fan, R., and Wang, Z. Deviation-sparse fuzzy c-means with neighbor information constraint. *IEEE Transactions on Fuzzy Systems*, 27(1): 185–199, 2018.

[124] Wang, Q., Wang, X., Fang, C., and Yang, W. Robust fuzzy c-means clustering algorithm with adaptive spatial & intensity constraint and membership linking for noise image segmentation. *Applied Soft Computing*, 92:106318, 2020.

[125] Jia, X., Lei, T., Du, X., Liu, S., Meng, H., and Nandi, A.K. Robust self-sparse fuzzy clustering for image segmentation. *IEEE Access*, 8:146182–146195, 2020.

[126] Huang, J., Nie, F., and Huang, H. A new simplex sparse learning model to measure data similarity for clustering. In *Twenty-fourth international joint conference on artificial intelligence*, Buenos Aires Argentina, July 2015.

[127] Mehidi, I., Belkhiat, D.E.C., and Jabri, D. A high accuracy segmentation method for retinal blood vessel detection based on hybrid filters and an adaptive thresholding. *Journal of Ambient Intelligence and Humanized Computing*, pages 1–13, 2022.

[128] Zhang, X. and Wandell, B.A. A spatial extension of CIELAB for digital color-image reproduction. *Journal of the society for information display*, 5(1):61–63, 1997. doi: 10.1889/1.1985127.

[129] Demirkaya, O., Asyali, M.H., and Sahoo, P.K. *Image processing with MATLAB: applications in medicine and biology*. CRC Press, 2008.

[130] Solomon, C. and Breckon, T. *Fundamentals of Digital Image Processing: A practical approach with examples in Matlab*. John Wiley & Sons, 2011.

[131] Bardozzo, F., De La Osa, B., Horanská, L., Fumanal-Idocin, J., delli Priscoli, M., Troiano, L., Tagliaferri, R., Fernandez, J., and Bustince, H. Sugeno integral generalization applied to improve adaptive image binarization. *Information Fusion*, 68:37–45, 2021.

[132] Khawaja, A., Khan, T.M., Naveed, K., Naqvi, S.S., Rehman, N.U., and Nawaz, S.J. An improved retinal vessel segmentation framework using frangi filter coupled with the probabilistic patch based denoiser. *IEEE Access*, 7:164344–164361, 2019. doi: 10.1109/access.2019.2953259.

[133] Bauer, S., Wiest, R., Nolte, L.P., and Reyes, M. A survey of mri-based medical image analysis for brain tumor studies. *Physics in Medicine & Biology*, 58(13): R97, 2013. Accessed: (2019-05-5).

[134] Egger, J., Kapur, T., Fedorov, A., Pieper, S., Miller, J.V., Veeraraghavan, H., Freisleben, B., Golby, A.J., Nimsky, C., and Kikinis, R. Gbm volumetry using the 3d slicer medical image computing platform. *Scientific reports*, 3(1):1–7, 2013. Accessed: (2018-02-16).

[135] Otsu, N. A threshold selection method from gray-level histograms. *IEEE transactions on systems, man, and cybernetics*, 9(1):62–66, 1979.

[136] Eberhart, R. and Kennedy, J. A new optimizer using particle swarm theory. In *MHS'95. Proceedings of the sixth international symposium on micro machine and human science*, pages 39–43. Ieee, 1995.

[137] Brainweb: Simulated Brain Database. https://brainweb.bic.mni.mcgill.ca/.

[138] Joshi, A.A., Shattuck, D.W., and Leahy, R.M. A method for automated cortical surface registration and labeling. In *International Workshop on Biomedical Image Registration*, pages 180–189. Springer, 2012. Accessed: (2018-02-16).

[139] Sezgin, M. and Sankur, B.l. Survey over image thresholding techniques and quantitative performance evaluation. *Journal of Electronic imaging*, 13(1):146–168, 2004.

[140] Couceiro, M. and Ghamisi, P. *Particle Swarm Optimization*, pages 1–10. Springer International Publishing, Cham, 2016. ISBN 978-3-319-19635-0. doi: 10.1007/978-3-319-19635-0_1.

[141] Vijay, V., Kavitha, A., and Rebecca, S.R. Automated brain tumor segmentation and detection in mri using enhanced darwinian particle swarm optimization (edpso). *Procedia Computer Science*, 92:475–480, 2016.

[142] Bala, A. and Chana, I. Intelligent failure prediction models for scientific workflows. *Expert Systems with Applications*, 42(3):980–989, 2015.

[143] Rosa, J.H., Barbosa, J.L., Kich, M., and Brito, L. A multi-temporal context-aware system for competences management. *International Journal of Artificial Intelligence in Education*, 25(4):455–492, 2015.

[144] da Rosa, J.H., Barbosa, J.L., and Ribeiro, G.D. Oracon: An adaptive model for context prediction. *Expert Systems with Applications*, 45:56–70, 2016.